

**Acoustic Reflections
from Cylindrical Blocks of Arctic Ice, 1986**

by
G. R. Garrison
R. E. Francois
T. Wen
R. P. Stein

**APL-UW 8707
August 1988**

**Applied Physics Laboratory University of Washington
Seattle, Washington 98105**

Approved for Public Release; Distribution is Unlimited

Contract N00024-85-C-6264

Contract N00039-88-C-0054

ACKNOWLEDGMENTS

The authors appreciate the discussions with Darrell Jackson, James Luby, and Paul Ingalls and the calculation by Dale Winebrenner of the reflections produced by a transition layer. Special thanks go to the APL arctic crew for the diving and handling of the blocks, and to Warren Fox and William Felton for processing the data and preparing the figures for this report.

This research was supported by the Office of Naval Technology (ONT) with technical management provided by the Naval Ocean Research and Development Activity (NORDA).

ABSTRACT

Measurements of acoustic reflections from cylindrical blocks of arctic ice were conducted in spring 1986. Blocks with diameters of 40, 84, and 109 cm were individually cored out and depressed below the surface. Acoustic pulses were transmitted from below, and thus the returns from the depressed block at shorter range were separable from the reflections off the underside of the ice canopy. The sound source/receiver was moved horizontally beneath the block to measure the angular response pattern. The skeletal layer formed at the bottom of the ice during freezing appeared to reduce the reflection at normal incidence below that expected from the bulk physical properties of the ice; this reduction increased greatly with frequency in the measurement range, 20–80 kHz. The reflective properties are compared with the observed structure of the skeletal layer to understand the nature of the reflection. $\rightarrow (r, 2)$



Accession For	
NTIS GRA&I	<input checked="" type="checkbox"/>
DTIC TAB	<input type="checkbox"/>
Unannounced	<input type="checkbox"/>
Justification	
By	
Distribution/	
Availability Codes	
Dist	Avail and/or Special
A-1	

CONTENTS

	<i>Page</i>
I. Introduction	1
II. Summary	3
III. The Experiment	5
IV. Experimental Arrangement	7
V. Transducers	19
VI. Calibration	20
A. From Air-Block Returns	20
B. From Sphere Returns	28
VII. Measurements	32
A. Short Block with Skeletal Layer Removed	32
B. The 84-cm Block	39
C. The 40-cm Block	45
D. The 109-cm Block	45
VIII. Lower Face Reflections	62
A. Area Dependence	62
B. The High Return from 40-cm Block	66
C. Effect of Skeletal Layer	67
D. Effect of Large-Scale Surface Features	68
E. Frequency Dependence	68
F. Equivalent Reflection Coefficients	68
G. Comparison with 1984 Experiment	70
IX. Upper Face Reflections	72
A. Absorption Calculated from Short-Block Measurements	72
B. Absorption Calculated from Other Blocks	81
X. Recommendations	86
XI. References	87
Appendix A. Effect of Surface Variations	A1
A. Gaussian Distribution of Surface Irregularities	A1
B. Cylindrical	A2
C. Sinusoidal	A2
Appendix B. Sound Speed Transition Layer	B1

LIST OF FIGURES

	<i>Page</i>
Figure 1. Ice properties obtained from measurements of samples taken with a Sipre corer.....	7
Figure 2. Plan view of transducer control system.....	8
Figure 3. Elevation view of transducer support system (a two-dimensional simplification).....	9
Figure 4. Combined figure showing the frame above the ice and the support used to hold the block vertical.....	9
Figure 5. Location of ice blocks and frame	10
Figure 6. The frame used in positioning the transducer below the ice block	11
Figure 7. The various block faces measured during the ice block reflection experiment.....	12
Figure 8. Vertical poles frozen into place at each block position.....	14
Figure 9. The equipment used to cut out a cylindrical block of ice.....	14
Figure 10. Depressing and guying the 84-cm block	15
Figure 11. The blocking and wedging used to hold the pole in place.....	16
Figure 12. Removal of a block after the reflection measurement was completed	17
Figure 13. The 84-cm block after removal	18
Figure 14. Frequency response of the ITC 1042 transducer with 500 ft of cable, using transmit/receive box No. 2.....	19
Figure 15. Frequency response of the hemispherical transducer with 500 ft of cable, using transmit/receive box No. 2.....	20
Figure 16. The metal cylinder used to form a block of air.....	21
Figure 17. Returns from the air block, using the ITC transducer	22
Figure 18. Returns from the air block, using the hemispherical transducer	22
Figure 19. Air-block target-strength patterns for Run 18, line E32.....	24
Figure 20. Air-block target-strength patterns for Run 20, line N21, ITC transducer	25
Figure 21. Air-block target-strength patterns for Runs 13-16, hemispherical transducer	26
Figure 22. Air-block target-strength at normal incidence with transducer calibration adjusted for best fit to the entire pattern of the return.....	27

Figure 23.	Target strength of the sphere during measurements of the returns from the air block, using the ITC transducer.....	29
Figure 24.	Target strength of the sphere during measurements of the returns from the 40-cm block, using the ITC transducer.....	30
Figure 25.	Target strength of the sphere during measurements of the returns from the short block (described in Section VII.A), using the ITC transducer	31
Figure 26.	Target strength of the sphere during measurements of the returns from the 84-cm block, using the ITC transducer.....	31
Figure 27.	Target strength of the sphere during measurements of the returns from the 109-cm block, using the ITC transducer.....	32
Figure 28.	The short block (standing on edge) made by sawing off both ends of the block removed for the diver entry hole.....	33
Figure 29.	Returns from the short block using the ITC transducer.....	34
Figure 30.	Short-block target strength at normal incidence using the ITC transducer	35
Figure 31.	Short-block target-strength patterns for Run 24, line N22	36
Figure 32.	Short-block target-strength patterns for Run 26, line E30.....	37
Figure 33.	Predicted patterns for a block that was formed with a cut that was cylindrical on one side, adding 2 cm at the edge	38
Figure 34.	Returns from the 84-cm block, using the ITC transducer and a 0.35 ms pulse.....	40
Figure 35.	Returns from the 84-cm block, using the hemispherical transducer	40
Figure 36.	Target strengths of 84-cm block at normal incidence	41
Figure 37.	Target-strength patterns of 84-cm block for Run 2A, line E32.....	42
Figure 38.	Target-strength patterns of 84-cm block for Run 2B, line N22.....	43
Figure 39.	Target-strength patterns of 84-cm block for Runs 1, 6, 8, and 10.....	44
Figure 40.	Returns from the 40-cm block, using the ITC transducer	47
Figure 41.	Returns from the 40-cm block, using the hemispherical transducer	47
Figure 42.	Target strengths of 40-cm block at normal incidence	48
Figure 43.	Target-strength patterns of 40-cm block for Run 29, line N24	49
Figure 44.	Target-strength patterns of 40-cm block for Run 31, line E29.....	50

Figure 45.	Target-strength patterns of 40-cm block for Runs 34–37.....	51
Figure 46.	Returns from the 109-cm block, using the ITC transducer	52
Figure 47.	Returns from the 109-cm block, using the hemispherical transducer	52
Figure 48.	Target strengths of 109-cm block at normal incidence	53
Figure 49.	Target-strength patterns of 109-cm block for Run 42, range 30 m	54
Figure 50.	Target-strength patterns of 109-cm block for Run 44, range 30 m	55
Figure 51.	Target-strength patterns of 109-cm block for Runs 39 and 40, range 30 m	56
Figure 52.	Target-strength patterns of 109-cm block for Run 46, range 20 m	57
Figure 53.	Target-strength patterns of 109-cm block for Run 48, range 15 m	58
Figure 54.	Target-strength patterns of 109-cm block for Run 50, range 15 m	59
Figure 55.	Target strengths of 109-cm block at normal incidence for measurements at three ranges, ITC transducer only	60
Figure 56.	A comparison of the returns for Runs 48 and 50, 109-cm block.....	61
Figure 57.	The measured target strengths at normal incidence for all blocks (no area correction)	63
Figure 58.	Target-strength measurements with an area correction of $10 \log A$	64
Figure 59.	Target-strength measurements with an area correction of $20 \log A$	65
Figure 60.	Amplitude reflection coefficients, R_A , corresponding to target strength for an 84-cm block.....	69
Figure 61.	Comparison of 1984 and 1986 results for the 84-cm block at normal incidence	71
Figure 62.	The constant B in Eq. 2 as determined from the 1986 measurements on an 84-cm diameter block	71
Figure 63.	Lower and upper face reflections for the short block	73
Figure 64.	Reflections from the short block, showing three levels, followed by the reflection from the under-ice surface	75
Figure 65.	Reflections from the air block, followed by the reflection from the under-ice surface.....	78
Figure 66.	Absorption computed from lower and upper face echoes for the short block	79
Figure 67.	Phase differences between returns at several frequencies from the upper and lower face of the short block.....	80

Figure 68.	Lower and upper face reflections for the 84-cm block.....	81
Figure 69.	Other observations of upper face reflections	83
Figure 70.	Other observations of upper face reflections, 109-cm block.....	84
Figure 71.	Absorption calculated in the three uncut blocks under three assumptions for upper surface reflection.....	85
Figure A1.	Computed effects of surface variations with a Gaussian distribution	A-3
Figure B1.	Predicted reflection coefficient for the bottom of the ice with a linear transition of sound speed over thickness L	B-3

LIST OF TABLES

Table I.	Schedule of events.....	6
Table II.	Combined transmitting response and receiving sensitivity as determined from the air-block returns	27

I. INTRODUCTION

The acoustic reflection of underwater sound from ice keels is not presently well modeled. Most modeling^{1,2} includes the stacking of ice blocks to form a keel and disregards the condition of the surface. There are two problems with this. The first is that ice keels are formed by pressure and consist of a jumbled, undefinable mass of broken and crushed ice. As a result, establishing a representative configuration of blocks for predicting acoustic returns, even for statistical studies, is difficult. The second problem lies in predicting the effect of the block's surface character, which varies with depth, season, and the freezing process.

Another, and probably better, approach would be empirical modeling based on acoustic measurements. Our current thinking is that the largest reflections originate from blocks with a large face nearly normal to the incident ray path. Such reflections could be modeled by (1) making acoustic scans of the ice to determine typical spacings and target strengths of these reflections, (2) measuring the response patterns of some ice blocks of known size and condition, and (3) combining these to model an ice field of reflectors with various target strengths, orientations, and response patterns.

For either approach, it is important to understand the reflection mechanisms better. The Applied Physics Laboratory has been conducting a series of measurements of the target strength and response pattern of known, isolated blocks of natural sea ice of several sizes. These measurements, which are conducted at frequencies of 20–80 kHz, began in the fall of 1984 and continued in the spring of 1986.

In the fall 1984 experiment,³ we measured the reflections from an 84-cm diameter block cut from 46-cm thick ice. At 20 kHz, the return was only 3 dB below that calculated for a rigid plate,⁴ assuming a loss of 9.5 dB for the impedance mismatch. At higher frequencies (up to 80 kHz), the return was as much as 30 dB below the predicted value. The directional response patterns showed a central peak but only a hint of the nulls predicted for a rigid plate. Reflections from the back face of the block were observed at

80 kHz, the only frequency for which recordings were made for later examination of the second reflection.

For the spring 1986 experiment, we incorporated several new features. A cylindrical "block" of air and a spherical target were added to provide two independent calibrations of the acoustic system. A block with the skeletal layer* removed was included to give a measure of the reflection from a fairly smooth surface, where the reflection loss would be primarily due to the resulting sharp impedance mismatch at the water-ice interface. Instead of one diameter, three diameters of blocks were used: 40, 84, and 109 cm. For the largest block, the acoustic range was decreased to $2/3$ and then $1/2$ the original range to test the range dependence. The return from the back face was observed at 20–80 kHz and was used to estimate sound absorption in the ice. The 1986 experiment is the subject of this report.

*As used here, the term "skeletal layer" refers to the transition zone between solid ice and water at the lower surface of sea ice. In spring 1986 the skeletal layer was 10–15 cm thick.

Known as "skeletal layer" in the literature, this is the transition zone between solid ice and water at the lower surface of sea ice. In spring 1986 the skeletal layer was 10–15 cm thick.

II. SUMMARY

The acoustic returns from three flat, circular areas of the underside of first-year, growing ice, as well as from a sawed off face, were measured at frequencies of 20–80 kHz to further the study of reflections from ice keels. Reflections were measured similarly for air–water interfaces of the same size as the blocks; the close agreement with theory verified the high accuracy of the method. The results show the following.

- (1) Reflection from a circular area of hard ice at normal incidence followed predictions for the impedance mismatch between water and ice. The angular response pattern agrees with the prediction for a rigid plate. (Combining these two separate effects to give the return at all angles is allowed by the Kirchhoff approximation.)
- (2) Reflection from a circular area of the underside of arctic ice is considerably lower than that from hard ice — from 10 dB at 20 kHz to 30 dB at 80 kHz. This reduced reflectivity is attributed to the skeletal layer. However, the short rise time of the return and the frequency dependence of the results indicate that, at most, only the lower 1 or 2 cm of the skeletal layer is involved. At the 0–10° incident angles of the measurements, the response does not follow the predicted sidelobe pattern; instead, it falls off at about 3 dB per degree for the blocks with diameters of 40 and 84 cm. The 109-cm diameter block is large enough that the trends and details of the pattern are obscured by the effect of long-wavelength, small-amplitude variations which are apparently inherent to thick natural sea ice, even in "flat" areas.
- (3) A return from the back face (i.e., the submerged upper face) of the three 1.6-m thick blocks was observed at most of the frequencies. This indicates that the thickness of flat, first-year ice can be measured from below. The

sonar beam would have to be narrow, but with air above the upper surface the reflections should be much larger than observed for the submerged ice blocks. The measured returns from the upper face indicate an average absorption loss of 5–10 dB per meter for vertical transmissions. There is some indication, however, that most of the absorption occurs in the skeletal layer.

Further investigation should be made to determine the effect of the undulations often observed on the underside of refrozen leads. These have a long wavelength and thus will have a greater effect on reflections from larger diameter blocks; measurements should be made with blocks of several diameters to explore this effect. The structure of the skeletal layer and any associated changes in acoustic properties with temperature should be examined. All future measurements should be made without diver assistance to eliminate any contamination of the skeletal layer with air.

III. THE EXPERIMENT

The experiment was conducted the last week of March 1986 at ice camp APLIS during the U.S. Navy's ICEX-86. The environmental conditions have been reported elsewhere.⁵ To support the camp, a large refrozen lead, 1.6 m thick, was used as a landing strip. This large expanse of ice, which appeared to be flat and uniform, was selected as the most suitable for the experiment. Near the end of the air strip, a cylindrical block was cut out with an APL thermal drill that forces heated water through small holes in a circular manifold to melt a circular groove about 5 cm wide in the ice.⁶ When free, the block was normally forced downward about 1 m and guyed into a fixed position with the lower face horizontal. In one case, the block was removed from the ice, and the lower and upper surfaces were cut off to create abrupt interfaces. A transducer suspended 30 m below the block served to transmit sound pulses and receive the reflections from the lower face of the block. The transducer was supported on lines so that it could be moved along a track which passed beneath the block. Each such pass is called a "run."

The schedule of events is summarized in Table I. The air temperature was considerably lower than the water temperature, and thus the time that the blocks were submerged before the measurements may have affected their temperature. A sample of the ice was obtained at the experiment site with a Sipre corer. Figure 1 shows the measured properties of the ice. Note that two temperatures are shown. The "in situ" values were measured as soon as possible after the core was withdrawn from the ice. (There was a delay of several minutes while removing the ice from the corer, laying it out, drilling measurement holes, and inserting the temperature probe.) The other temperature values were taken during the density measurements, which involved a hydrostatic weighing of the sample in a bath of iso-octane whose specific gravity was measured by hydrometer. From the measurement of the temperature, density, and salinity of each sample, the total void volume (brine volume plus air volume) was computed, using the method of Cox and Weeks.⁷

Table 1. Schedule of events.

Date	Time	Event
24 March		Frame constructed on the ice.
25 March		84-cm block cut and pushed down. Diver-entry hole prepared.
26 March		Installed lines under the ice using divers (necessarily releasing some unwanted air under the ice). Runs 1 and 2.
27 March	a.m.	Installed target sphere 6 m below top ice. Sphere nearly full of Freon.
	1000-1110	Runs 4 and 5. Sphere returns. Runs 6 and 7. Sphere topped off with Freon (it apparently split at the seam when re-installed). Sawed both ends off an 84-cm block to form "short block."
	2000-2200	Runs 8-12 on 84-cm block. Removed 84-cm block.
28 March	1130	Installed air block. Runs 13 and 14.
29 March	0630	Runs 15-17.
	0845	Runs 18-21.
	1030	Installed short block. Runs 24-28.
	1900	Cut and depressed 40-cm block.
	2000-2200	Runs 29-33.
30 March	0800-1000	Runs 34-38.
	1900	Cut and depressed 109-cm block. Runs 39-41.
31 March	0800	Runs 42-44.
	1000	Run 46 with transducer raised to shorter range.
	1030	Runs 48 and 50 with transducer raised to shorter range.
1 April		Recovered sphere. Found to be split open.

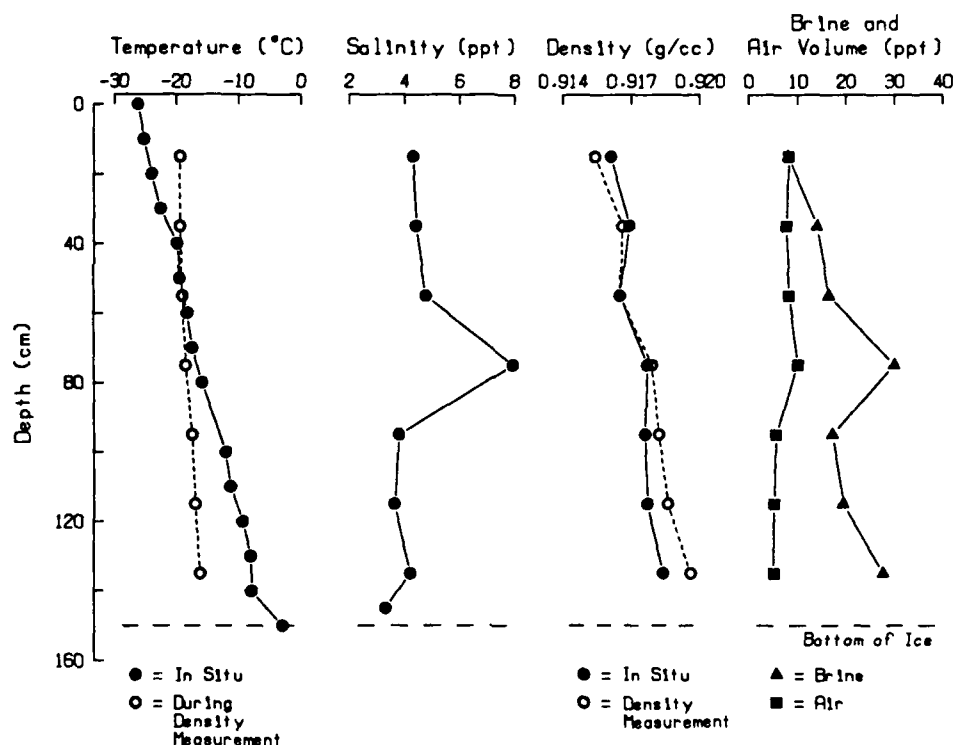


Figure 1. Ice properties obtained from measurements of samples taken with a Sipre corer.

IV. EXPERIMENTAL ARRANGEMENT

The experimental arrangement (Figures 2–6) remained the same as in 1984. The transducer was connected by lines to a ring, which was placed over one of many pegs on a rectangular wooden frame such that the position of the transducer could be calculated from the position of the ring. The spacing of the pegs was 15 cm, and the peg-to-peg movement of the transducer was about 21 cm, or an angle change of 0.4° . The accuracy of positioning is estimated to be about 10 cm. Each peg was designated by north and east coordinates N and E and labeled. After the N and E of the peg for which the transducer output was maximum were determined, two perpendicular runs were made, one north–south along an E line and one east–west along an N line. The various block faces used to measure reflections are shown in Figure 7.

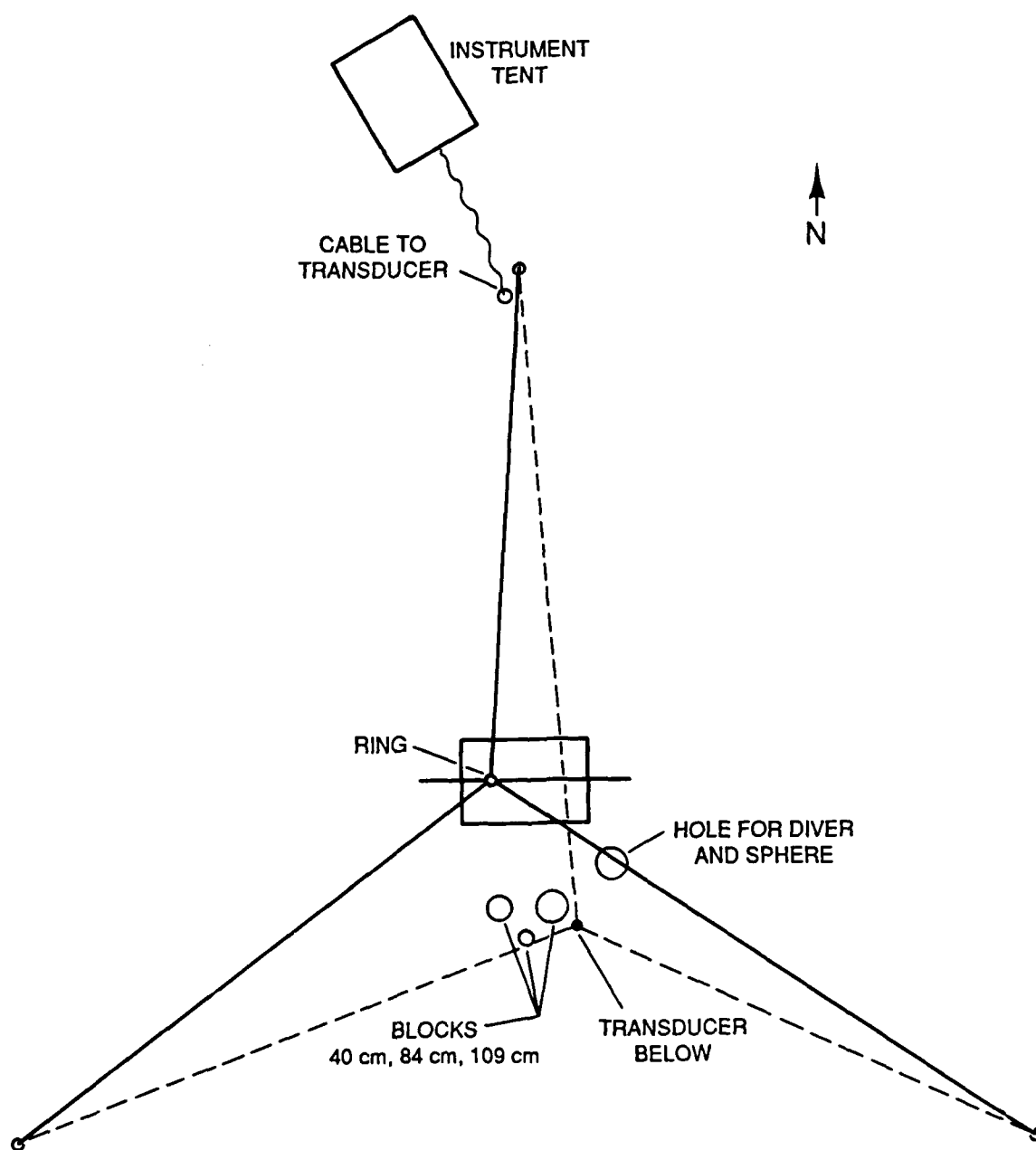


Figure 2. Plan view of transducer control system.

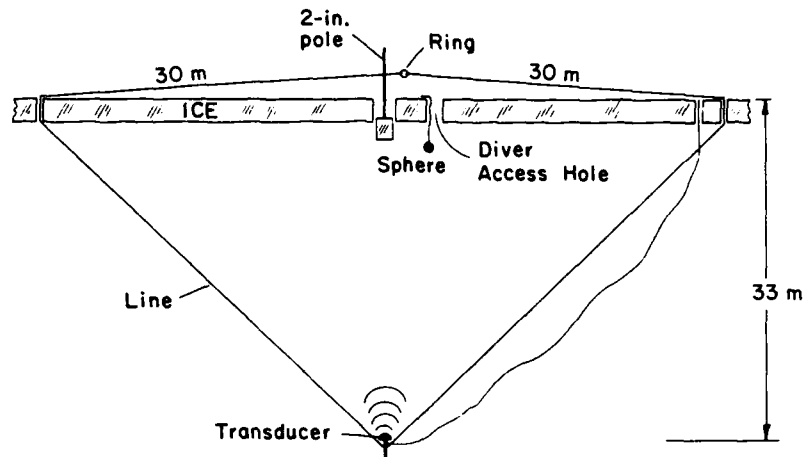


Figure 3. Elevation view of transducer support system (a two-dimensional simplification).

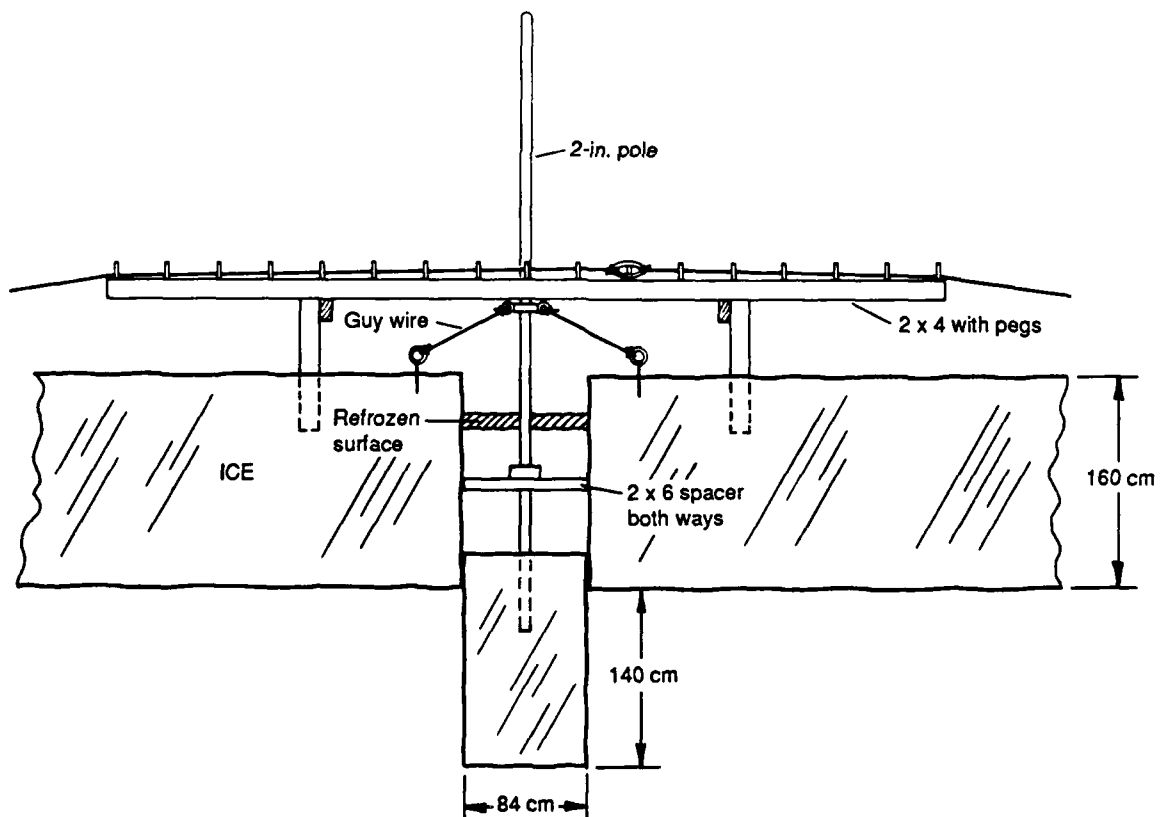


Figure 4. Combined figure showing the frame above the ice and the support used to hold the block vertical. The frame was actually offset from the ice blocks, as shown in Figures 2 and 5.

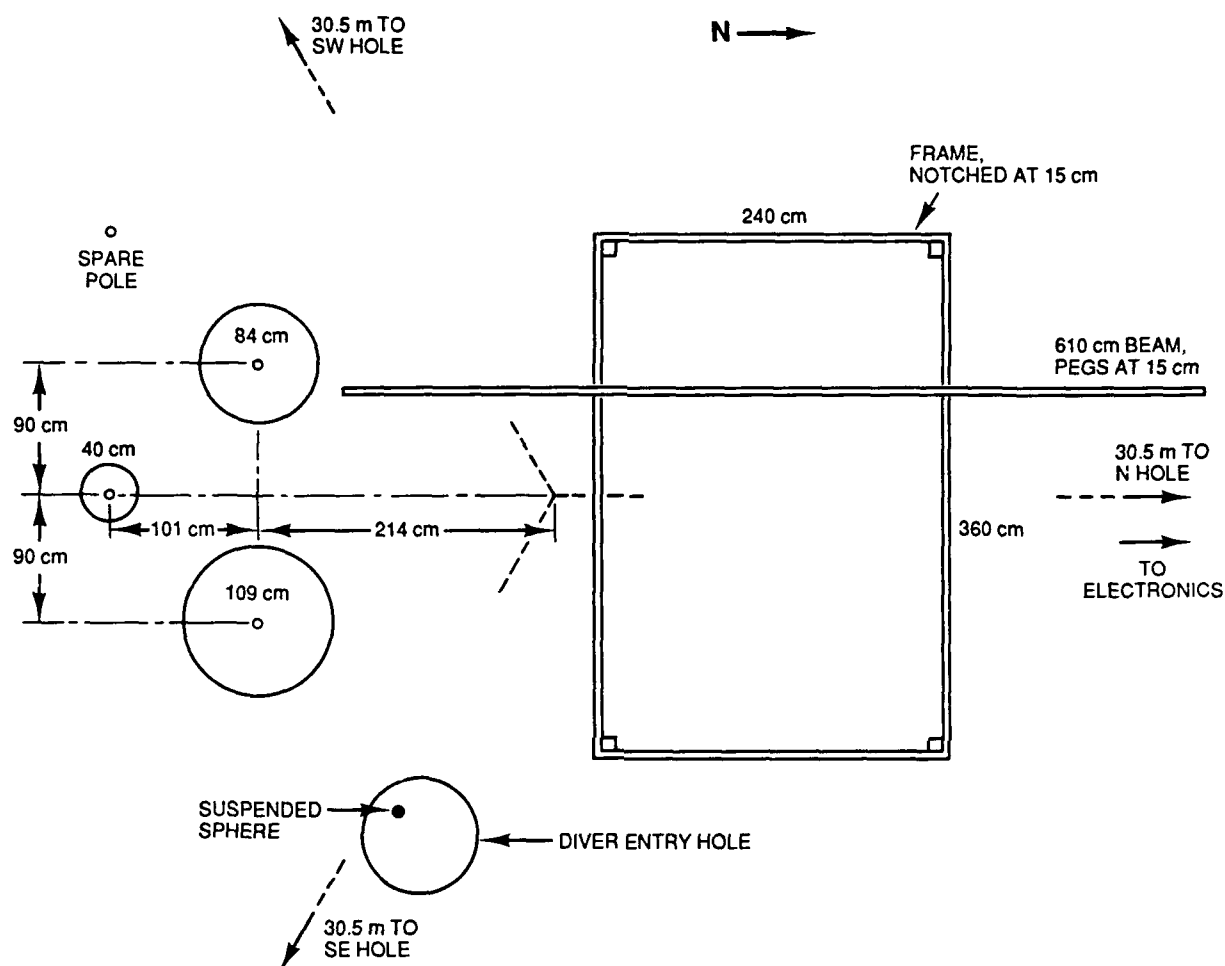


Figure 5. Location of ice blocks and frame.

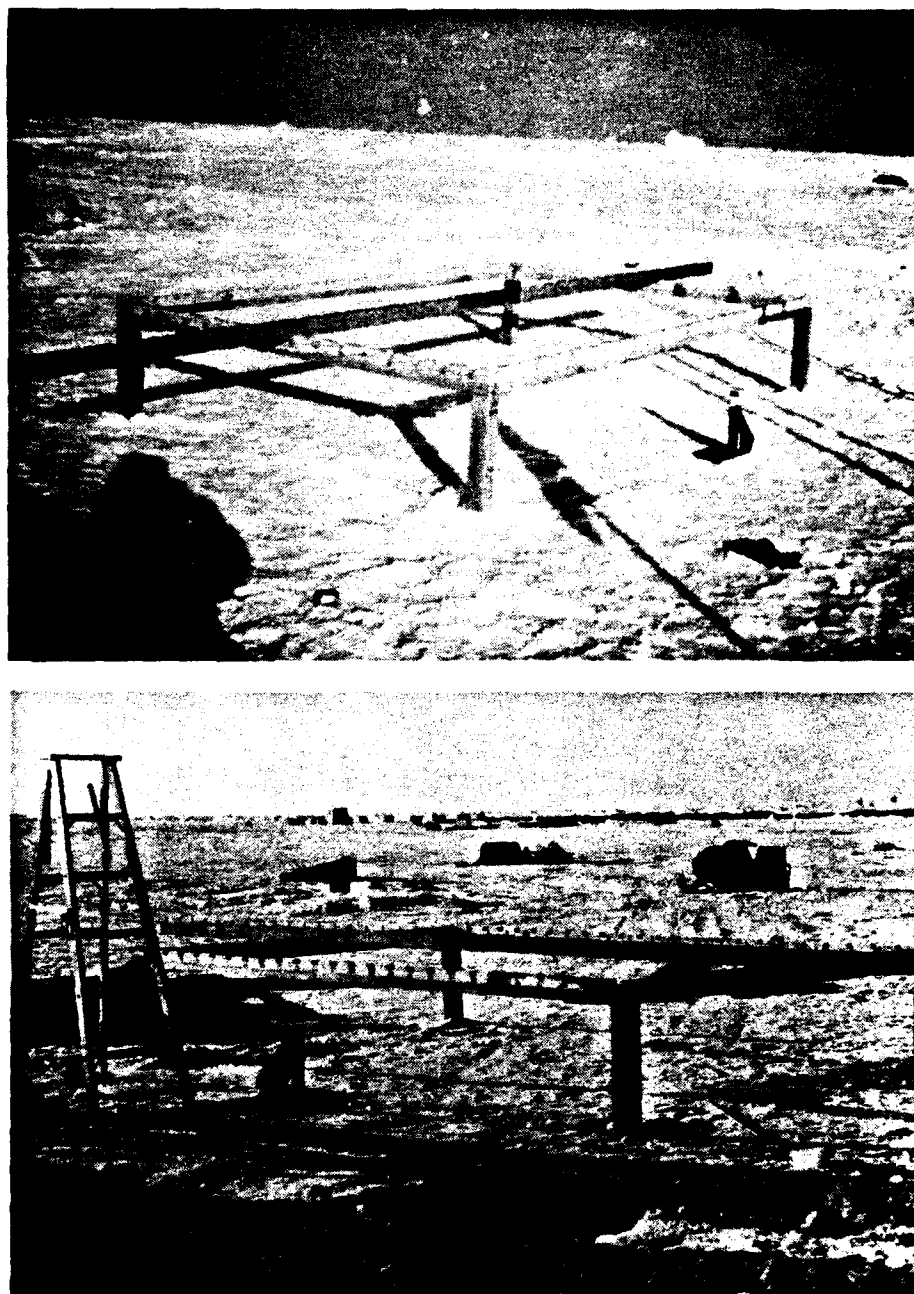


Figure 6. The frame used in positioning the transducer below the ice block.

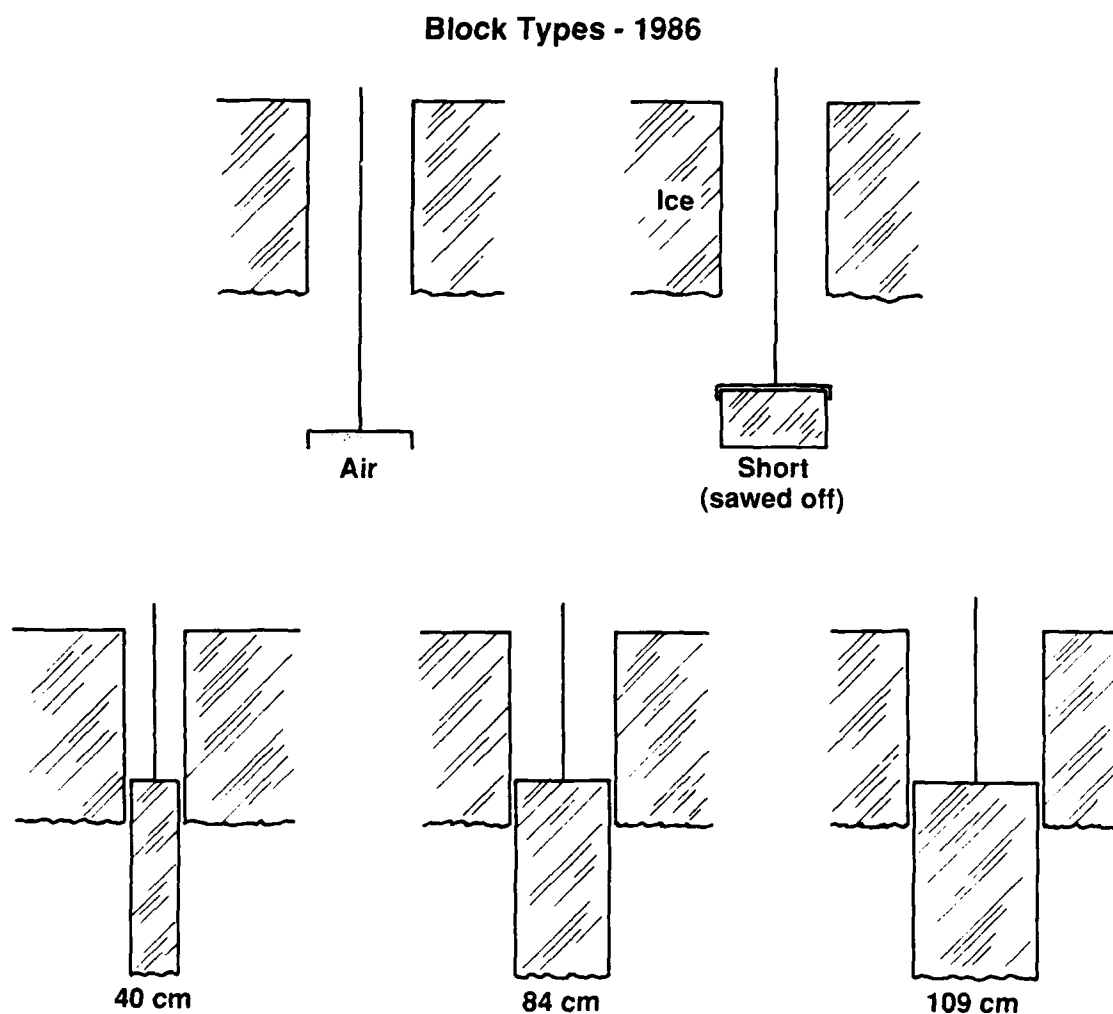


Figure 7. The various block faces measured during the ice block reflection experiment. The wavy line for the bottom is symbolic; the skeletal layer appeared quite smooth.

Before beginning the experiment, the locations of the blocks, the frame, and the support lines were carefully surveyed. At the location of each block, a 30-cm deep, 10-cm diameter hole was drilled in the ice. A 3-m long, 5-cm diameter aluminum tube was then plumbed vertically in the hole, and fresh water and snow were packed around the pole. By the next day, the poles were frozen solidly in place (Figure 8). When each block was later cut out and guyed into place, this pole was kept vertical to assure that the lower face of the block was horizontal, or at least as nearly so as it was originally.

To make the diver-entry hole, a 90-cm diameter hole was melted with the APL thermal drill, Figure 9. This hole was near the positioning frame as shown in Figure 6. After we drilled the three 23-cm holes for the lines and another 90-cm hole for handling the transducer, the divers swam the support lines from the diver access hole to the three 23-cm holes 30 m away. When all lines were connected, the transducer was installed through the transducer hole. In the meantime, the 84-cm block was melted out, forced down, wedged in place with blocks, and supported by guylines (Figures 10 and 11). Later, the procedure was repeated for the other blocks.

When the measurements on each block were completed, the block was removed, placed on a sled, and moved out of the way (Figures 12 and 13). The lower portion of the 84-cm block appears dark in Figure 13 because of entrapped brine, some of which has drained out onto the sled and frozen. This darkened area indicates the extent of the skeletal layer.

The transmitting, receiving, and recording equipment was operated in a tent at the north edge of the site. For the experiment, 0.35–1.0 ms cw pulses at 20–80 kHz were transmitted from the transducer, and the envelope of the returns was recorded on a Nicolet digital oscilloscope. These records were saved on diskettes for later analysis. In addition, as a backup, the signals were heterodyned to 5 kHz and recorded on a video cassette recorder.

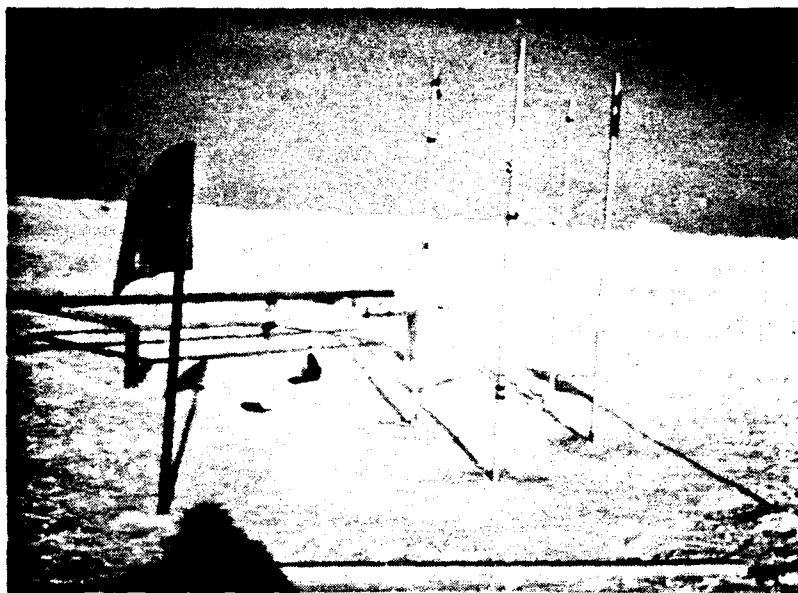


Figure 8. Vertical poles frozen into place at each block position.

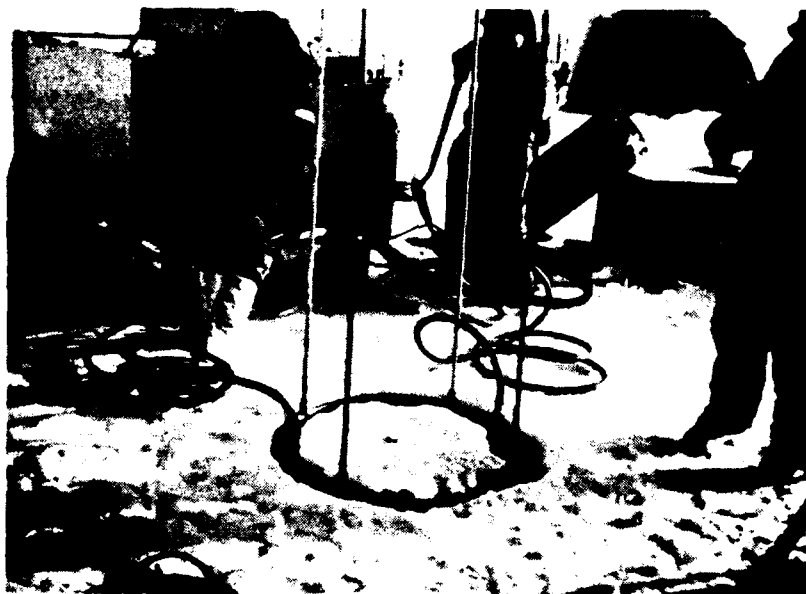


Figure 9. The equipment used to cut out a cylindrical block of ice. Hot water is pumped through a hose into a circular tube with holes in the bottom. The "jetting" water melts the ice and the melt water is then returned to the pump through a second hose.



*Figure 10.
Depressing and guying
the 84-cm block.*

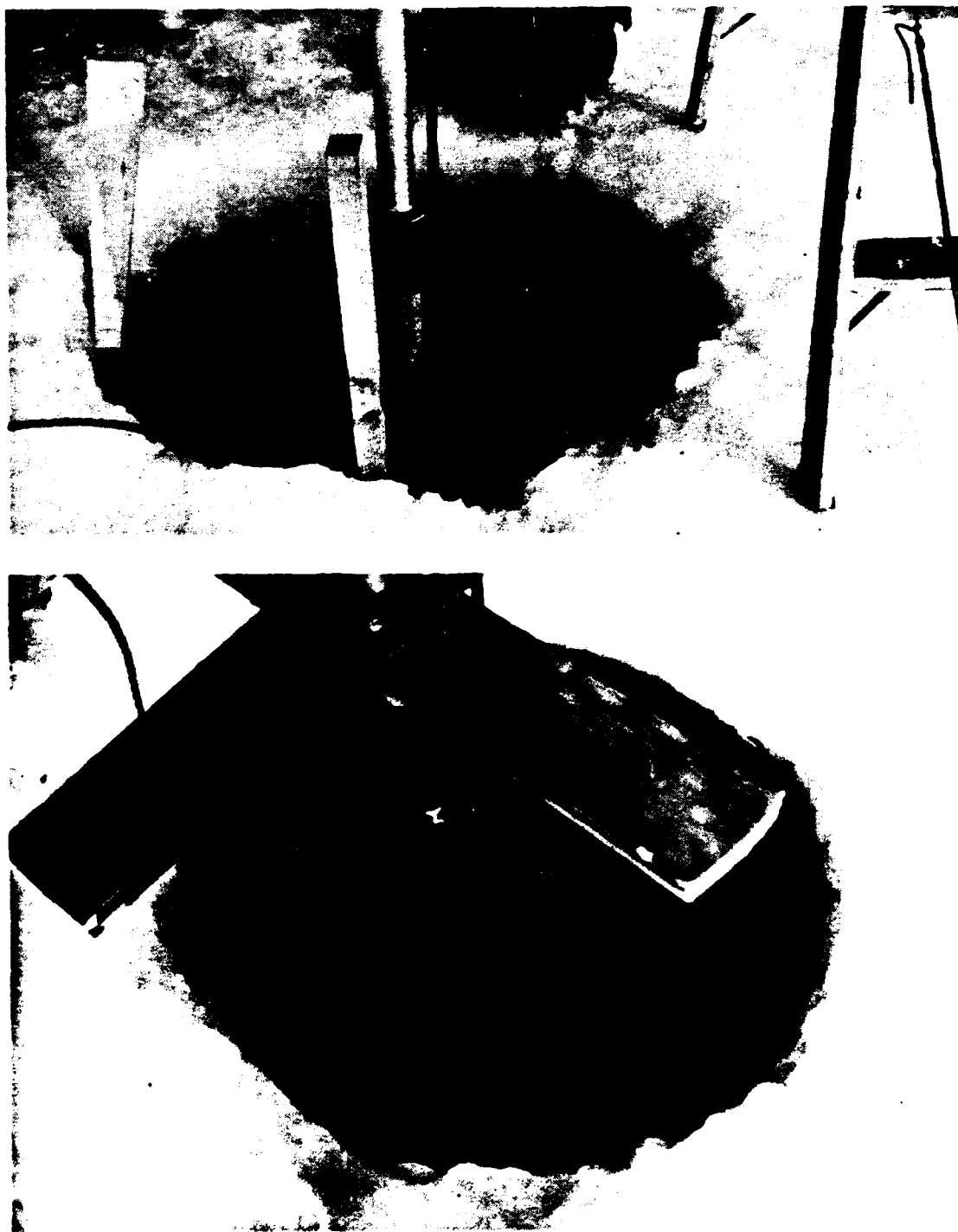


Figure 11. The blocking and wedging used to hold the pole in place.

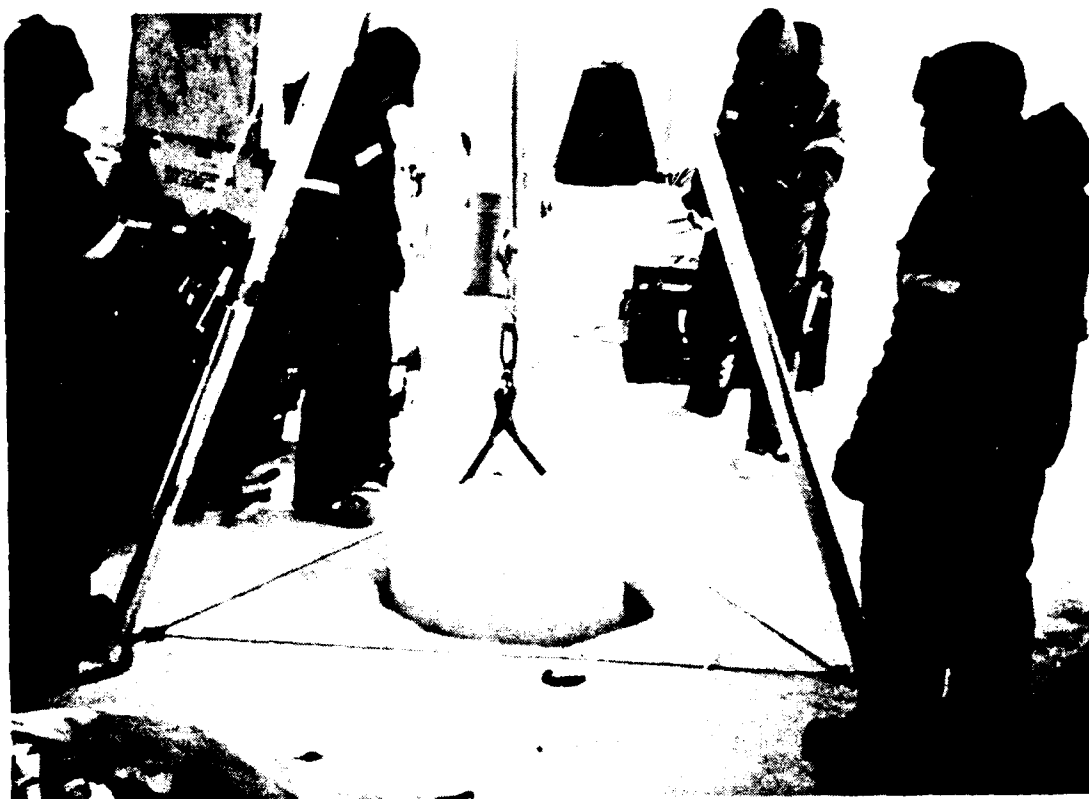


Figure 12. Removal of a block after the reflection measurement was completed.

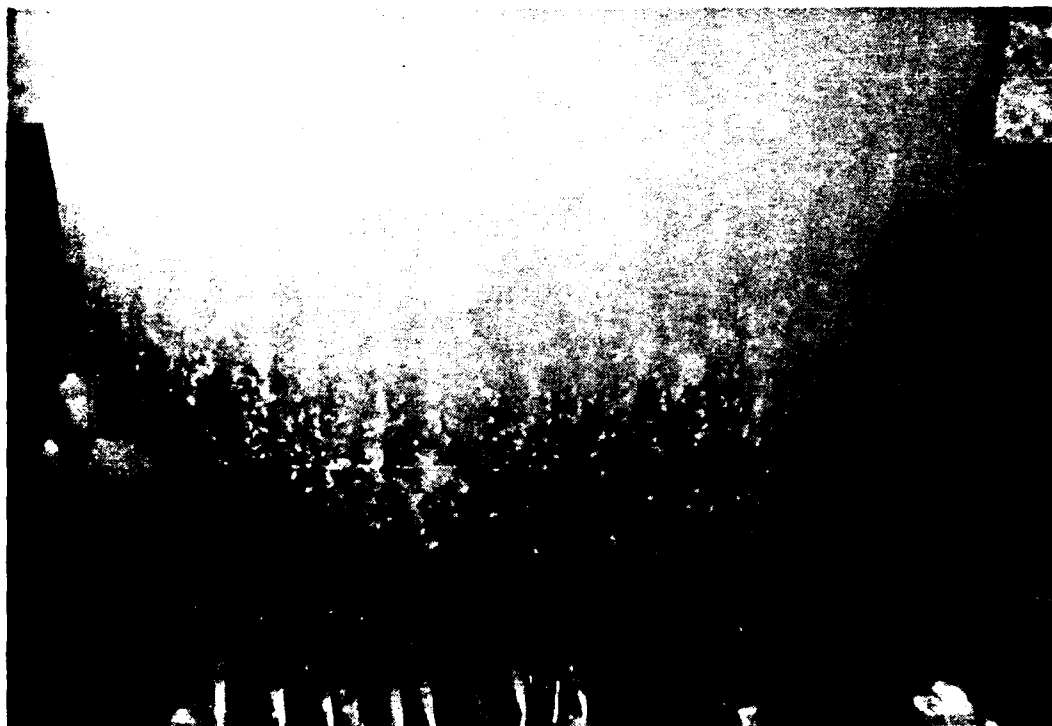


Figure 13. The 84-cm block after removal. Brine trapped in the lower part has drained out and frozen.

V. TRANSDUCERS

From an experimental viewpoint, it would be more efficient to use only one transducer to cover the desired frequency range, 20–80 kHz. Our best candidate, an ITC 1042 spherical transducer, however, had low transmitting response at the low-frequency end, as seen in Figure 14. To remedy this, another transducer was provided to cover the lower frequencies, a hemispherical bowl transducer with several resonances that we thought might also be useful for other experiments. The response curves of the hemisphere are shown in Figure 15. This transducer was operated at 20 and 30 kHz during the experiment.

Because we cannot duplicate the arctic water temperatures (i.e., the transducer temperature) at our calibration barge, we depend on the in-field procedure described in the next section for transducer calibration.

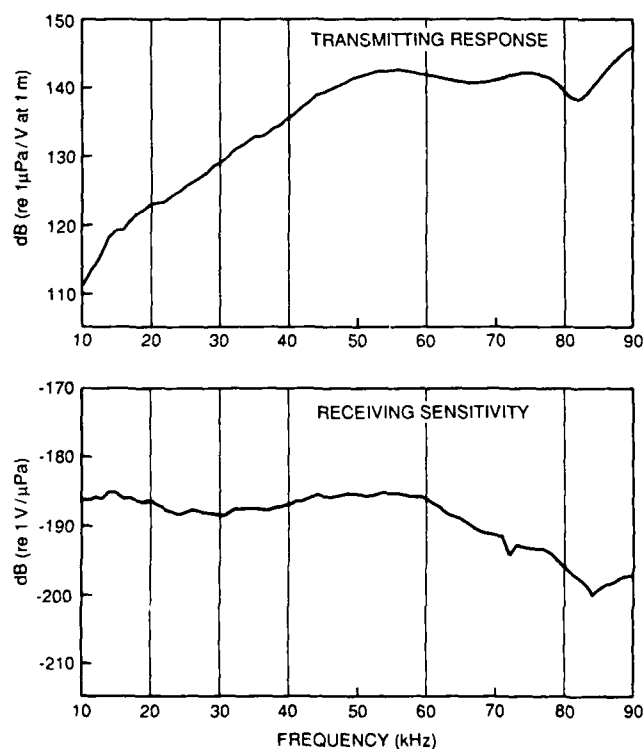


Figure 14.
Frequency response of the ITC 1042 transducer with 500 ft of cable, using transmit/receive box No. 2.

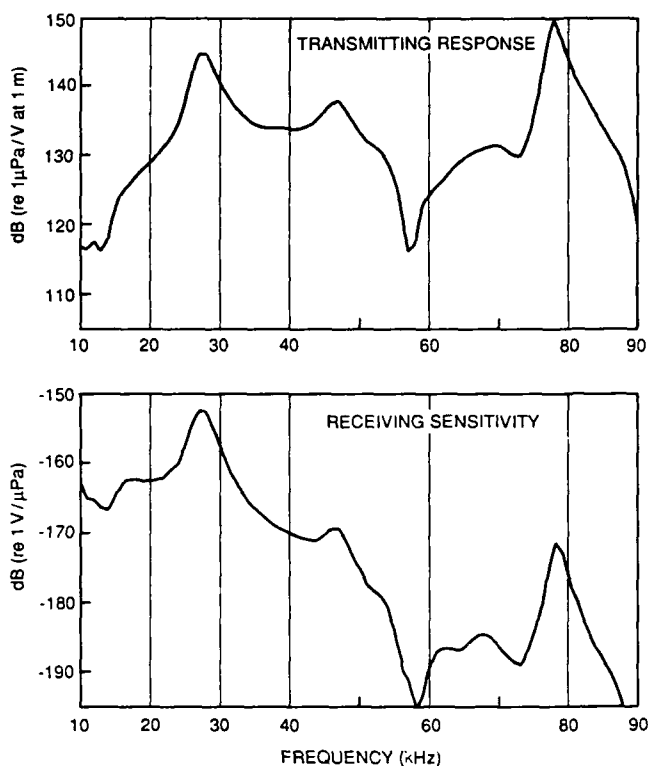


Figure 15.
Frequency response of the hemispherical transducer with 500 ft of cable, using transmit/receive box No. 2.

VI. CALIBRATION

A. From Air-Block Returns

A circular "air block" was created using an 86-cm diameter, 5-cm high, hollow metal cylinder with an open face on the bottom (see Figure 16). An attached pole was used to push the cylinder below the ice and indicate when it was level. It was then supplied with air through a hose until bubbles at the surface confirmed that it was full. The air-water interface at the lower surface of this cylinder should have remained very flat.

Reflections were measured in the same way as for the other blocks. The transducer, suspended 30 m below the block, was moved along a line estimated to pass through the block's axis. The location of the maximum return was noted. A perpendicular pass was then made through this location, and the maximum return again noted. This should have

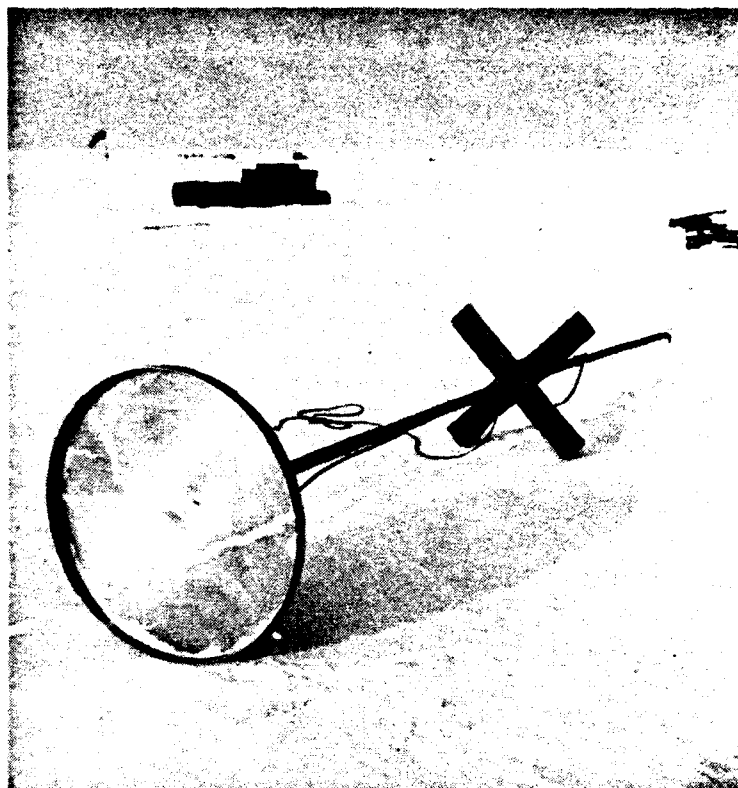


Figure 16. The metal cylinder used to form a block of air. Note the tubing used to force air into the cylinder from the surface.

been on the axis of the block, but another pass was made in the original direction for confirmation. If the maximum return did not occur as expected, the location of the new maximum was assumed to be correct without further checking.

After the position of maximum response was located, the transducer was moved along each of the two perpendicular directions through that position, stopping for a measurement every 15 cm along the positioning frame (15-cm movement of the ring along the frame corresponds to about 21-cm movement of the transducer). The transducer was then replaced by the alternate one, and the procedure repeated. The position of the transducer, the receiver gain, and the transmit voltage were recorded during each acoustic measurement. Some typical air-block returns for both transducers are shown in Figures 17 and 18.

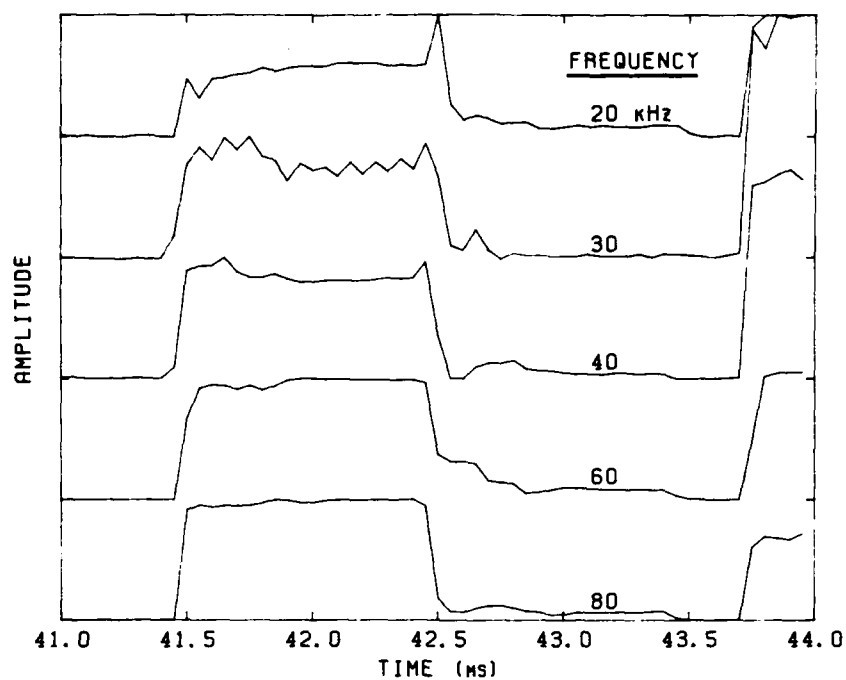


Figure 17. Returns from the air block, using the ITC transducer.

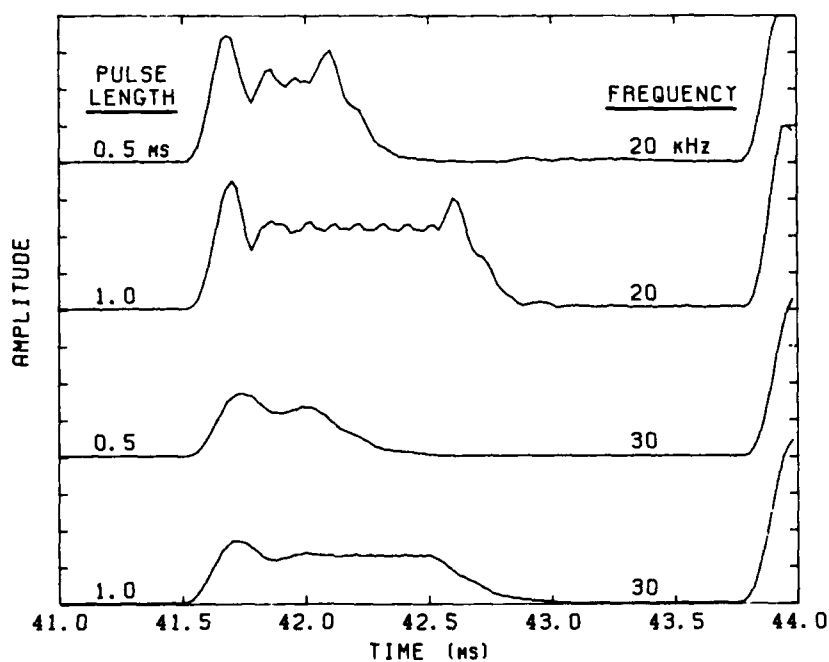


Figure 18. Returns from the air block, using the hemispherical transducer.

The target strengths at the five frequencies have been plotted, Figures 19–21, using transducer calibration constants that were adjusted to bring the entire angular response pattern into best agreement with theory—in this case rigid-plate theory^{3,4} adjusted slightly for a near-field geometry. (Rigid-plate theory applies also to a pressure release boundary.) The theoretical response is shown as a solid line in Figures 19–21. The calibration constants used at each frequency are listed in Table II.

The target strengths at normal incidence in Figures 19–21 are plotted in Figure 22. These particular values are not in exact agreement with theory because the best fit was made to the entire response pattern. The low values for Run 20 may be due to the transducer not crossing through the peak of the response (by 30 cm) or could arise from almost any alteration or disturbance to the flat air–water interface. (The return is more sensitive to irregularities in the surface at the higher frequencies.) The air-block calibrations are estimated to have an accuracy of 1 dB.

The near-field correction shown in Figure 22 was calculated by numerically integrating³ the return from the face of a hypothetical block, taking into account the phase relationships when summing the contributions from all the elements of the block face. The method is described in Appendix A.

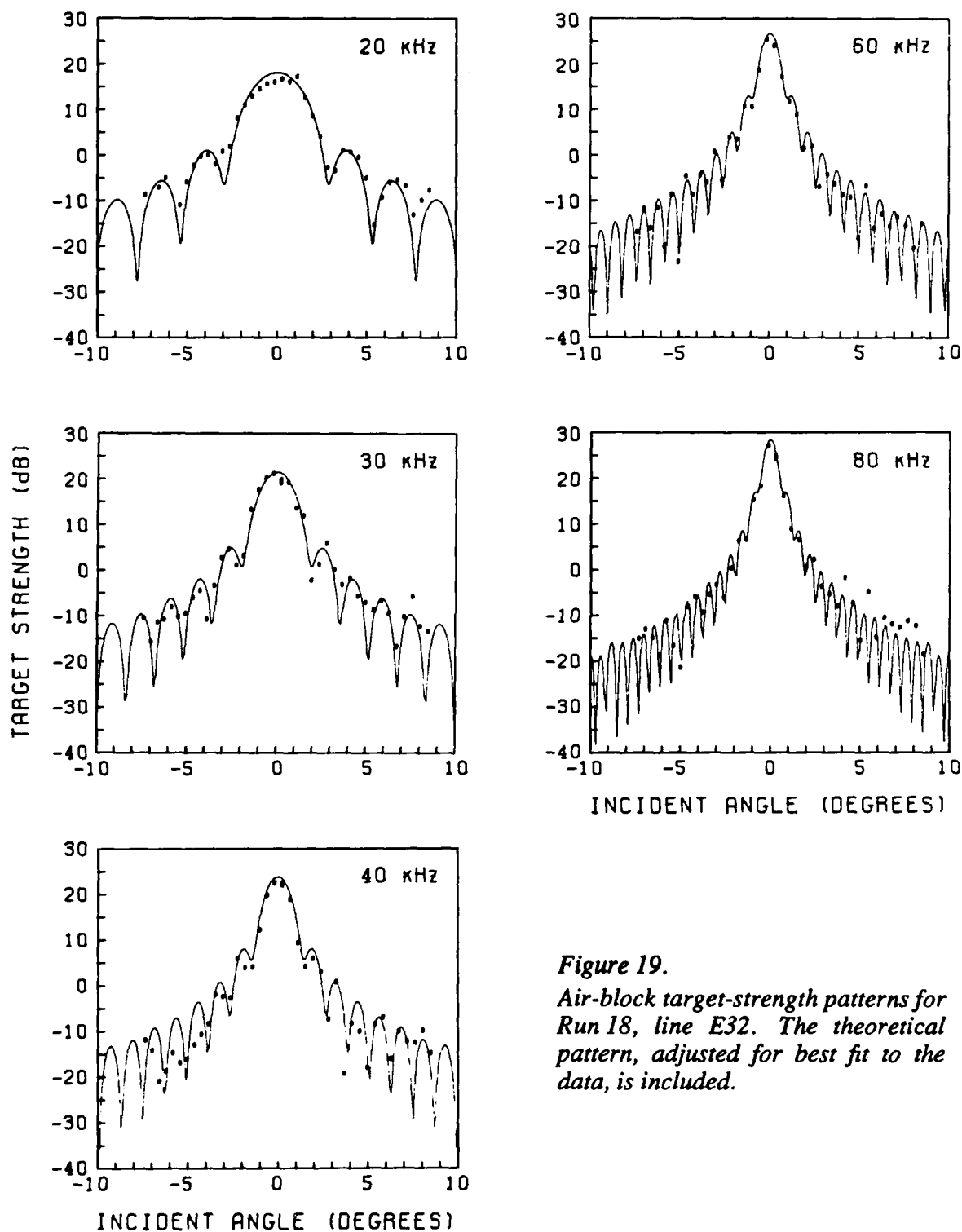


Figure 19.

Air-block target-strength patterns for Run 18, line E32. The theoretical pattern, adjusted for best fit to the data, is included.

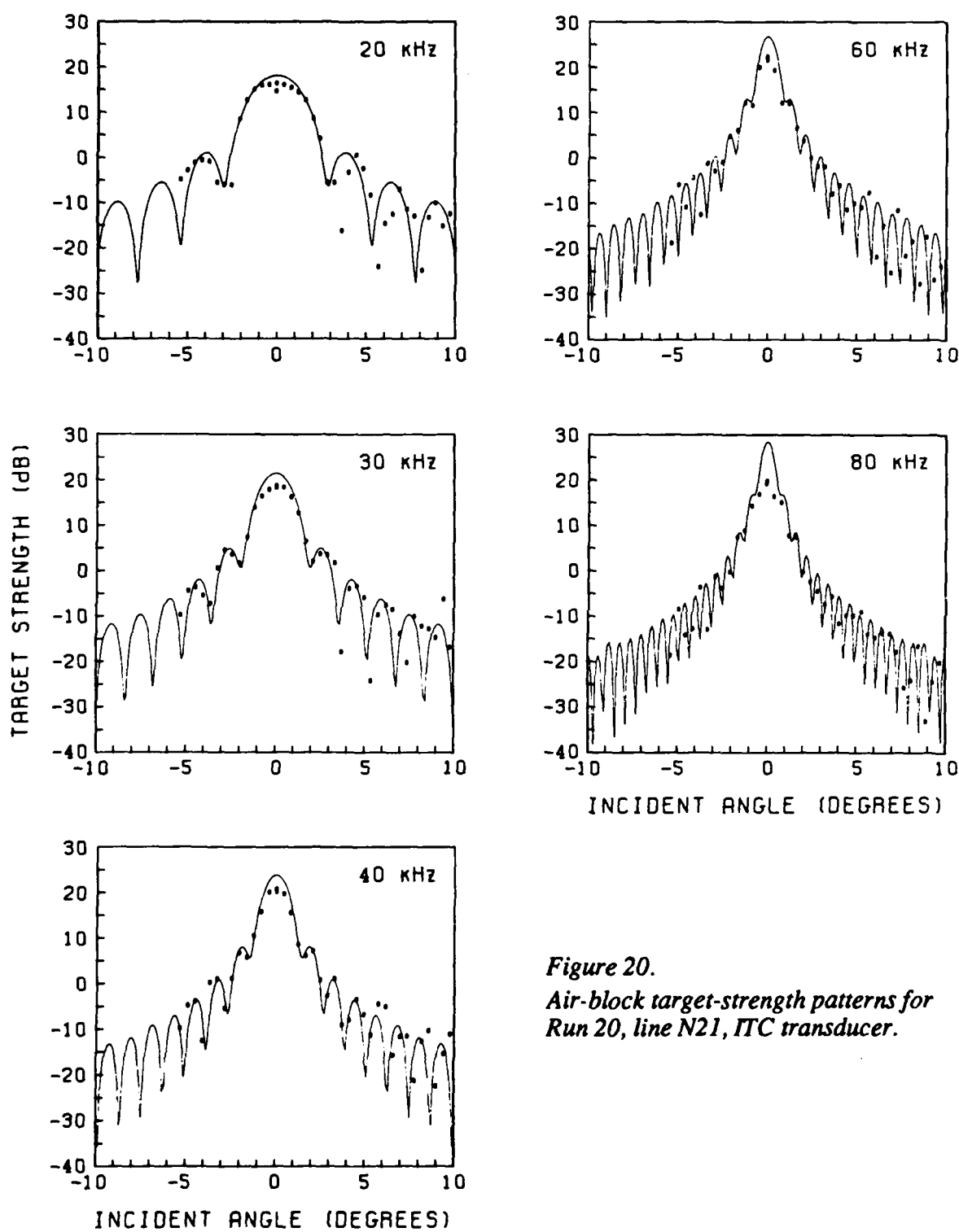


Figure 20.
Air-block target-strength patterns for
Run 20, line N21, ITC transducer.

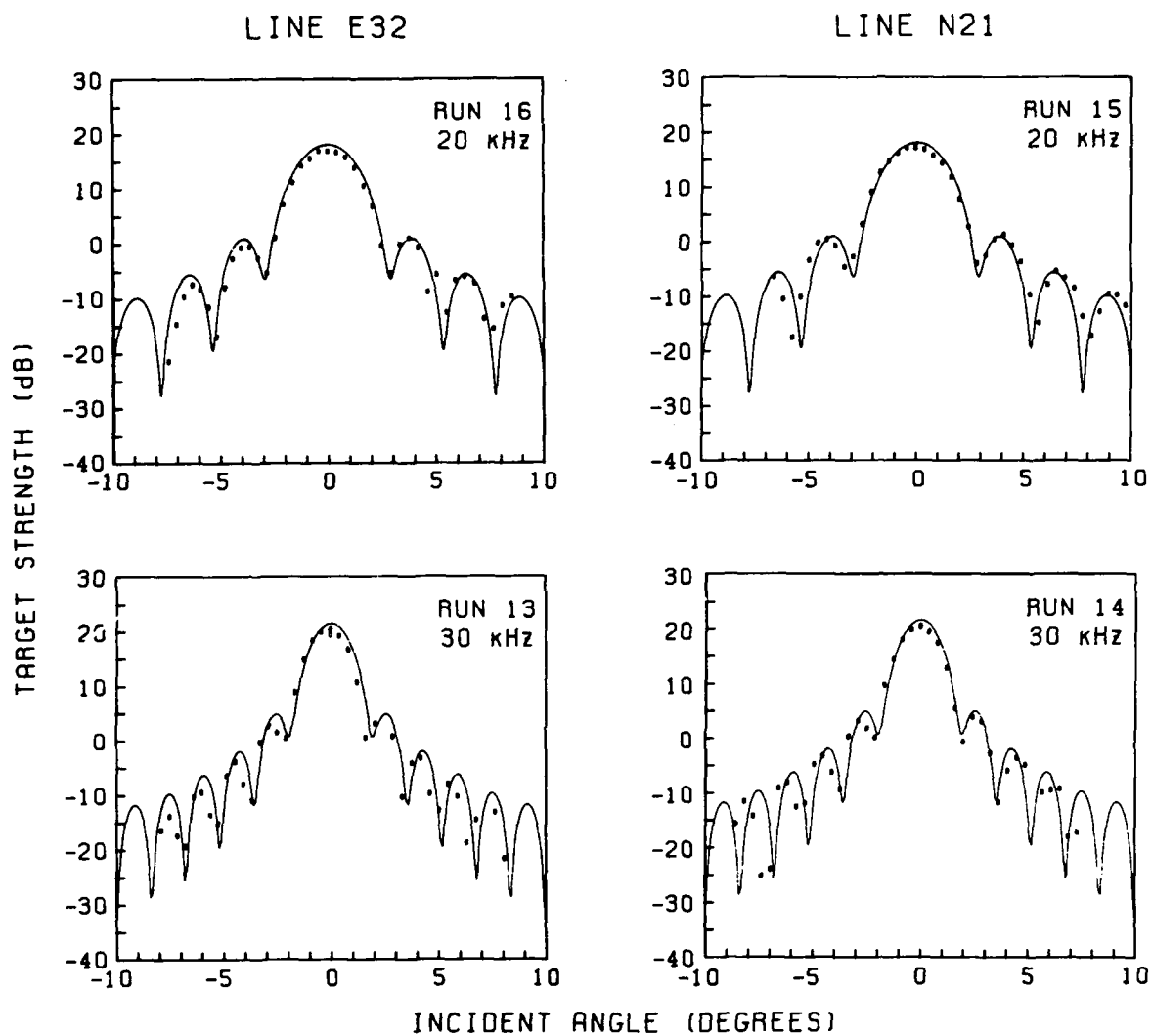


Figure 21. Air-block target-strength patterns for Runs 13-16, hemispherical transducer.

Table II. Combined transmitting response and receiving sensitivity as determined from the air-block returns.

Transducer	Frequency (kHz)	Air Block Calibration Constant (dB)
ITC 1042	20	-78
	30	-76
	40	-69
	60	-57
	80	-55
Hemisphere	20	-66
	30	-55
Water Temperature	--	-1.6°C

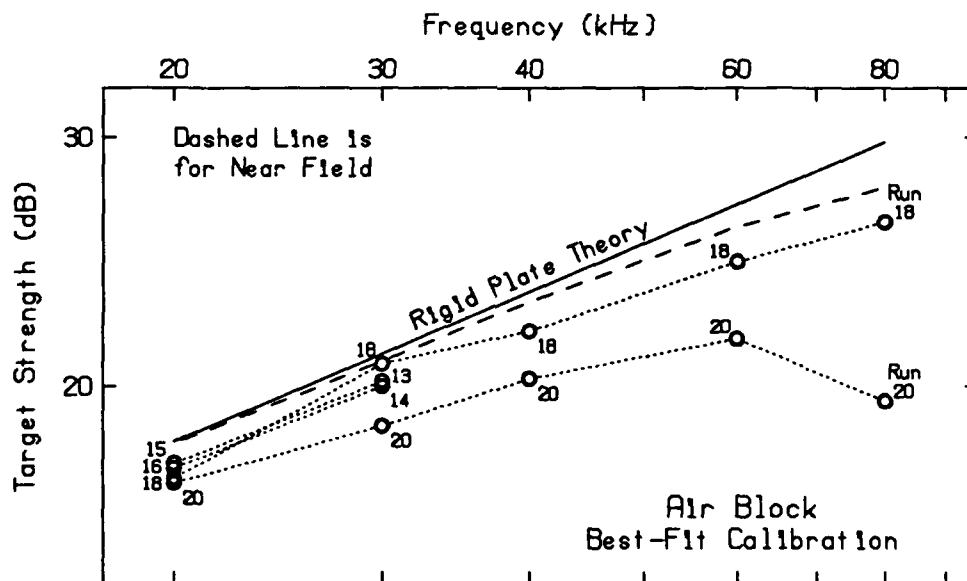


Figure 22. Air-block target strength at normal incidence with transducer calibration adjusted for best fit to the entire pattern of the return.

B. From Sphere Returns

A stainless steel, Freon-filled sphere was installed below the blocks to provide a continual check on calibration. (Freon focuses the energy onto the back side of the sphere's interior and thus provides a higher target strength than an air-filled sphere.) We discovered later, however, that the sphere had split open the first day, when the cold Freon used to fill the sphere was warmed by the water and expanded. At the close range of the measurements, the flooded sphere still served as a good reference for each run and gave nearly the same target strength at all frequencies when calculated using the air-block calibration.

The target strength of the sphere during several of the runs is shown in Figures 23–27. The returns are close enough to the same strength to give confidence that the target strengths determined for the ice blocks are consistent to ± 2 dB.

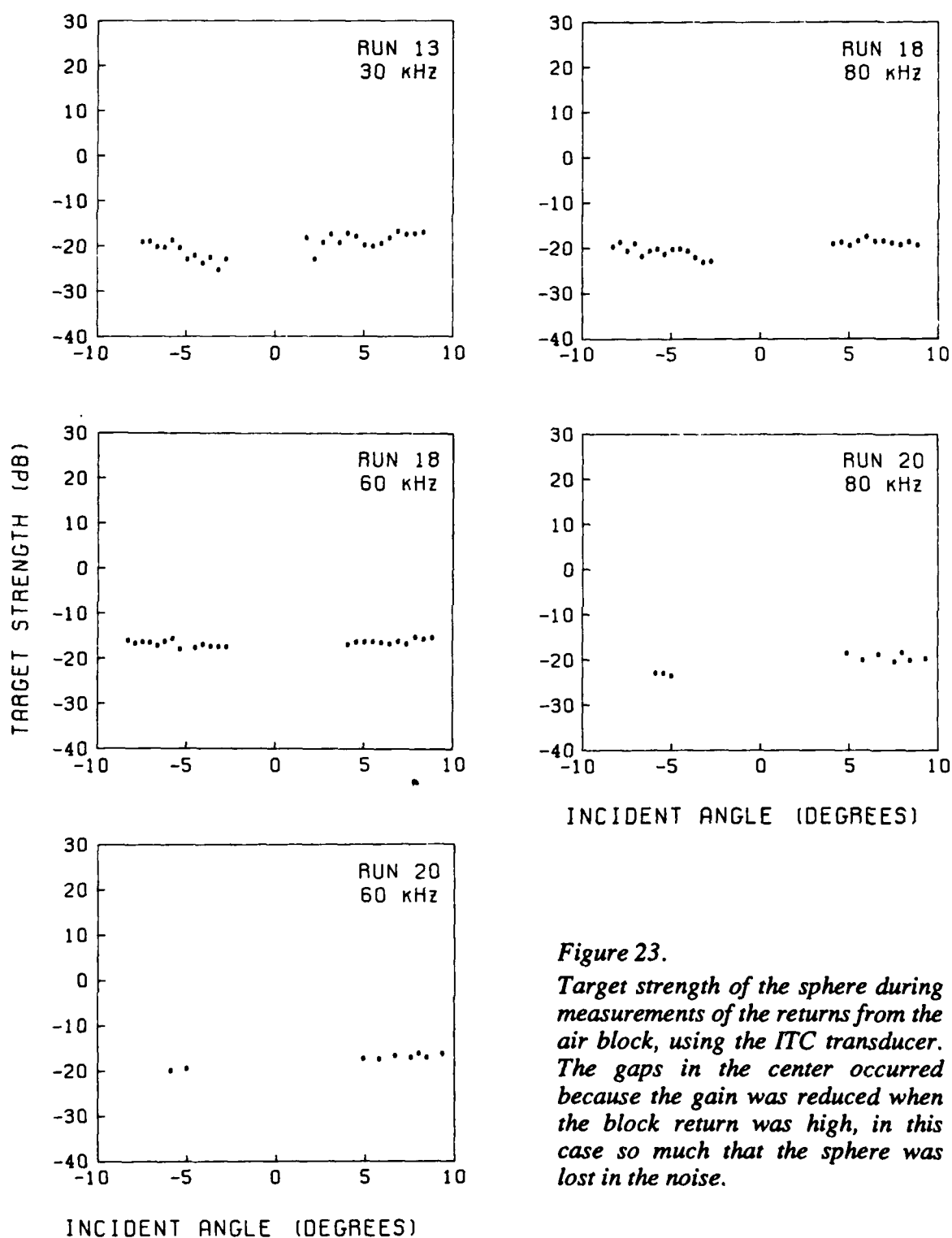


Figure 23.

Target strength of the sphere during measurements of the returns from the air block, using the ITC transducer. The gaps in the center occurred because the gain was reduced when the block return was high, in this case so much that the sphere was lost in the noise.

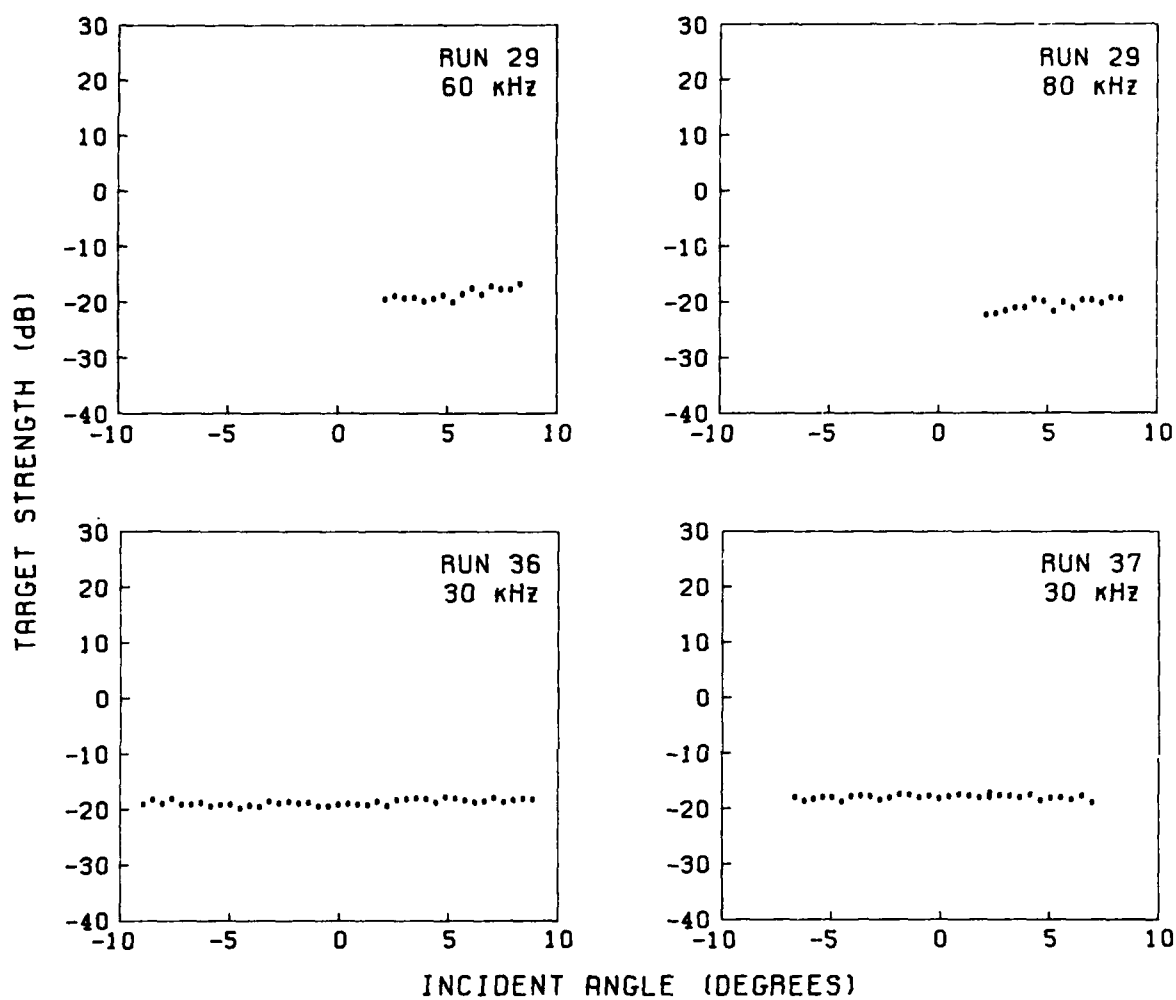


Figure 24. Target strength of the sphere during measurements of the returns from the 40-cm block, using the ITC transducer.

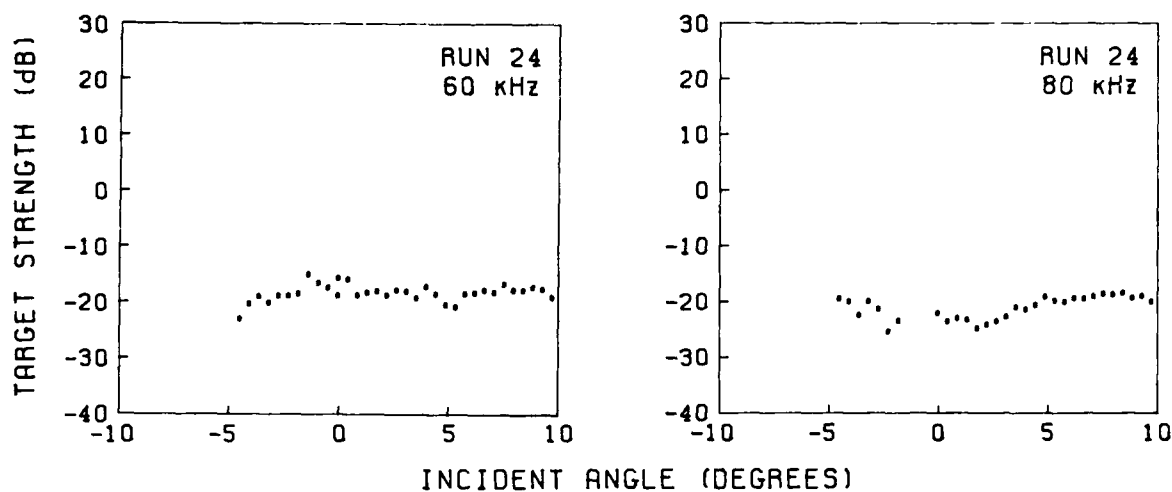


Figure 25. Target strength of the sphere during measurements of the returns from the short block (described in Section VII A), using the ITC transducer.

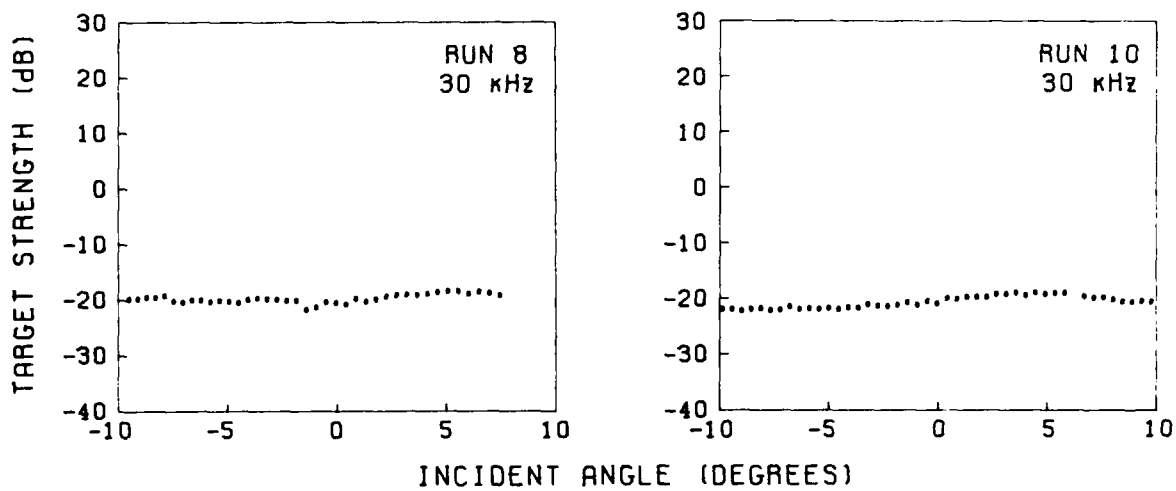


Figure 26. Target strength of the sphere during measurements of the returns from the 84-cm block, using the ITC transducer.

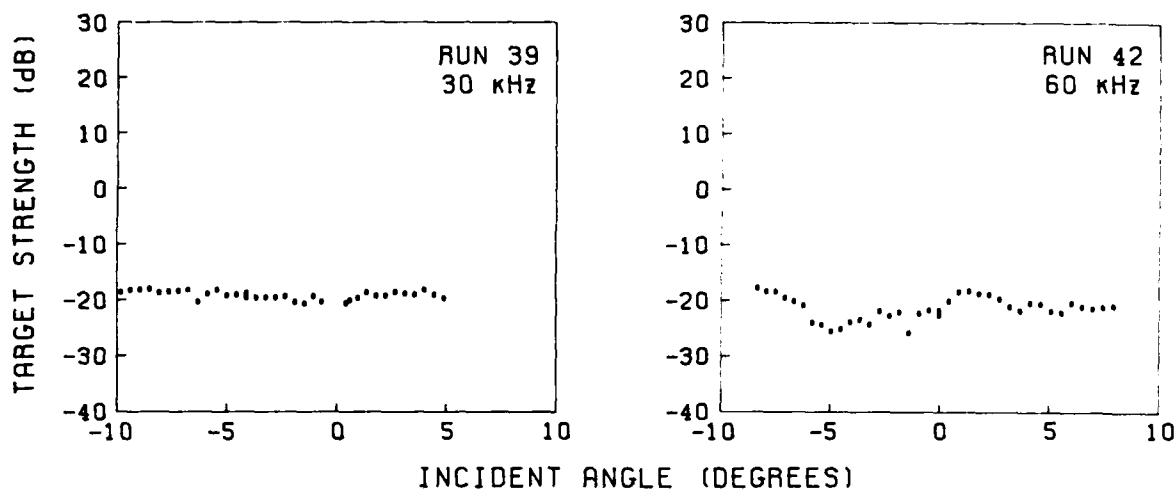


Figure 27. Target strength of the sphere during measurements of the returns from the 109-cm block, using the ITC transducer.

VII. MEASUREMENTS

Each block, in turn, was installed and left in place for several hours while acoustic reflections were measured. After each return was examined, and an average amplitude estimated, the target strength of the block face was calculated. When the measurements were complete, the block was removed so it would not interfere with the next measurements.

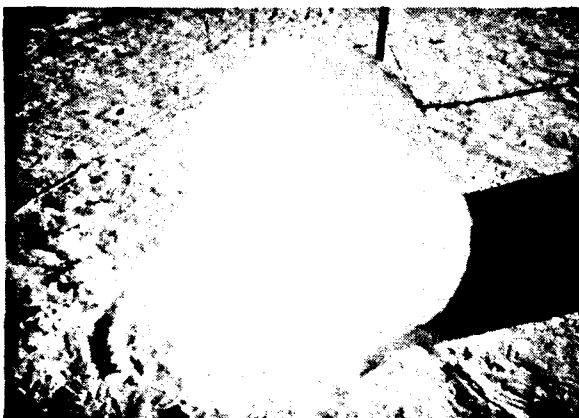
A. Short Block with Skeletal Layer Removed

The short block (Figure 28) was obtained by sawing off both ends of the block that was removed to make the diver entry hole. The sawed face was quite smooth, but the saw veered off near the end of the cut to produce a rounded surface (concave from below). Three attempts to saw straighter gave no improvement. The short block remained in the cold air for a few days before it was submerged and undoubtedly cooled considerably. After it was submerged, it had only a few hours to warm in the water before the reflections were measured. Thus a glaze of ice may have formed on the lower surface and altered the reflections.



Figure 28.

The short block (standing on edge) made by sawing off both ends of the block removed for the diver entry hole.



Only the ITC transducer was used for the short-block measurements. A sample of the returns is shown in Figure 29.

The target strength calculated from the short block returns at normal incidence is plotted in Figure 30. The drop at 80 kHz seems excessive. It may be caused by large-scale variations in the block's surface that become appreciable with respect to the wavelength (1.8 cm). The fine-scale surface roughness was too small to cause such a drop.

The short-block target-strength patterns are shown in Figures 31 and 32. There is considerable difference between the two orthogonal directions of transducer movement. The peaks of the returns have about the same amplitude, but the return in one direction (Figure 32) has a sidelobe pattern and the other does not.

The results are similar to what would be obtained if half the face were rounded off like the surface of a cylinder. Figure 33 shows the results computed numerically, by the method outlined in Appendix A, for passes at 20 and 60 kHz in directions perpendicular and parallel to the axis of a cylindrical shape that results in a 2-cm addition of ice at the edge. The results are similar to those observed. Such a north-east contrast requires that we by chance oriented the block with the axis of the cylindrical cut within 20° of either one of the frame axes—a chance of 40/90.

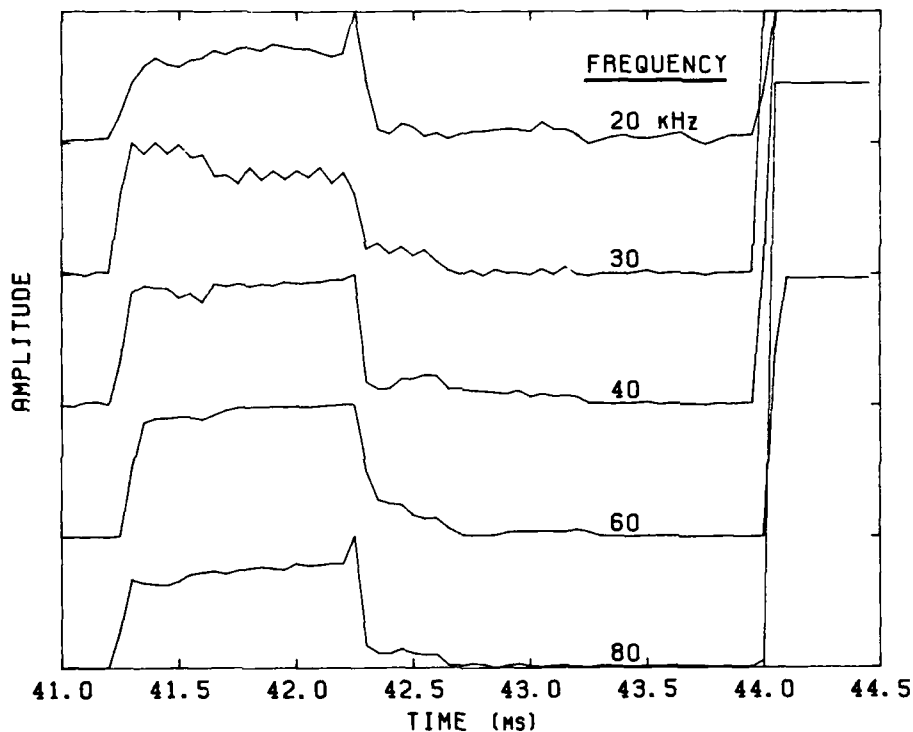


Figure 29. Returns from the short block using the ITC transducer.

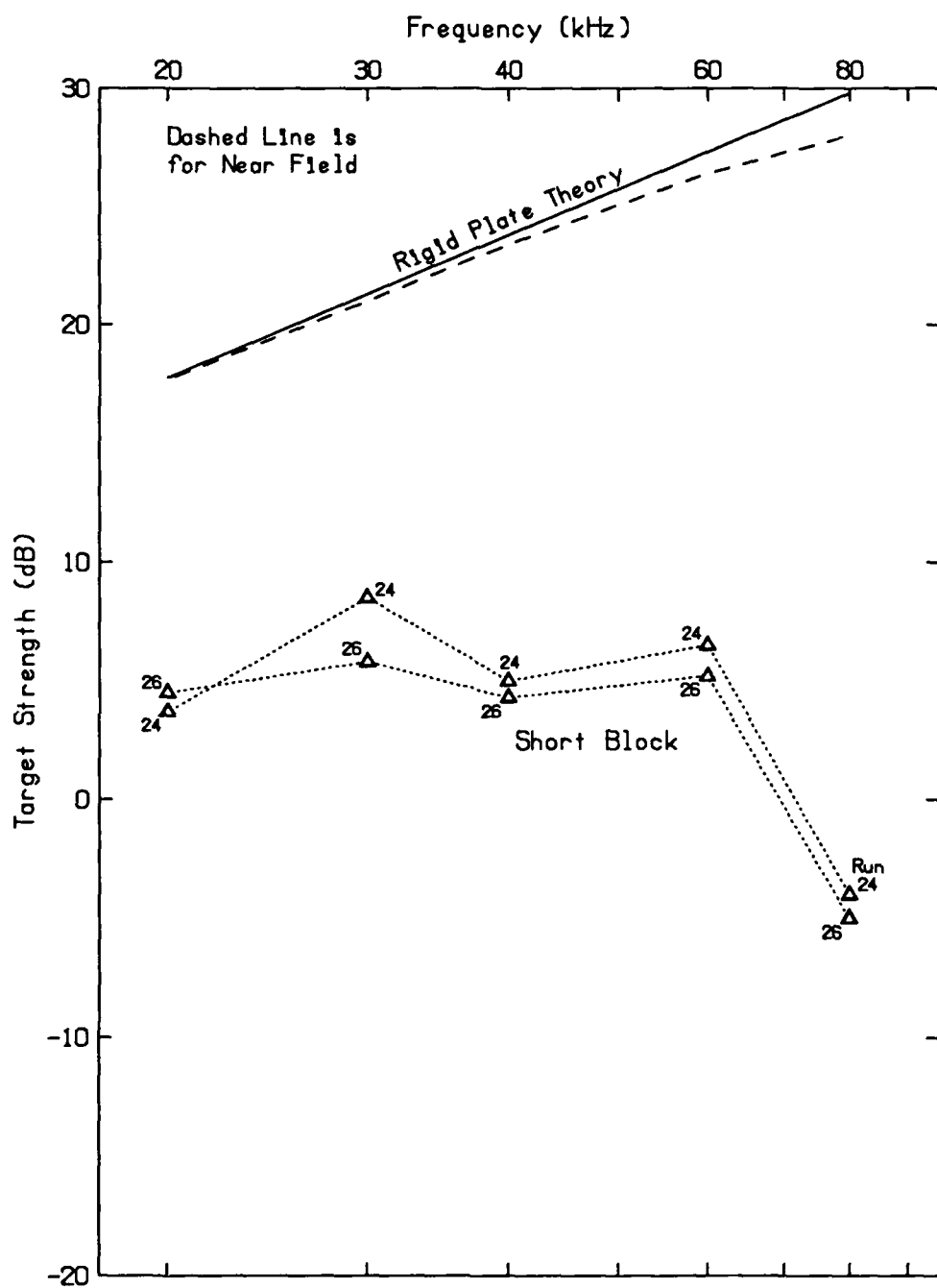


Figure 30. Short-block target strength at normal incidence using the ITC transducer.

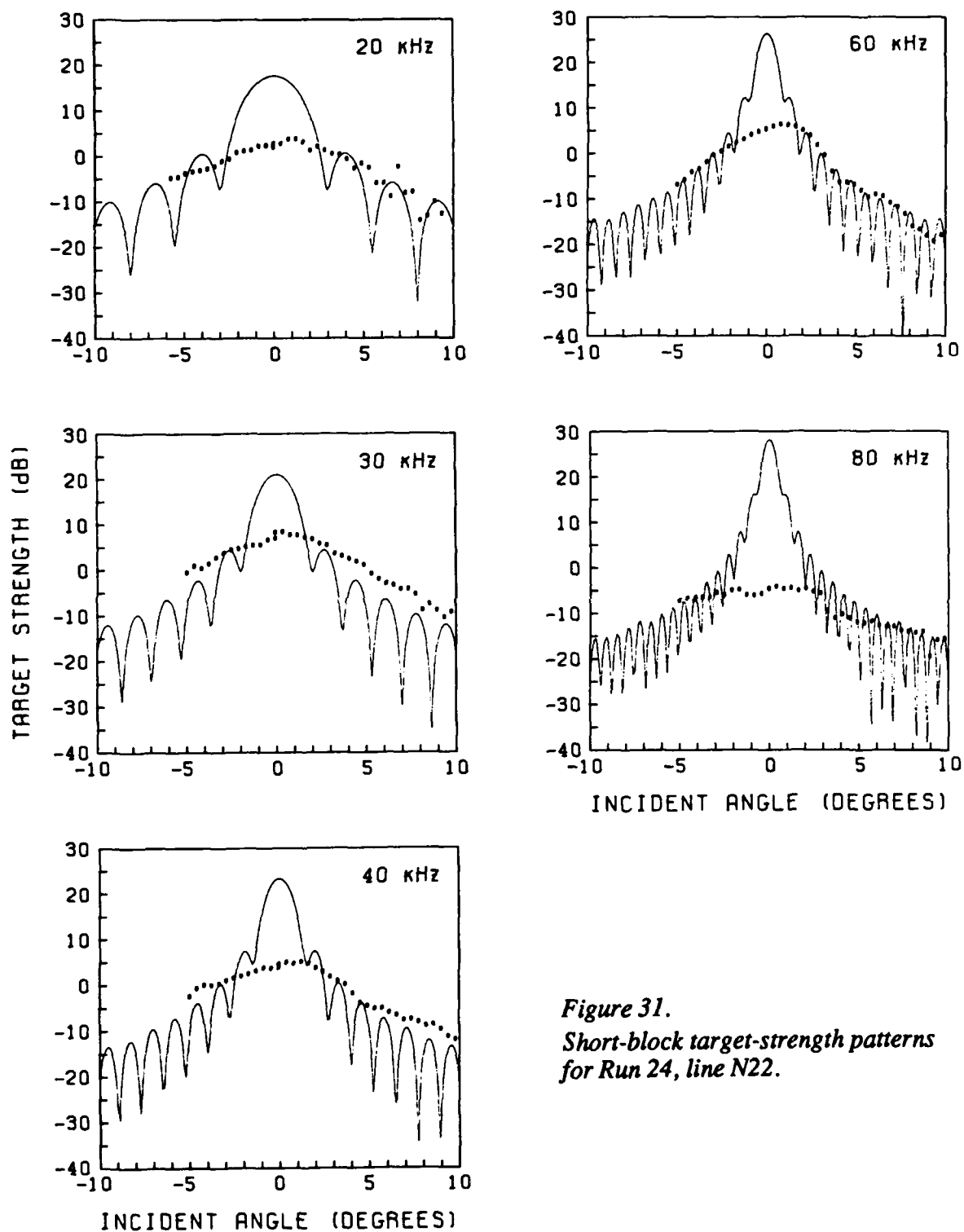


Figure 31.
Short-block target-strength patterns
for Run 24, line N22.

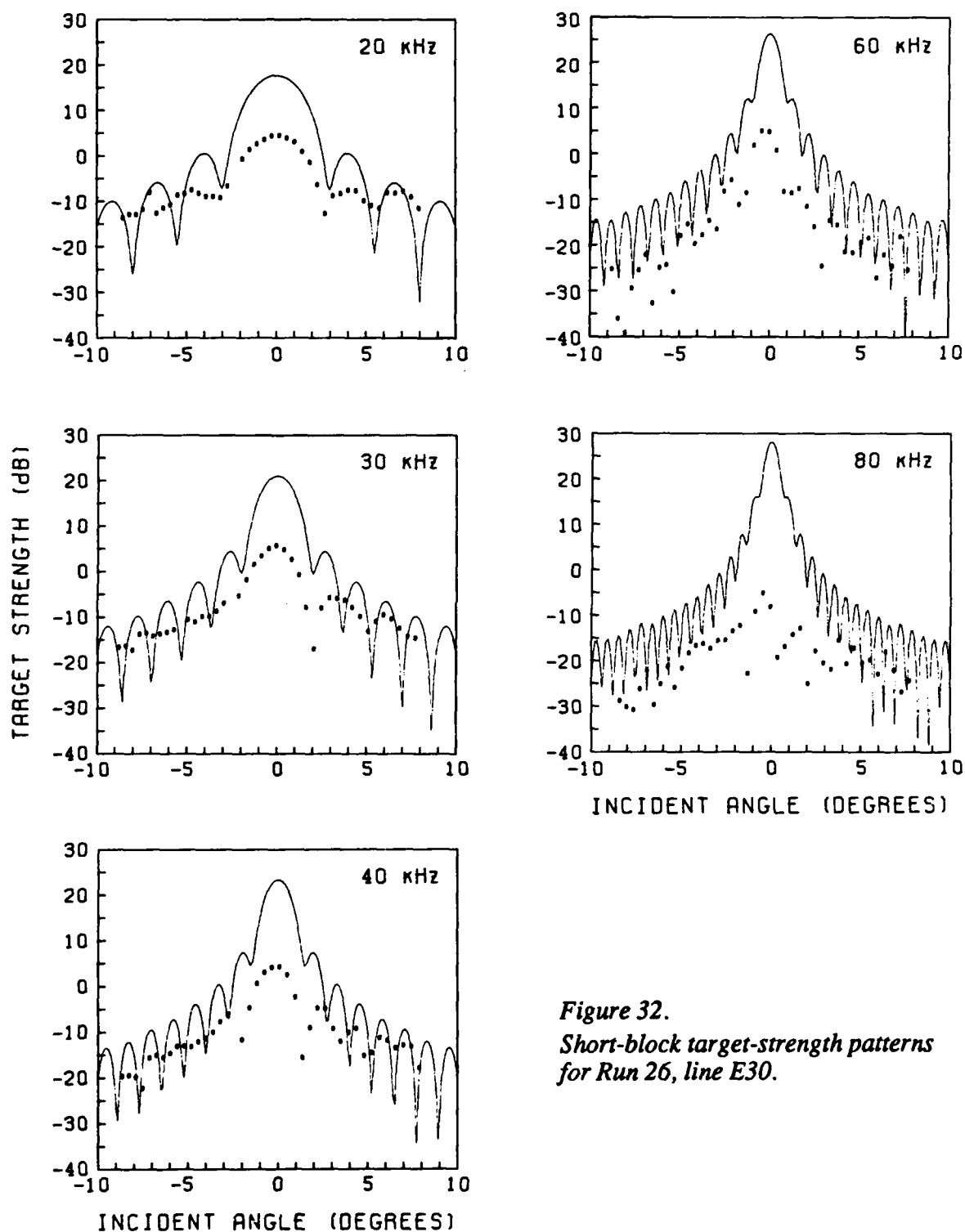


Figure 32.
Short-block target-strength patterns
for Run 26, line E30.

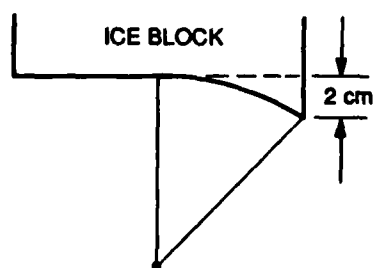
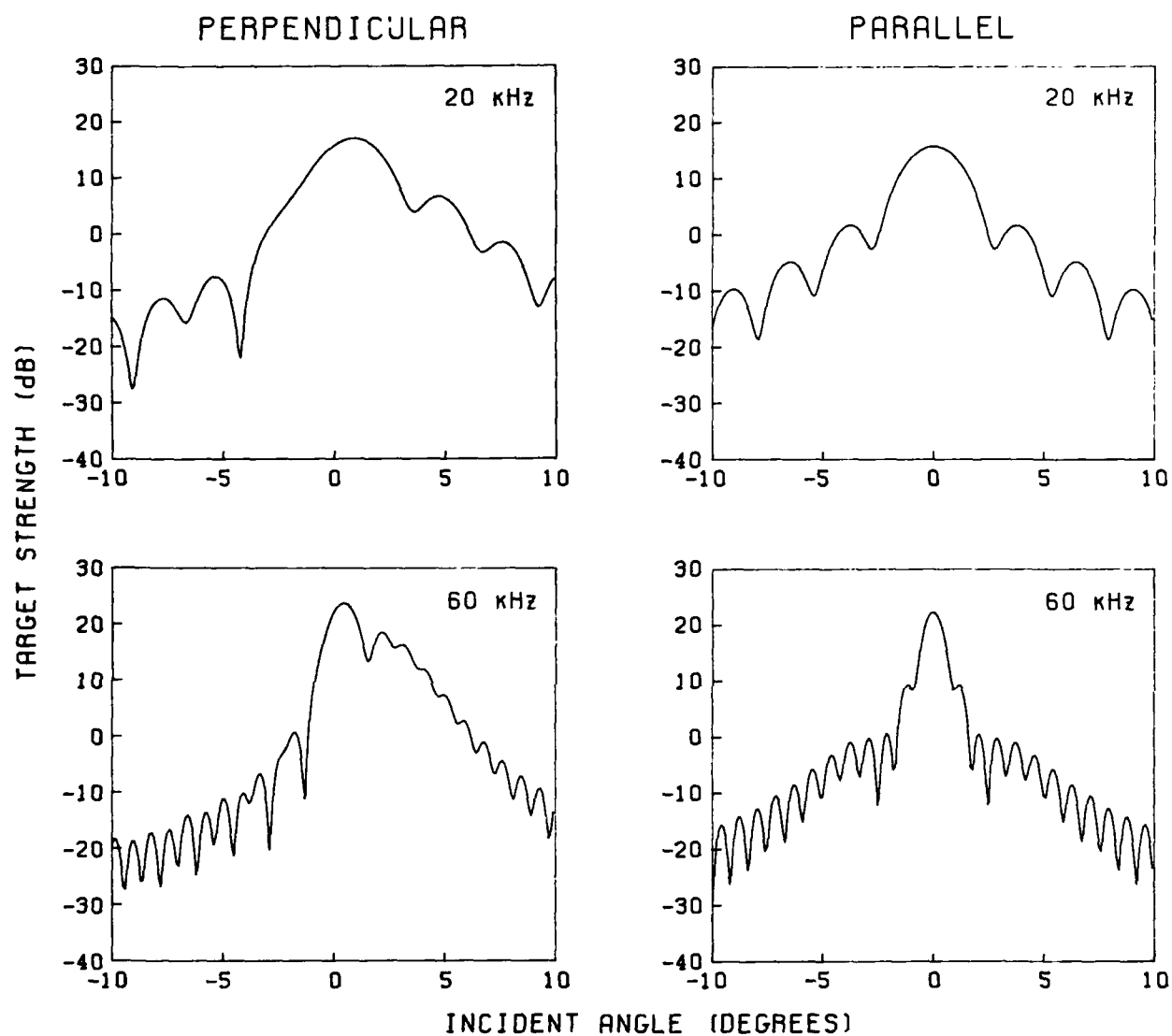


Figure 33.

Predicted patterns for a block that was formed with a cut that was cylindrical on one side, adding 2 cm at the edge.

B. The 84-cm Block

This block was the same diameter as that used in the pilot experiment in 1984. It was selected as the first measurement in the present experiment because the hole was needed for the air-block and short-block tests.

At the beginning, each transducer pass measured returns at a single frequency. Later, the method was improved so that five frequencies could be used in succession for the ITC transducer, or two pulse lengths at 20 and 30 kHz each for the hemisphere; thus only one transducer pass each way was required to measure up to five acoustic returns at various frequencies and pulse lengths.

Some examples of the returns at normal incidence from the 84-cm block are shown in Figures 34 and 35. The rise of the return is as fast as for the air block, indicating that the reflecting surface is distinct. For the higher frequencies, the reflection from the upper face is distinguishable about 1 ms later (see Section IX).

The pulses from the ITC transducer were square, but those from the hemispherical transducer had an initial high peak and a second lower one because of competing vibrational modes. This shape also was seen when monitoring the ac voltage applied to the transducer. The ITC pulse often had a high short peak at the end which occasionally appeared in the return. When reading the return for the hemispherical transducer, it was advantageous to use a 1-ms pulse and read the amplitude of the latter half, which was more consistent.

The target strengths at normal incidence are shown in Figure 36. At 40 kHz, the target strength begins to fall off as if the wavelength (3.6 cm) were small enough to detect the ice roughness, and this falloff increases at 60 and 80 kHz. The 30 kHz result for the hemispherical transducer seems low, but discrepancies would be expected when operating so close to a resonance (see Figure 15) that is temperature sensitive.

The patterns of the returns are shown in Figures 37–39. The returns were expected to be about 10 dB lower than those predicted by the rigid-plate theory because of the impedance mismatch between water and ice, but they are 23–37 dB lower. There is a central peak but little indication of nulls and side lobes. At high angles, the low returns often merge with the noise.

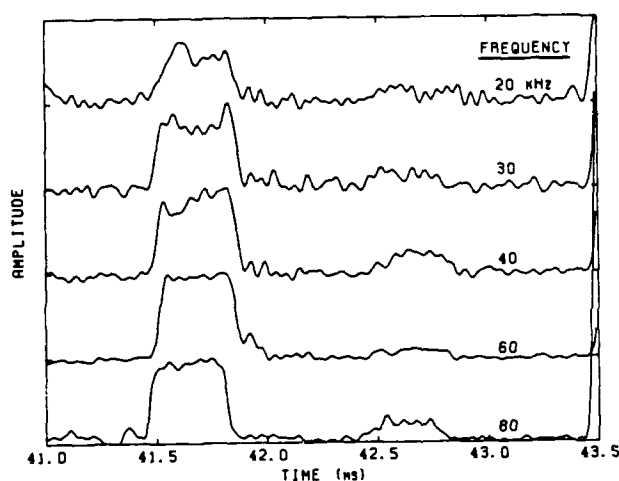


Figure 34.
Returns from the 84-cm block, using the ITC transducer and a 0.35 ms pulse.

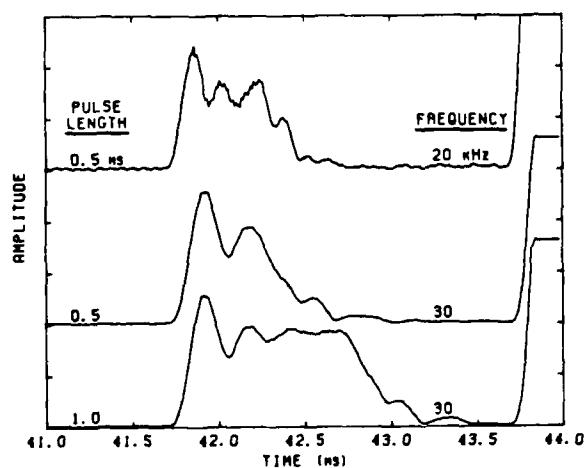


Figure 35.
Returns from the 84-cm block, using the hemispherical transducer.

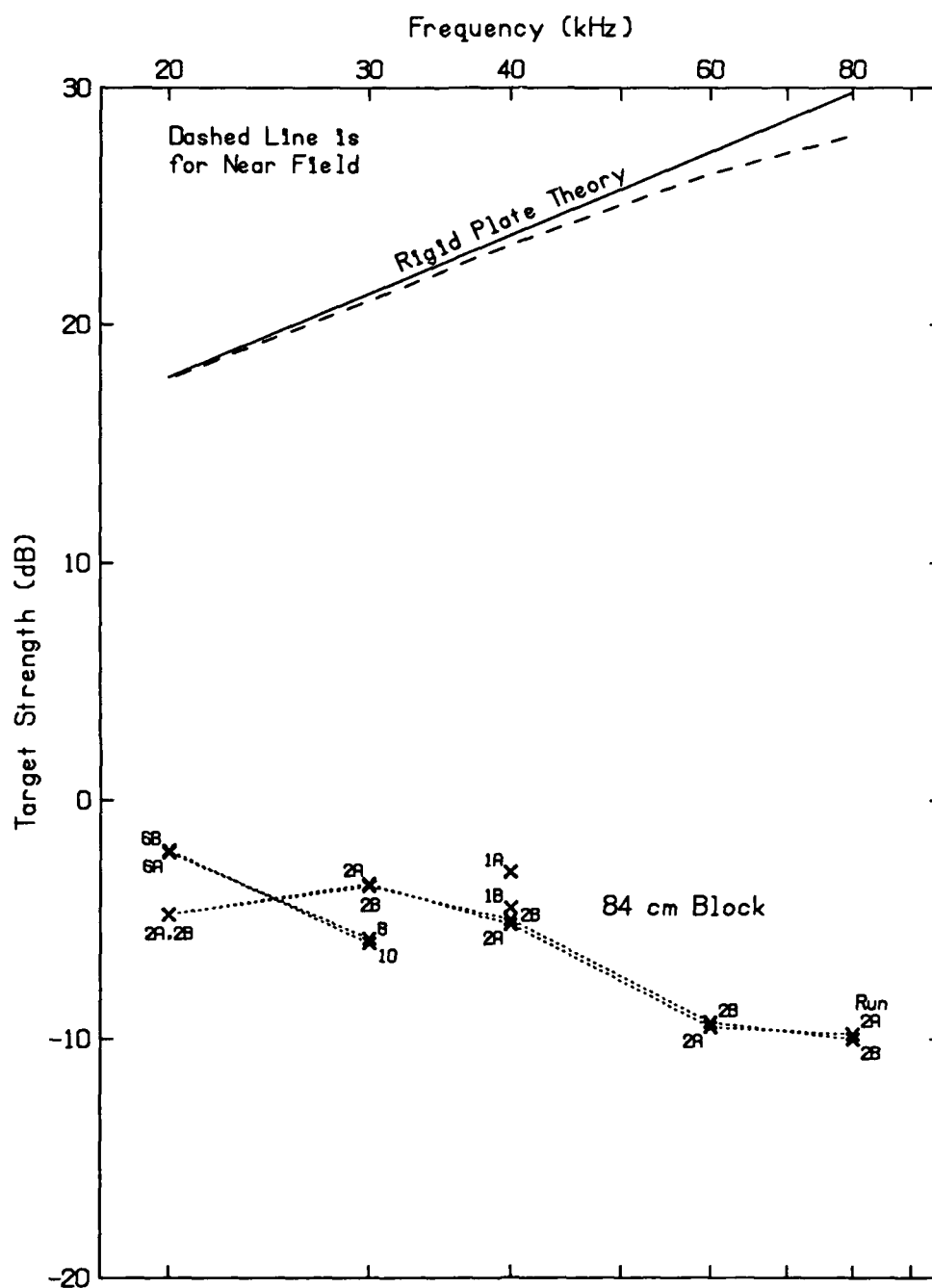


Figure 36. Target strengths of 84-cm block at normal incidence.

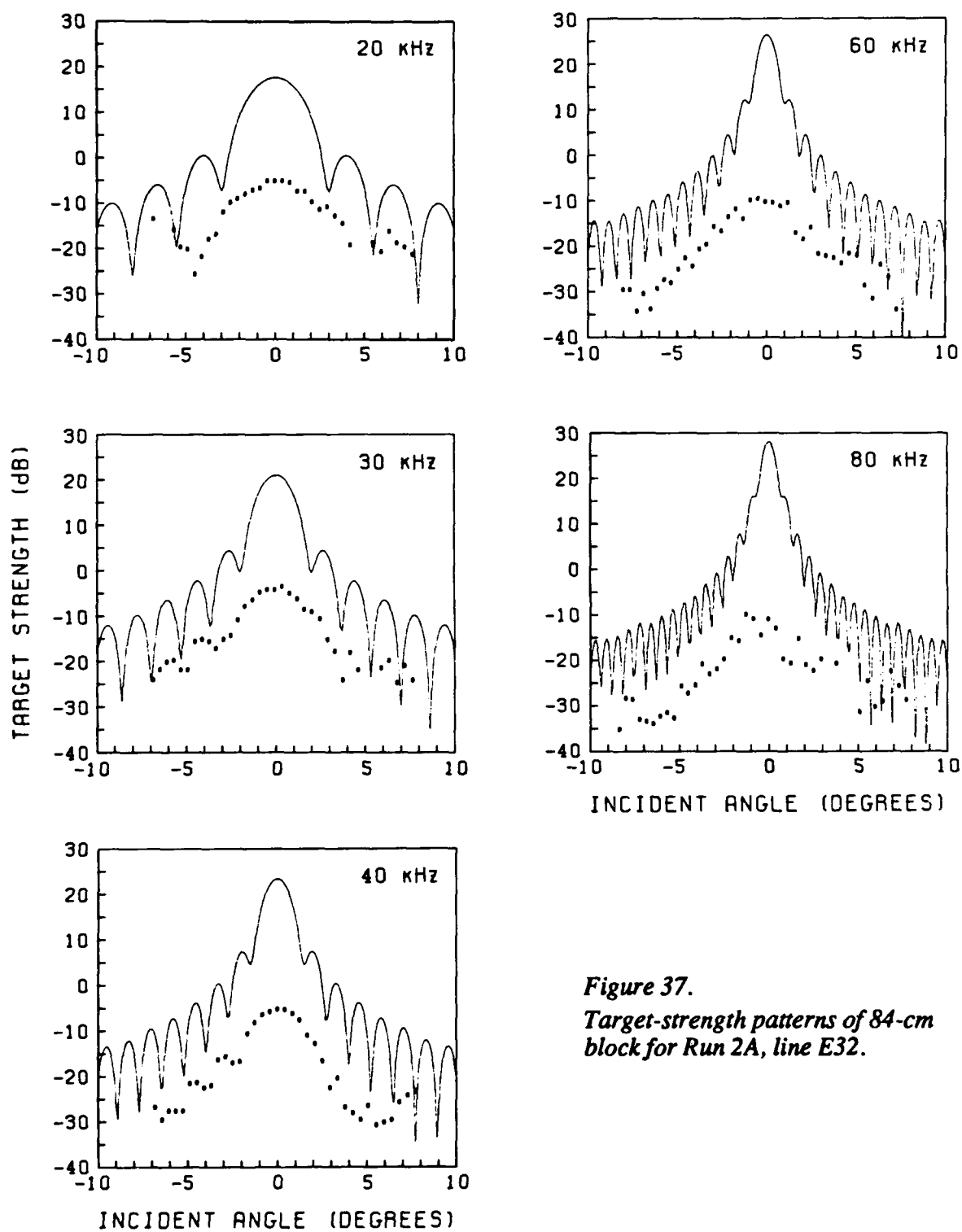


Figure 37.
*Target-strength patterns of 84-cm
block for Run 2A, line E32.*

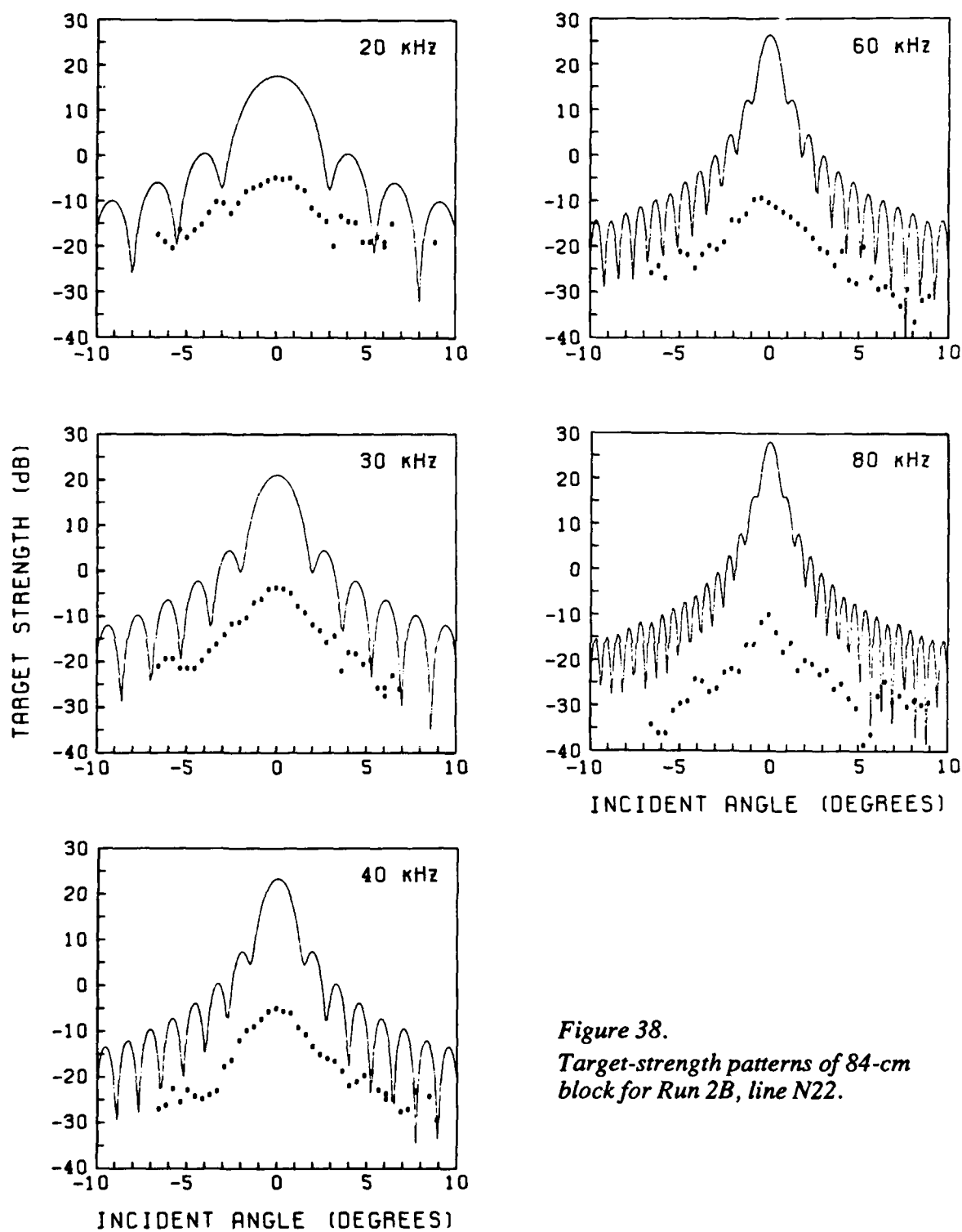


Figure 38.
Target-strength patterns of 84-cm
block for Run 2B, line N22.

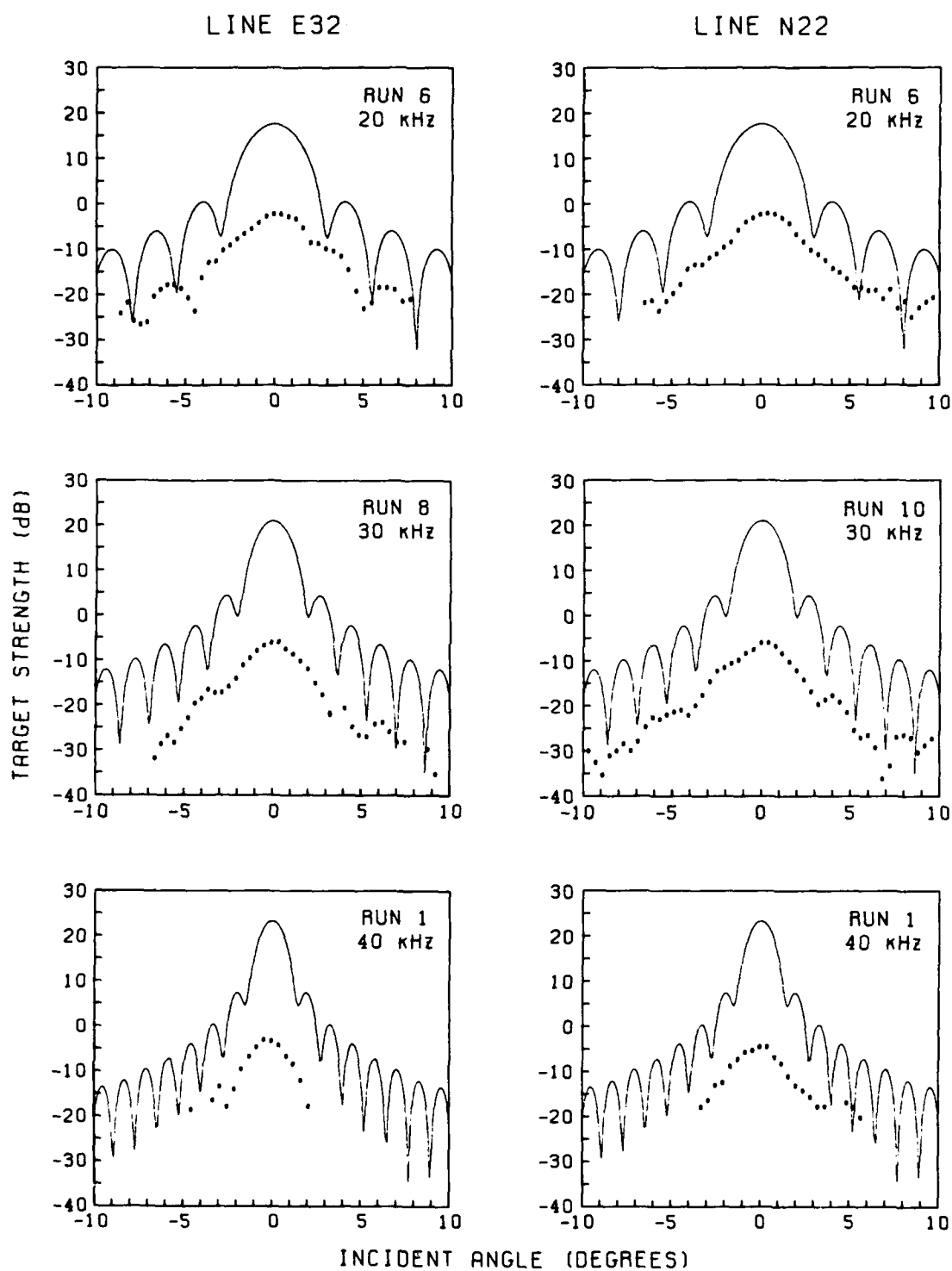


Figure 39. Target-strength patterns of 84-cm block for Runs 1, 6, 8, and 10.

C. The 40-cm Block

The 40-cm block was prepared in a similar fashion. The normal-incidence returns are shown in Figures 40 and 41; the target strengths at normal aspect are shown in Figure 42, and the patterns are shown in Figures 43–45.

This block gave returns even higher than the larger blocks. Some possible reasons for this are discussed in Section VIII.B. The patterns show distinct nulls and side lobes. At the lower frequencies, the predicted loss of 9.5 dB due to impedance mismatch seems sufficient to account for all the loss. At 60 and 80 kHz, the loss is much greater, 14 and 17 dB respectively.

D. The 109-cm Block

The 109-cm block was the last one measured. The normal-incidence returns are shown in Figures 46 and 47, the normal-incidence target-strength results in Figure 48, and the response patterns in Figures 49–51. Several of the patterns level off at a minimum value, which was apparently the noise level.

These patterns do not have a good central peak, nor do they have well-defined side lobes. It appears that a block face of this size does not reflect as a flat plate.

This completed the planned experiments, but there was enough time left for a change in range. All three lines were shortened by a given amount to raise the transducer, first to 20 m below the ice block and then to 15 m. The ITC transducer was moved in steps to locate the center of the block and then across in one direction only. The target-strength patterns are shown in Figures 52 and 53 for ranges of 20 m and 15 m, respectively. The theoretical patterns were corrected for near-field effects at each range.

As a finale, the transducer, still 15 m below the ice block, was moved back across for a second pass. The patterns (Figure 54) show a much stronger peak than on the first pass (Figure 53), which is difficult to understand as no changes were made in the equipment between the two passes.

The returns at normal incidence for all the ITC runs with the 109-cm block are compared in Figure 55. The data points have not been corrected for near-field effects, which are shown near the top of the figure. The agreement between the results for Runs 42–48, which involved three ranges, indicates that the shorter-range returns had no near-field reduction. Apparently, the return was already so incoherent that being near-field caused no additional reduction.

The difference between Figures 53 and 54 is disturbing. Checks on the returns from the sphere at 40, 60, and 80 kHz show that they were well above the noise level and agreed within 2 dB for the two runs. Looking further for an explanation of the difference, we compared the pulses received near normal incidence (Figure 56). In general, the shapes of the returns are about the same.

Figures 49 and 50 show that the response pattern for the 109-cm block did not show a well-defined central peak, and thus the peak would have been difficult to find. It may be that Run 50 passed through a peak and Runs 42, 44, 46, and 48 were off to one side by half a meter. This is a larger error than expected, but perhaps a strong current caused a translocation of the transducer between Runs 48 and 50, or perhaps we accidentally made the last pass on a different frame line. Ordinarily the highest return would be considered the most valid because there are many causes for reduced returns and few for a higher return. When the preceding runs for both the 84-cm and 109-cm blocks all show low values, however, the choice is difficult. When we compare the results for different sized blocks in the next section, the short-range measurements are omitted (i.e., Runs 45, 48, and 50).

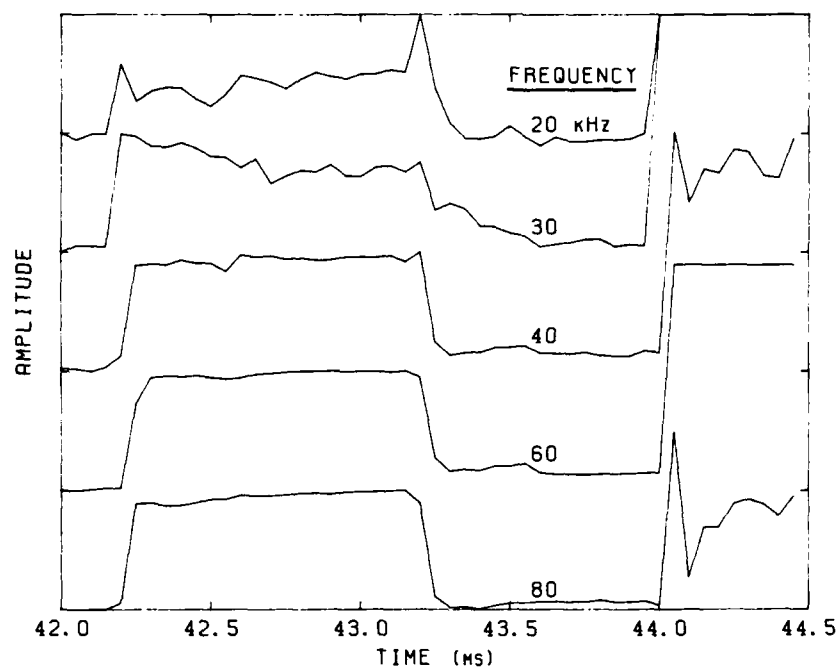


Figure 40. Returns from the 40-cm block, using the ITC transducer.

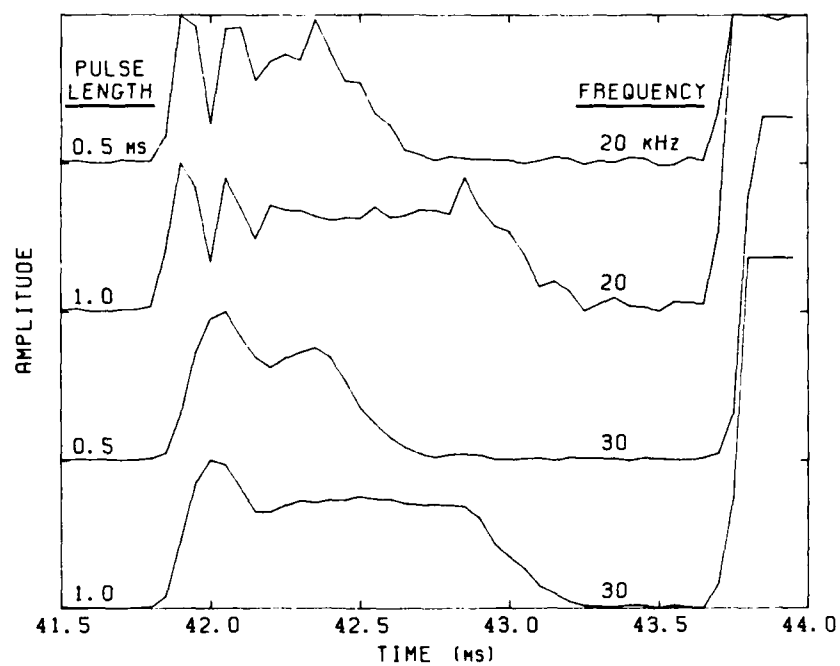


Figure 41. Returns from the 40-cm block for two pulse lengths and two frequencies, using the hemispherical transducer.

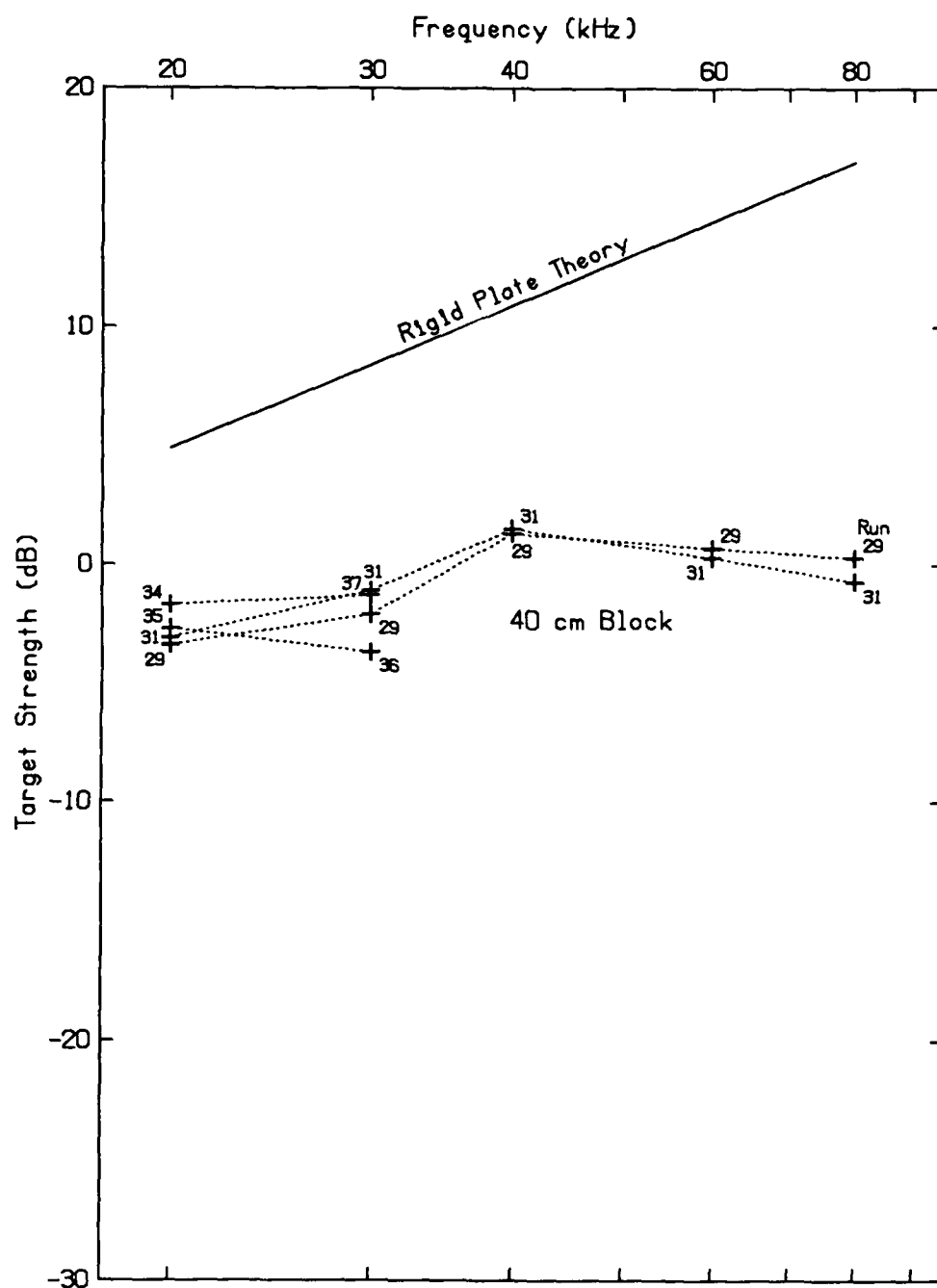


Figure 42. Target strengths of 40-cm block at normal incidence.

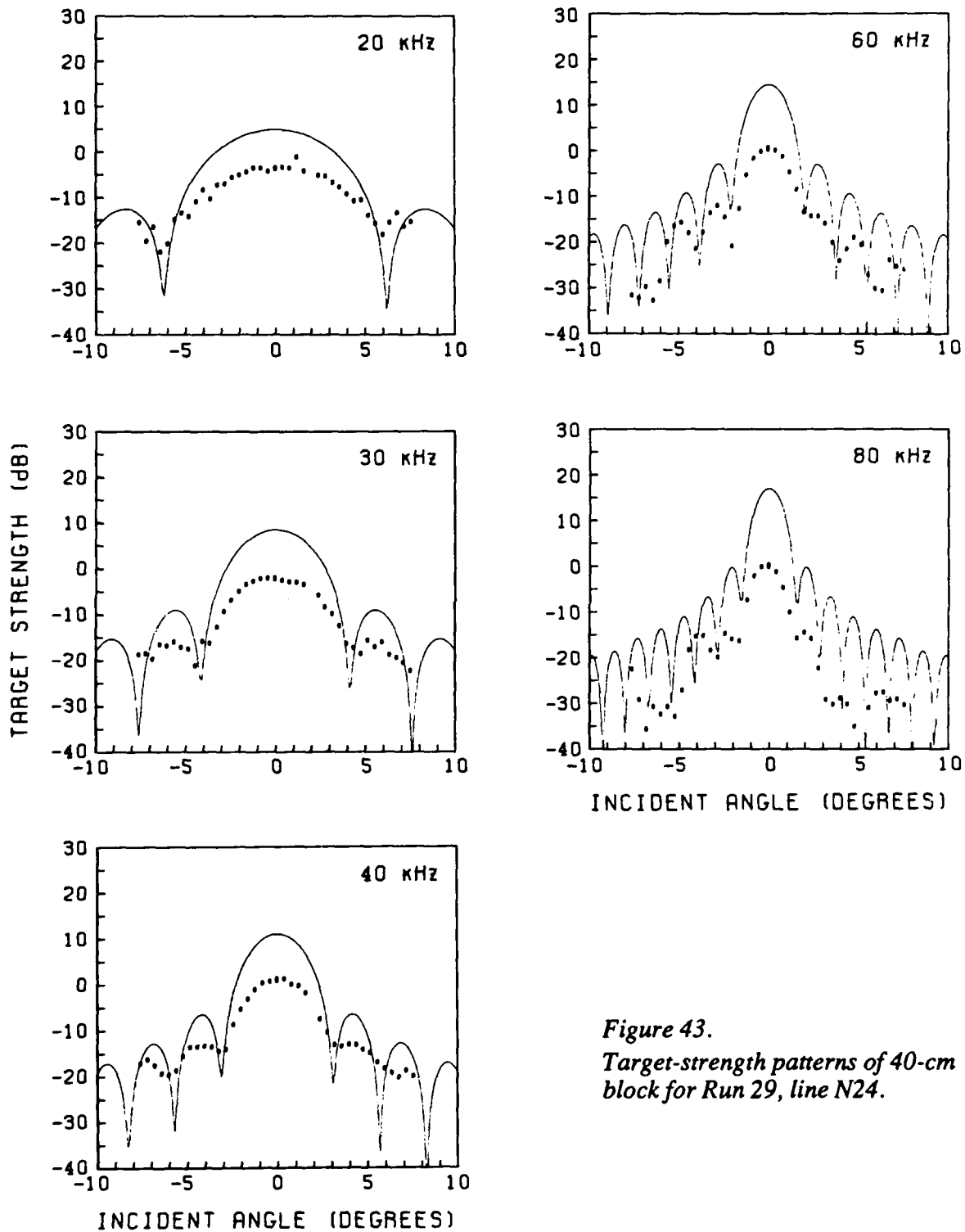


Figure 43.

Target-strength patterns of 40-cm block for Run 29, line N24.

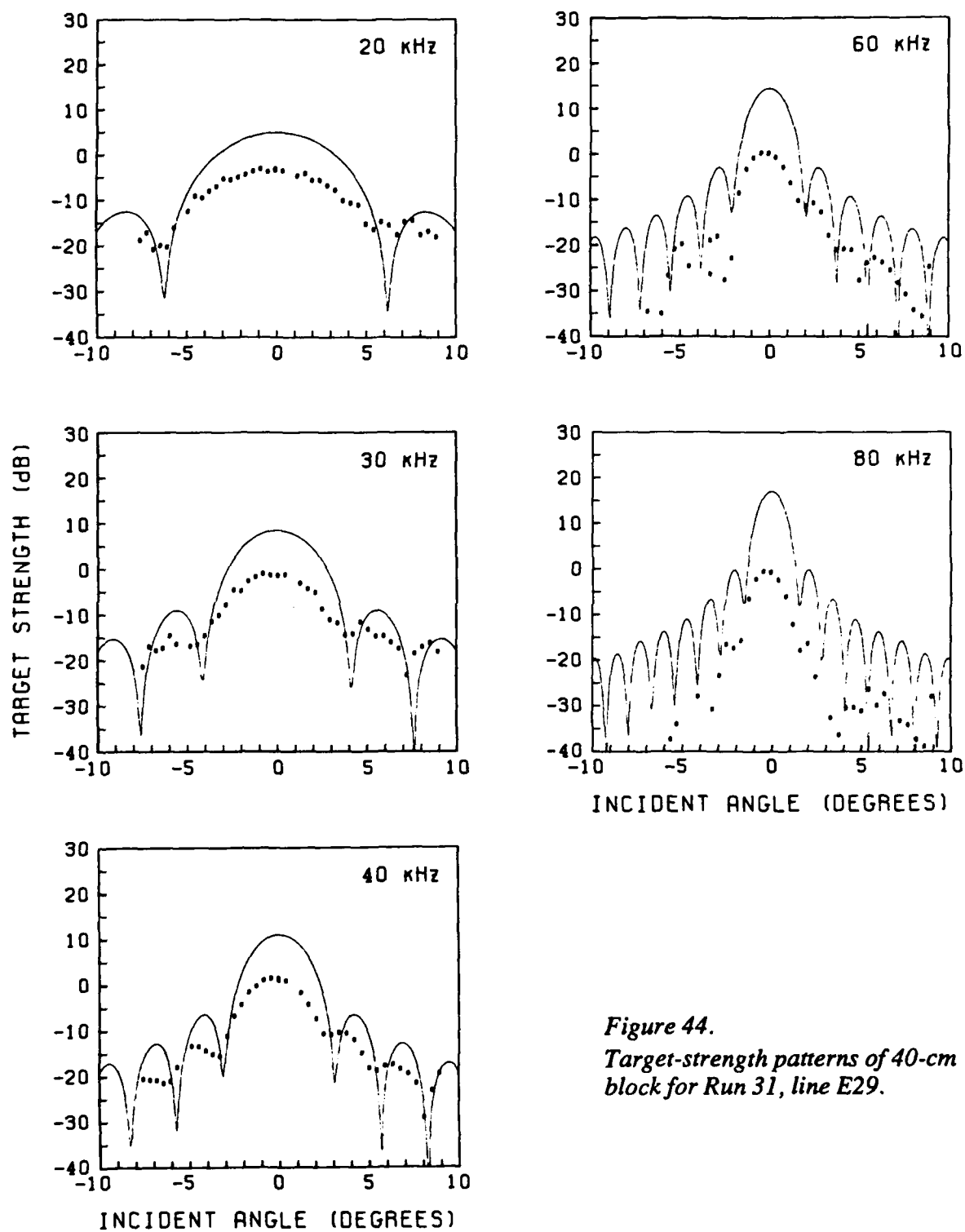


Figure 44.
Target-strength patterns of 40-cm
block for Run 31, line E29.

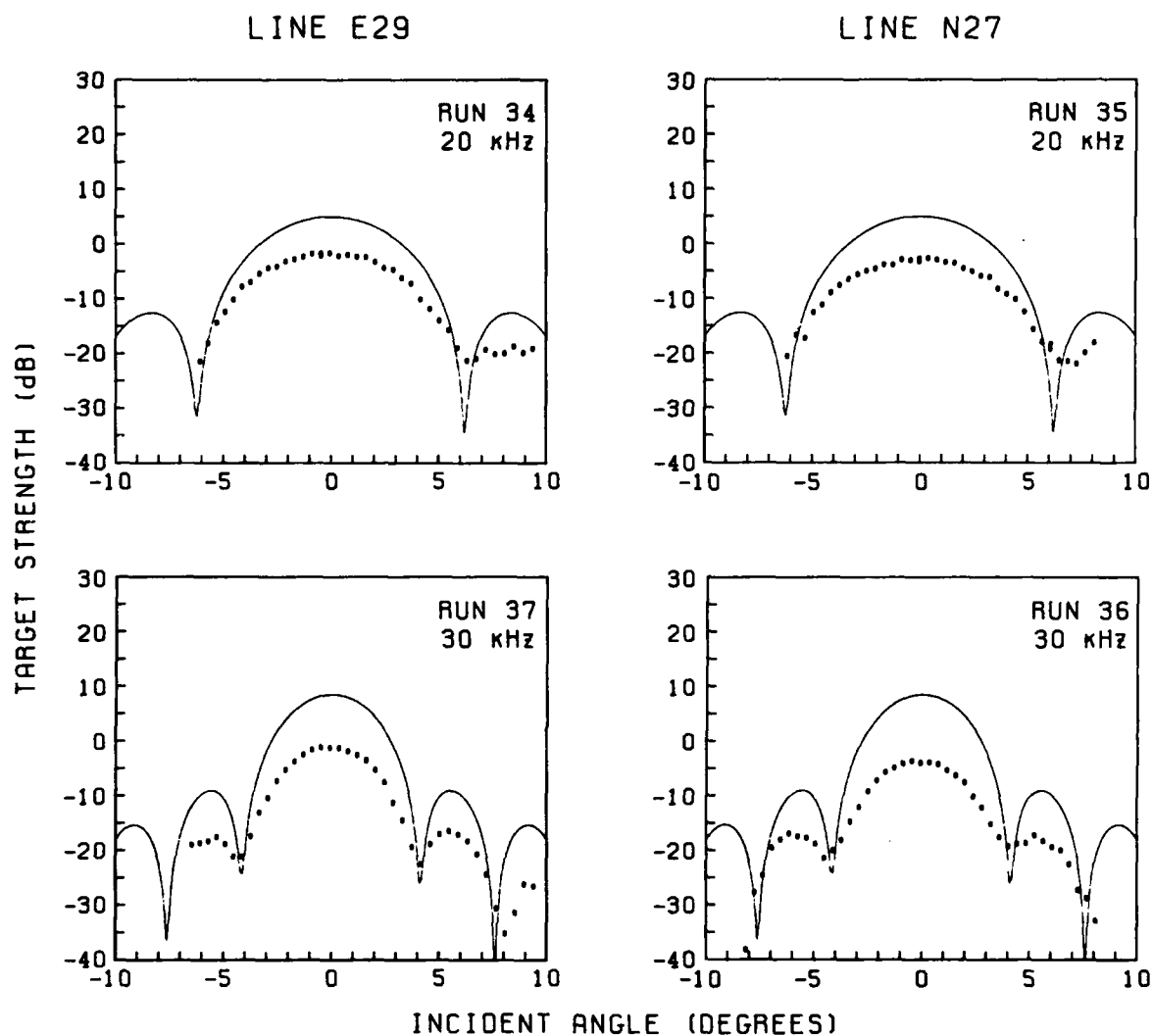


Figure 45. Target-strength patterns of 40-cm block for Runs 34–37, lines E29 and N27.

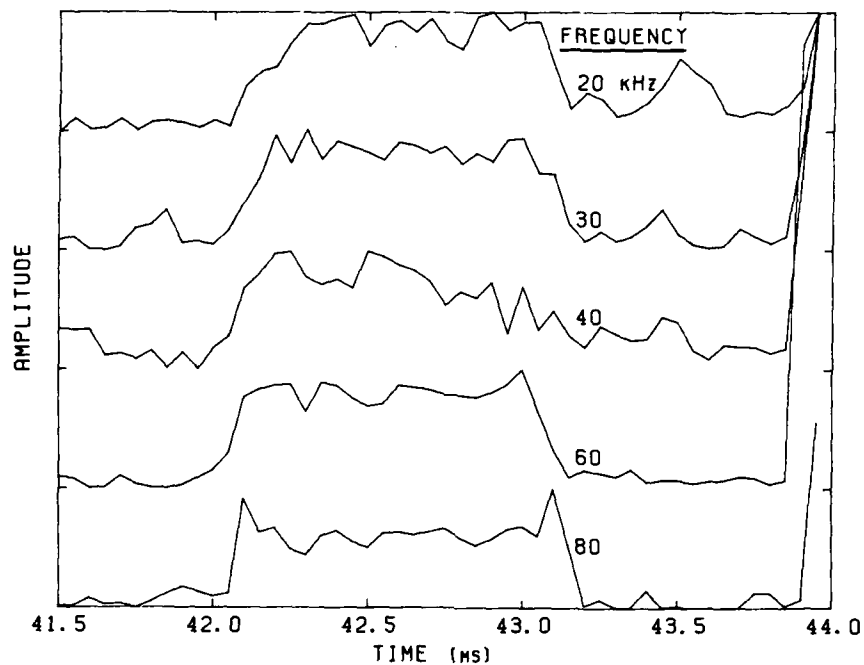


Figure 46. Returns from the 109-cm block, using the ITC transducer.

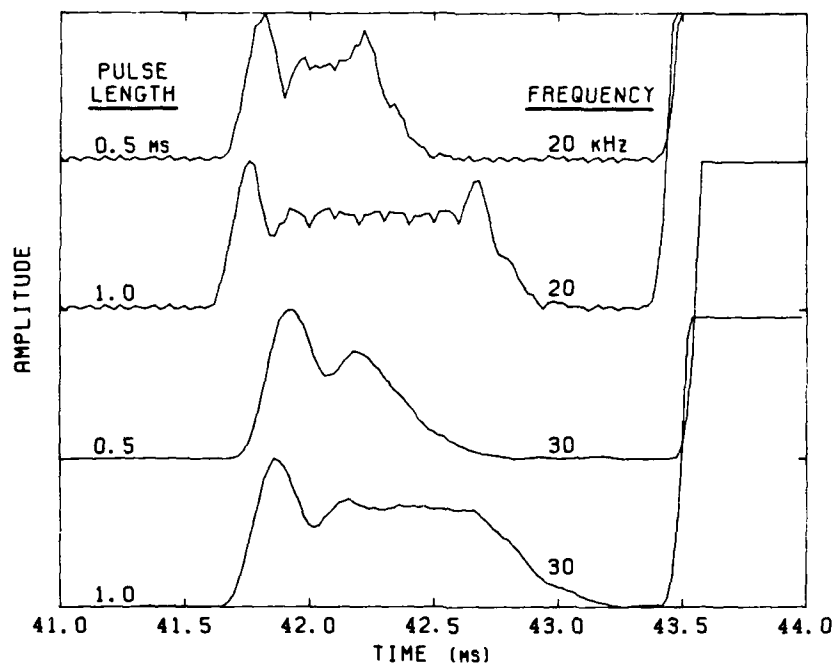


Figure 47. Returns from the 109-cm block for two frequencies and two pulse lengths, using the hemispherical transducer.

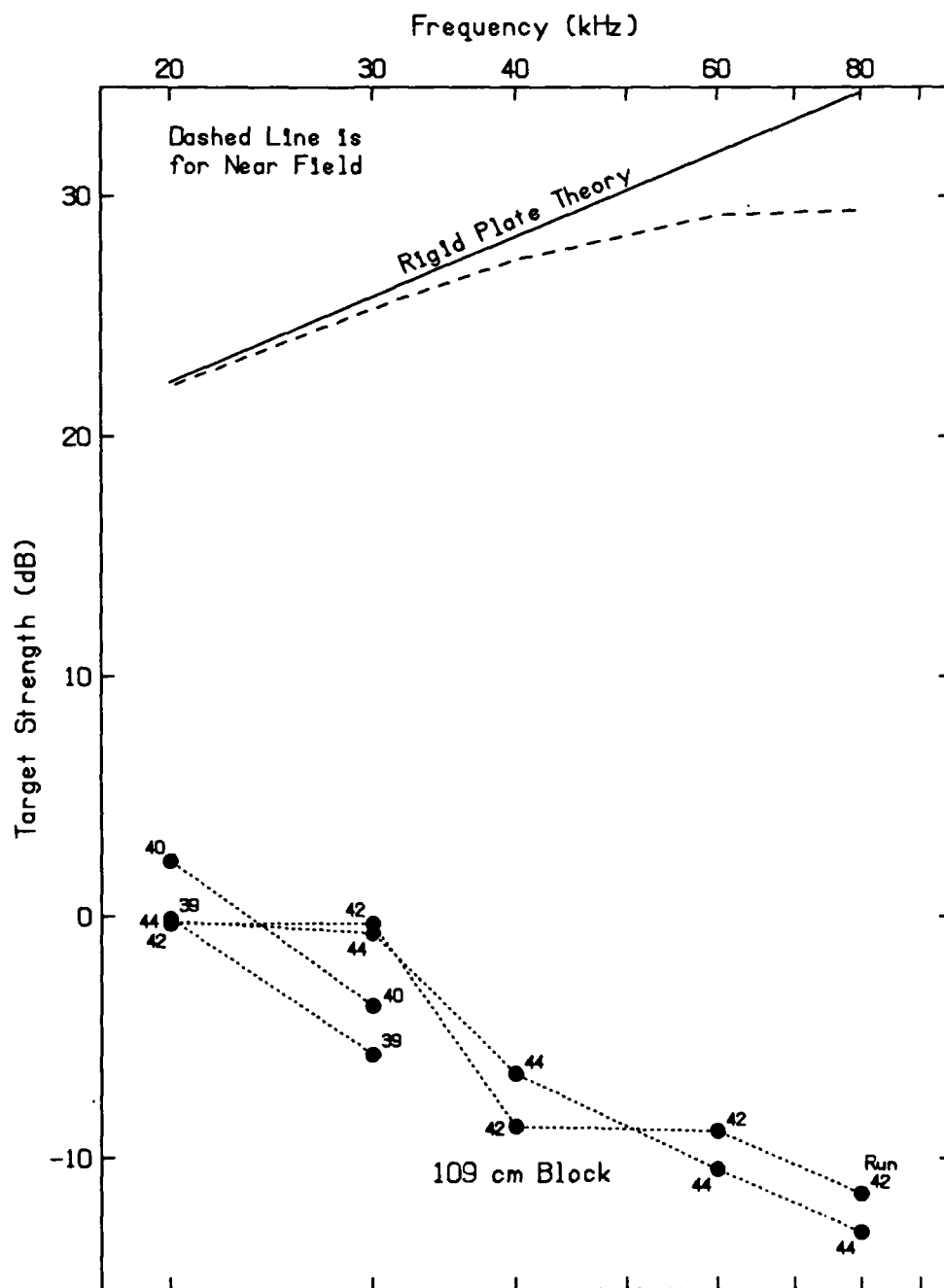


Figure 48. Target strengths of 109-cm block at normal incidence.

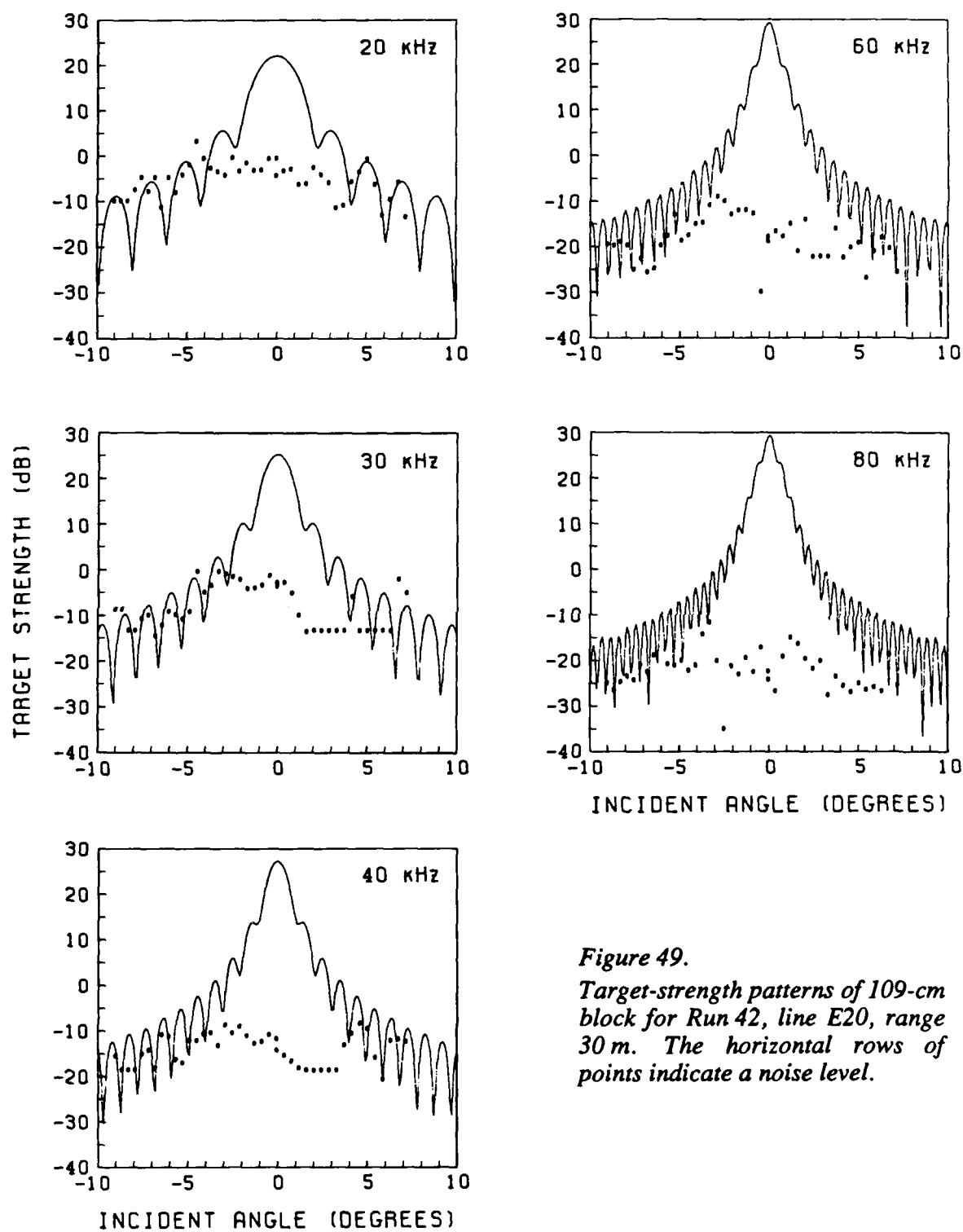


Figure 49.

Target-strength patterns of 109-cm block for Run 42, line E20, range 30 m. The horizontal rows of points indicate a noise level.

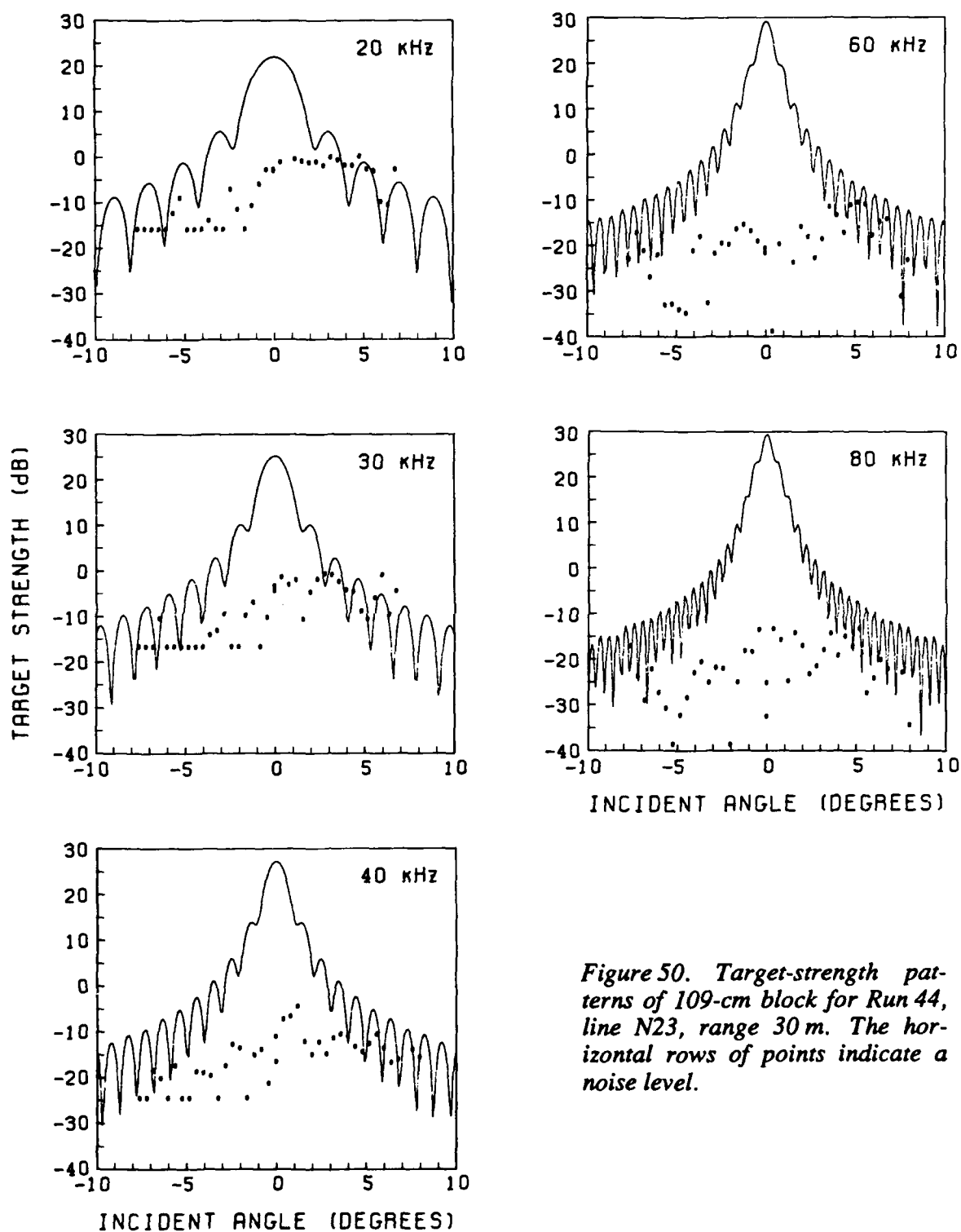


Figure 50. Target-strength patterns of 109-cm block for Run 44, line N23, range 30 m. The horizontal rows of points indicate a noise level.

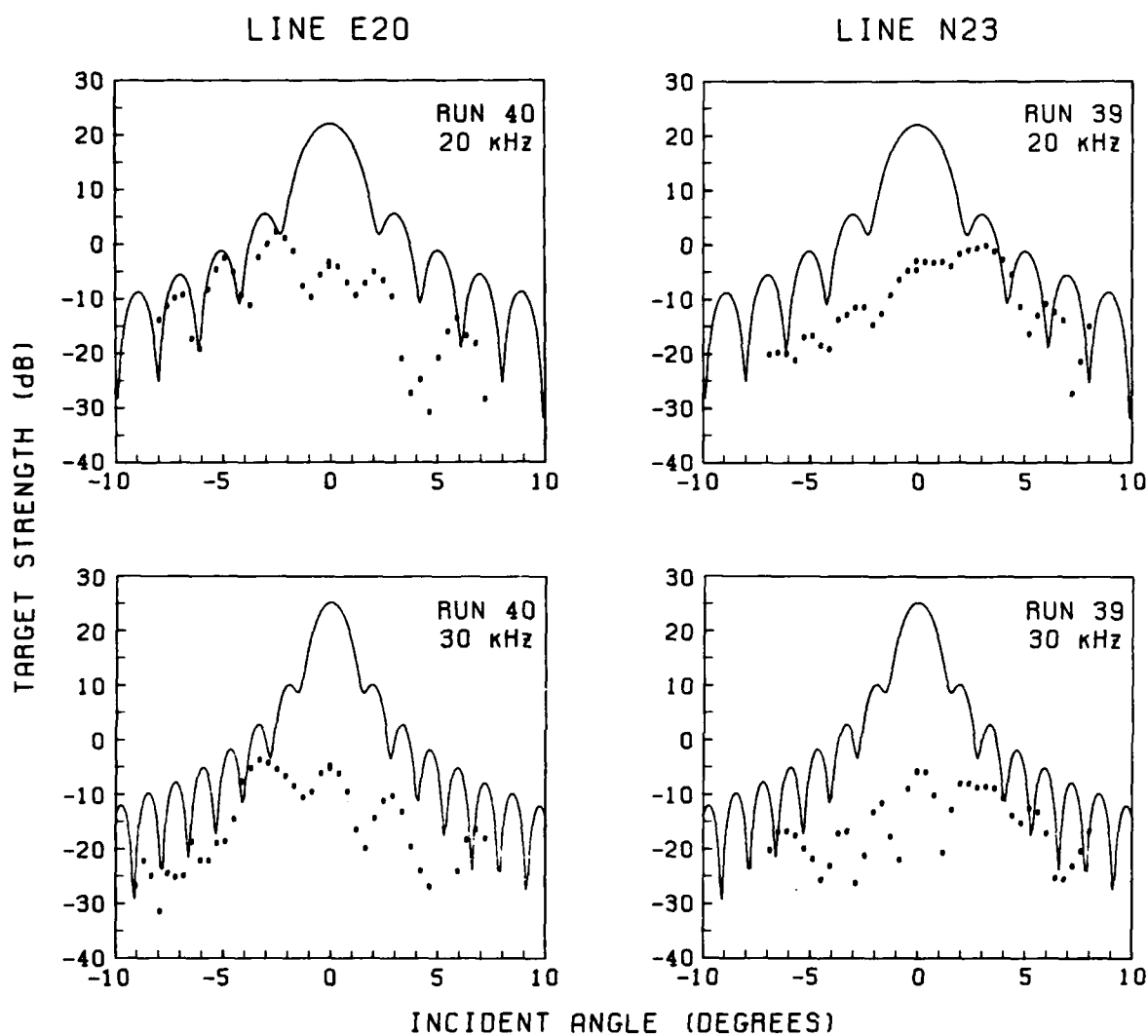


Figure 51. Target-strength patterns of 109-cm block for Runs 39 and 40, range 30 m.

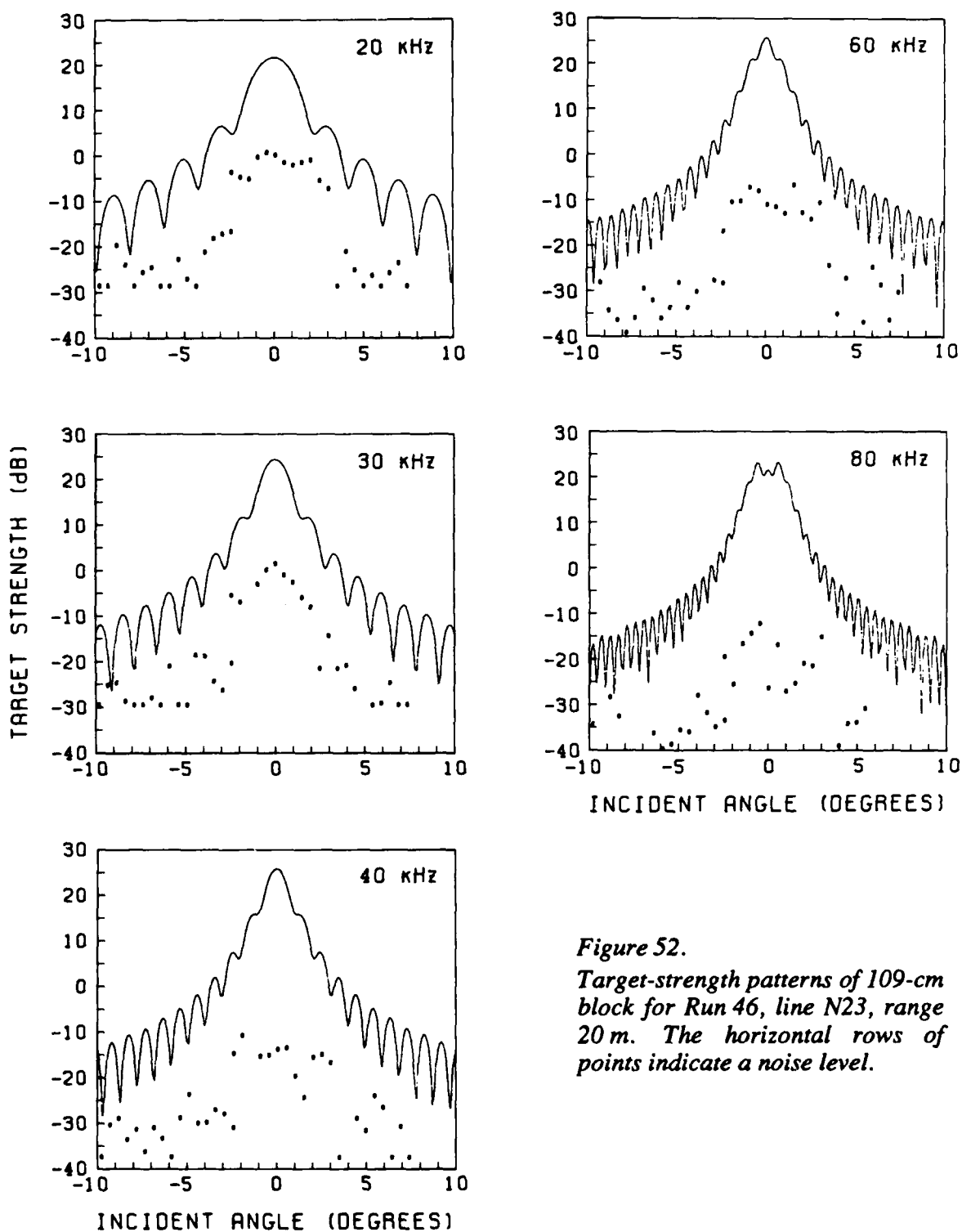


Figure 52.

Target-strength patterns of 109-cm block for Run 46, line N23, range 20 m. The horizontal rows of points indicate a noise level.

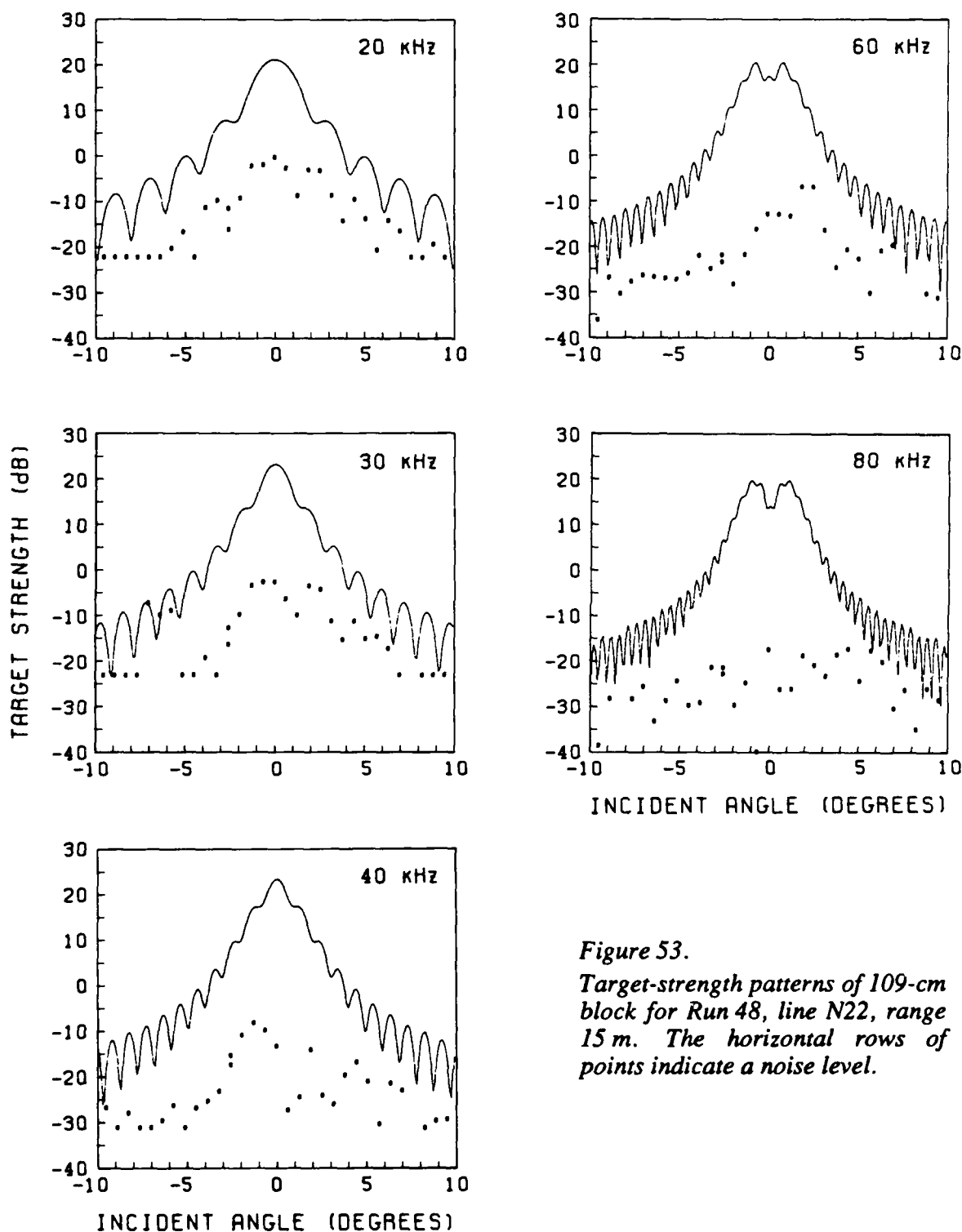


Figure 53.

Target-strength patterns of 109-cm block for Run 48, line N22, range 15 m. The horizontal rows of points indicate a noise level.

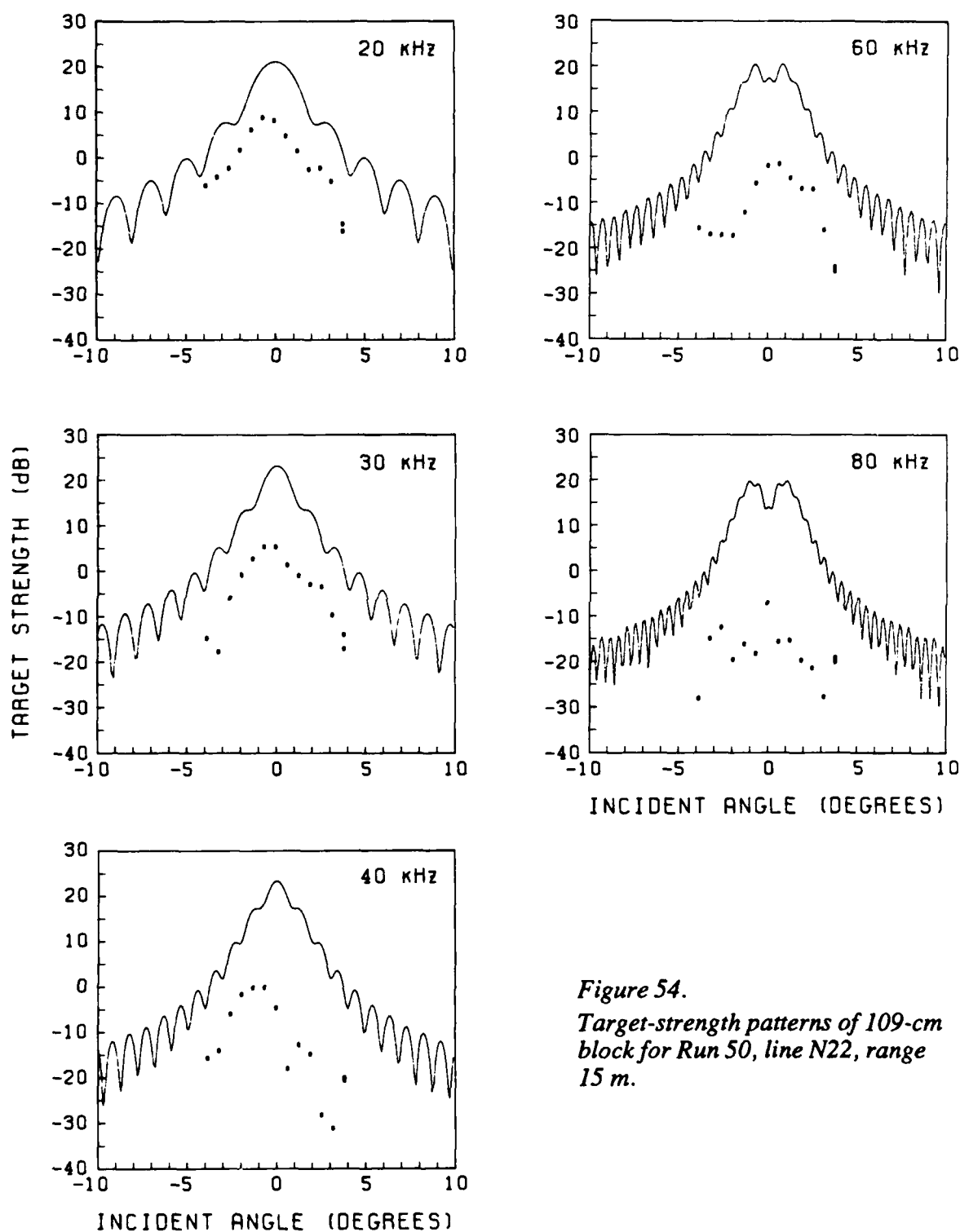


Figure 54.
Target-strength patterns of 109-cm
block for Run 50, line N22, range
15 m.

60 APL-UW 8707

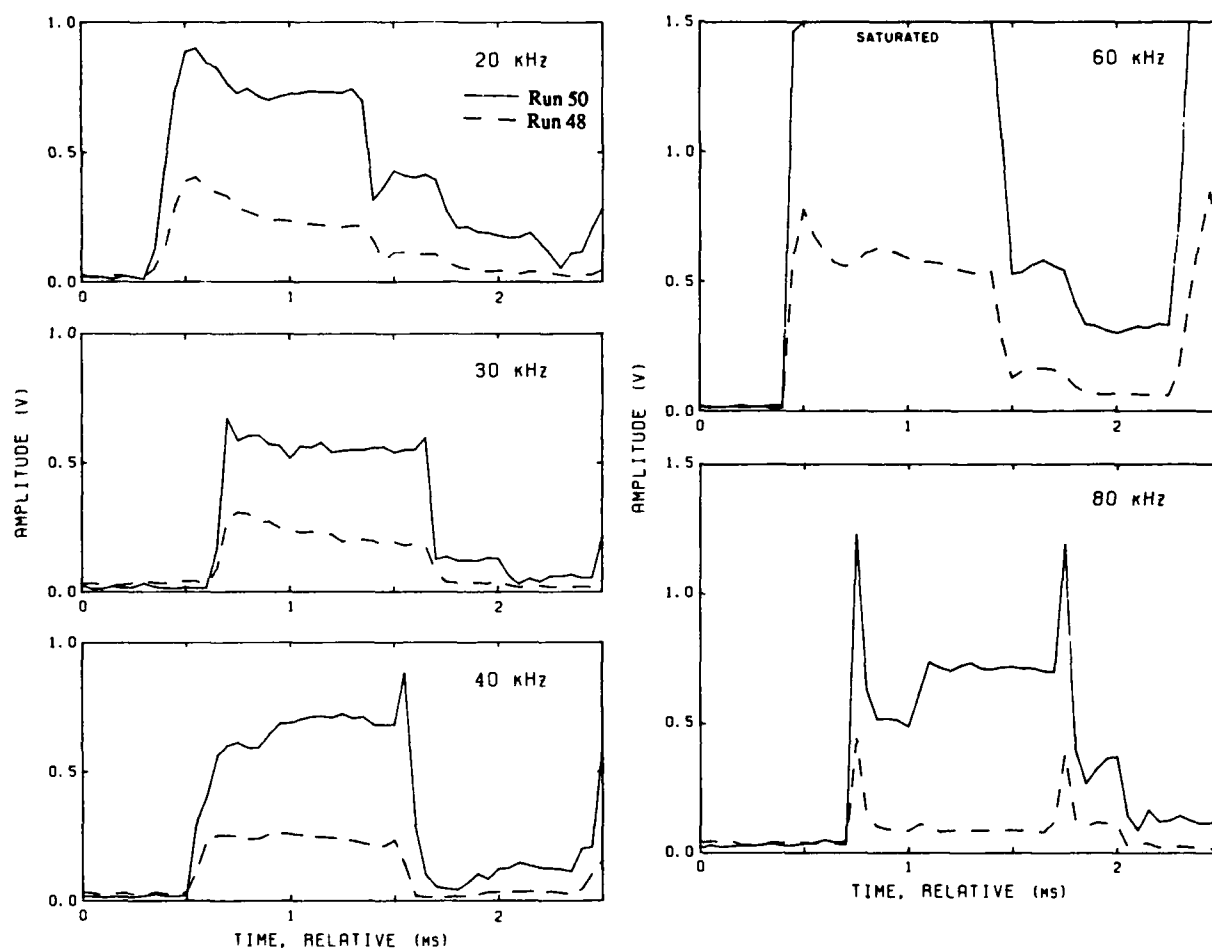


Figure 56. A comparison of the returns for Runs 48 and 50, 109-cm block.

VIII. LOWER FACE REFLECTIONS

The reflections from the underside of the blocks cut from the arctic ice cover were used to study the variation in reflection with the diameter of the blocks and with the acoustic frequency. The shape of the lower boundary of the ice and the porous structure of the skeletal layer were examined as possible causes of the low reflectivity of the undersurface.

A. Area Dependence

For comparison, the target strengths of the different sized blocks have been plotted together in Figure 57. The next figures are for two different corrections for the area of the block face, since the area dependence may indicate the type of reflection taking place.

- (1) Reflection proportional to area A . This area dependence would correspond to incoherent scattering from a very rough surface. Figure 58 shows that the normal-incidence returns for the 84- and 109-cm blocks are in fair agreement when the $10 \log A$ correction is applied, indicating an incoherent scattering. For this type of reflection, the central peak would generally be small, and there would be no side lobes. However, if the rms slope was small, a peak would be present even though the return was incoherent. Figures 49–51 show that the 109-cm block gave low peaks and no side lobes, indicating incoherent scattering. The short-block return gave a normal-incidence target strength so much higher than the larger blocks that a different type of reflection must have occurred.
- (2) Reflection proportional to area squared. This corresponds to the reflection from a rigid plate (or pressure relief surface). Figure 59 combines results for different sized blocks using a correction of $20 \log A$. The 84- and 109-cm results are further apart than for the $10 \log A$ correction, indicating a lack of

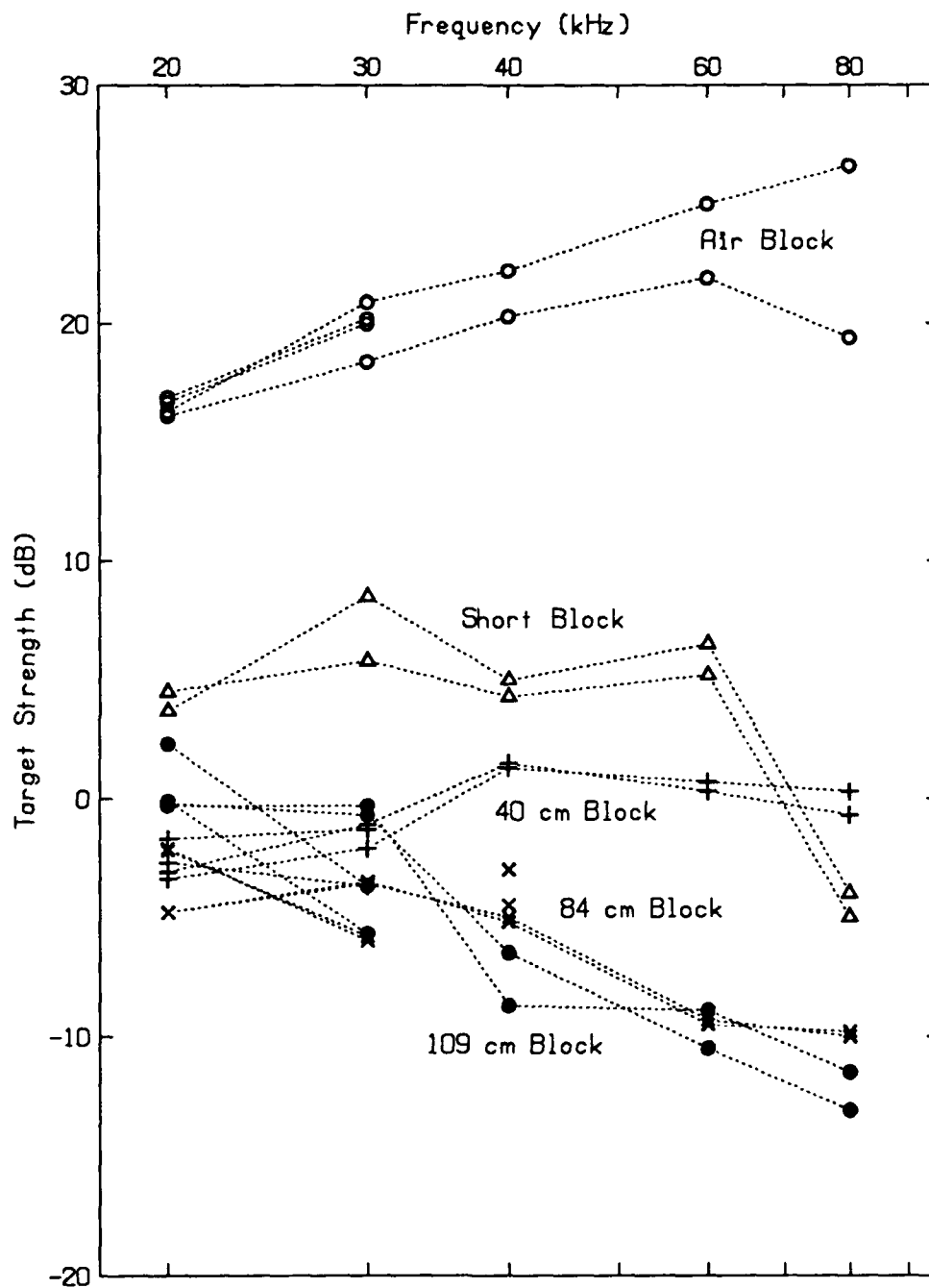


Figure 57. The measured target strengths at normal incidence for all blocks (no area correction).

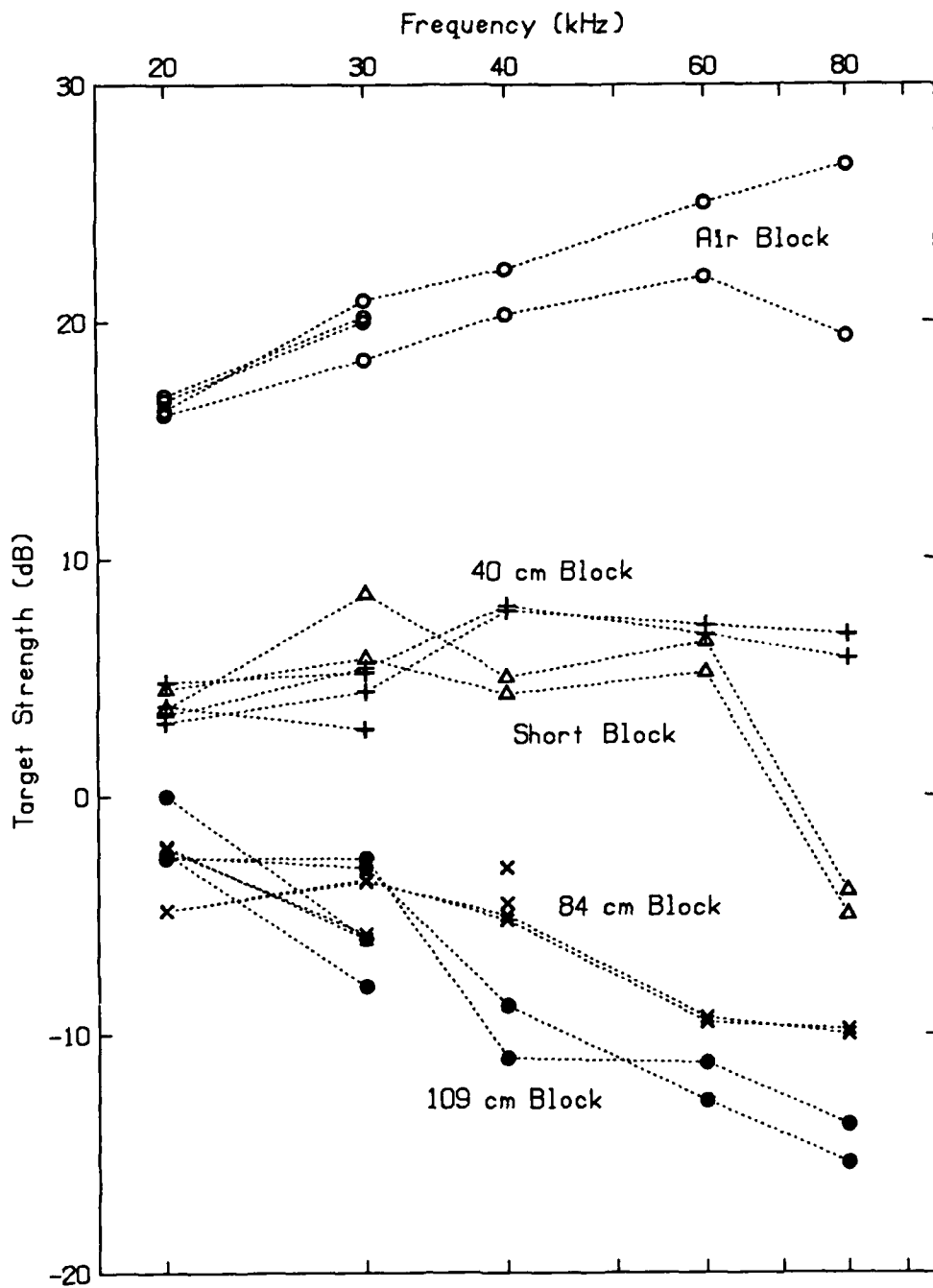


Figure 58. Target-strength measurements with an area correction of $10 \log A$. The 40-cm and 109-cm results are corrected to a diameter of 84 cm.

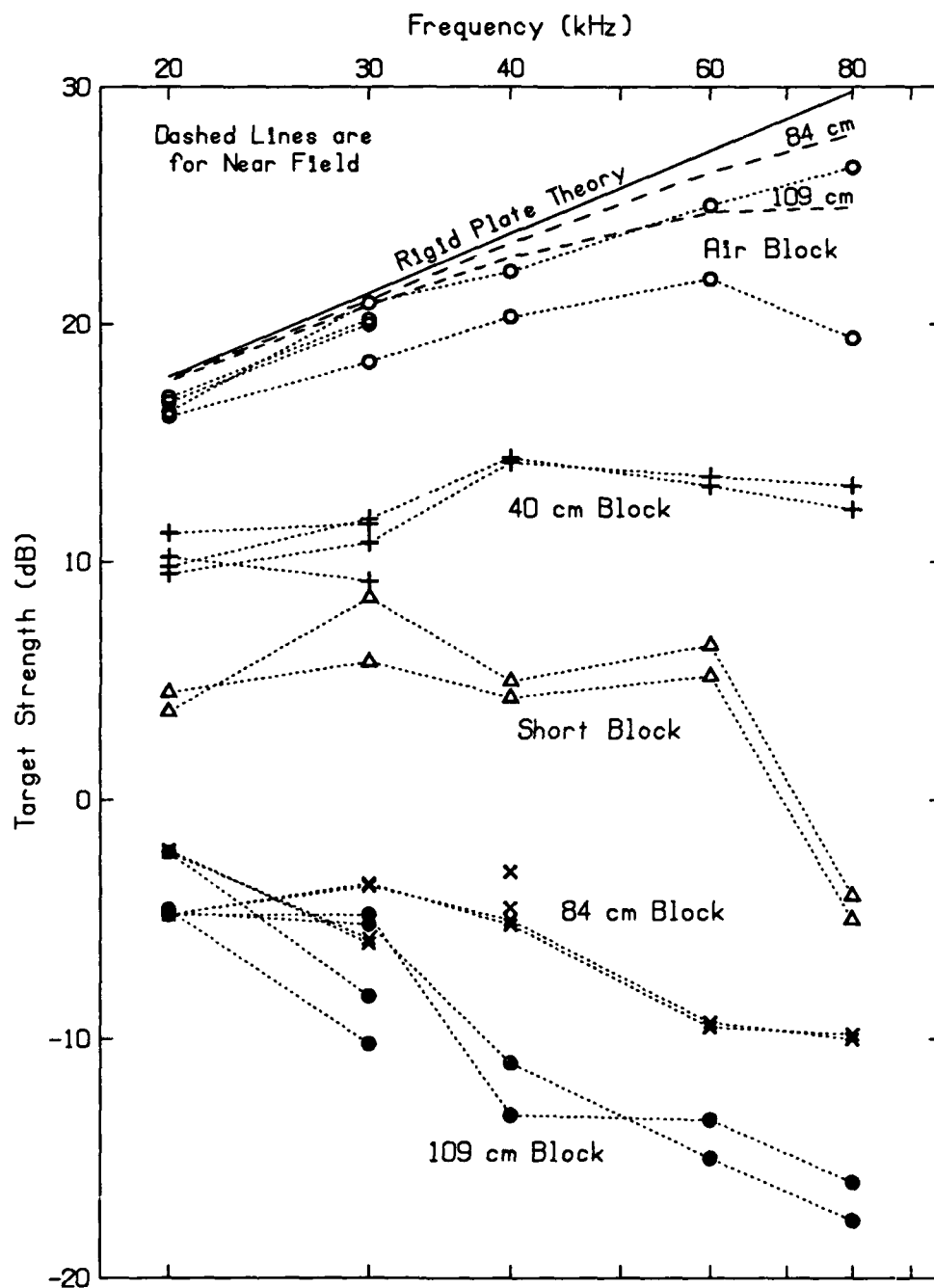


Figure 59. Target-strength measurements with an area correction of $20 \log A$. The 40-cm and 109-cm results are corrected to a diameter of 84 cm.

coherency. The results for the 40-cm block are here about 10 dB below rigid-plate theory—approximately the amount that would be expected if the surface was smooth and the loss was all from the impedance mismatch between water and ice.³

Neither of the two area corrections brings the target strengths into good agreement; however, for the larger blocks, the $10 \log A$ correction is better. Although all blocks were cut from the same flat area, there seems to be a difference in the reflectivity. The larger blocks gave incoherent returns, whereas the 40-cm block gave the high peak at normal incidence and the sidelobe pattern corresponding to a coherent return. We believe that the 40-cm face was not typical and look for some cause of an increased reflectivity to explain the high return (see next paragraph).

B. The High Return from 40-cm Block

Differences in the surface resulting from the preparation of the blocks or from other causes must be considered when looking for reasons for the unusually high return from the 40-cm block. One possibility is that fresh water was released below the ice when the diver hole, the 84-cm block, or the 40-cm block was melted out. This water might have formed a glaze of ice over the surface of the 40-cm block. However, this would require the ice to absorb a considerable amount of heat quickly before the fresh water was carried away by the current.

A second, and more likely, possibility is that air exhaled by the divers or the overflow from the air block collected in a slight cavity at the position of the 40-cm block and entered the skeletal layer. (Disappearance of air into the underside of the ice was observed in March 1987.) Such air would increase the reflection and, if uniform enough, would give a response pattern like that of a pressure-relief surface. This air would not have been observable when the end of the block was casually examined after it was removed and laid on its side. Because the response pattern was similar to that of a rigid

plate, we conclude that this is the most probable explanation for the high returns from the 40-cm block.

C. Effect of Skeletal Layer

To determine the effect of the skeletal layer on acoustic reflection, measurements were made of the reflections from the short block (Section VII.A) formed by sawing off the lower 30 cm. Except at the higher frequencies, where the saw cut variations were greater than a quarter wavelength, the amplitude of the returns at normal incidence agreed well with the predictions of rigid-plate theory plus the loss due to impedance mismatch at the water-ice interface. The response patterns showed the central peak and side lobes, at least in one direction (Figures 31 and 32). Therefore, it must have been some characteristic of the skeletal layer that caused the low returns from the natural block surfaces.

Examination of the ice with probes indicated that the skeletal layer, which we consider as the transition to hard ice, occupied 10–15 cm. The backscatter of acoustic energy must involve some penetration into the soft skeletal layer of the ice. However, the short rise time of the returns shows that only 2 or 3 cm of this layer could have been involved in the reflections.

A roughness produced by a layer of reflectors about 1 cm thick would cause little interference at 20 kHz and greater interference at higher frequencies, as observed. However, a layer of uniformly dispersed reflectors as thick as the observed skeletal layer, 10–15 cm, would produce interference at all frequencies, which is not in agreement with the measurement. Therefore, if the low returns are due to interference from reflections within the skeletal layer, no more than 1 or 2 cm of the layer is involved. Another factor is that high acoustic absorption in the skeletal layer, as has been deduced from our measurements, may limit the effective thickness of the layer involved in the backscattering process.

D. Effect of Large-Scale Surface Features

It is also possible that the underside of the ice cover was not flat. Undulations in the under-ice surface have been observed in other years; they are thought to be related to drifts of snow on the upper surface which change the insulation and thus the thickness of the ice. In general, if large-scale variations are present, the larger the block the greater the variation from a flat surface and the lower the return as a result of interference. This might explain the decrease in target strength as the block diameter increases. Some models of reflection from surfaces with different shapes are presented in Appendix A.

E. Frequency Dependence

All measurements show a decrease in target strength at the higher frequencies. This would occur if the variations in the undersurface approached peak-to-trough dimensions equal to a quarter wavelength, which results in destructive interference. The same would be true for volume scatterers spaced a quarter wavelength apart vertically. For the measurements reported here, quarter wavelengths vary from 1.79 cm at 20 kHz to 0.45 cm at 80 kHz. Even with surface variations within this range, the face might appear "flat" to the eye.

The effect of a gradual transition of sound speed in the skeletal layer, as discussed in Appendix B, is also highly frequency dependent.

F. Equivalent Reflection Coefficients

The amplitude reflection coefficient is unity if the measured target strength is the same as that from a pressure relief surface or a rigid plate. For target strengths differing from this by ΔTS , the corresponding amplitude reflection coefficient, R_A , is related by

$$\Delta TS = 20 \log R_A . \quad (1)$$

Values of R_A for an 84-cm block are plotted in Figure 60, which is at the same scale as

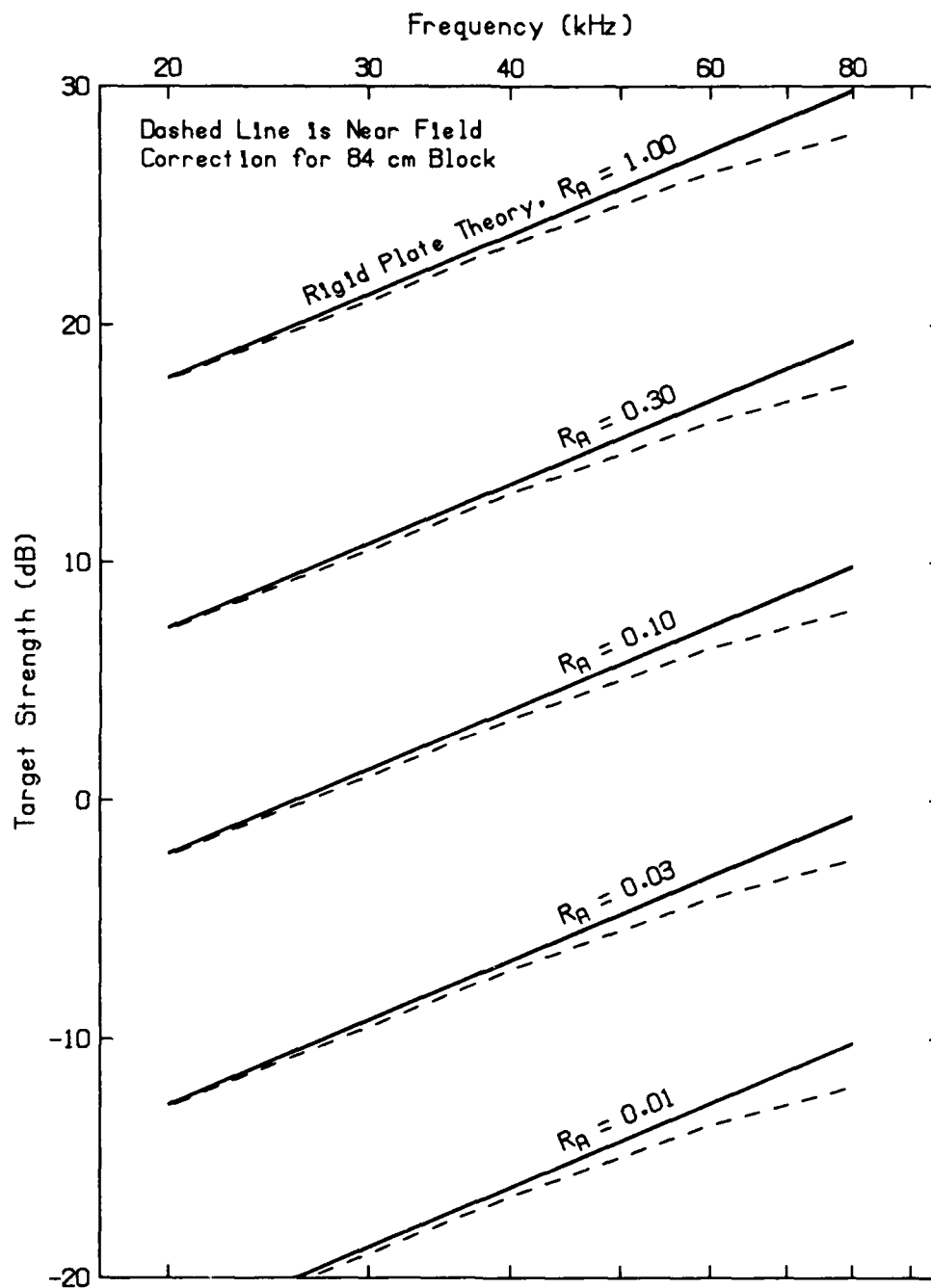


Figure 60. Amplitude reflection coefficients, R_A , corresponding to target strength for an 84-cm diameter block. The reflection coefficients corresponding to the target-strength values on Figure 59 can be obtained by comparison of the two figures.

Figure 59 for ease of comparison. This combination of rigid plate theory with plane wave reflection coefficient is allowed by the Kirchhoff approximation.⁸

G. Comparison with the 1984 Experiment

The results described here for the spring 1986 measurements on the 84-cm block can be compared with those given earlier³ for the same size block in fall 1984. The comparison, for normal incidence, is shown in Figure 61. There is rough agreement, with the most pronounced difference occurring at 20 kHz. The higher return and better pattern in 1984 indicate that the block face may have been flatter. Another possibility is that the difference in environmental conditions such as the ice thickness, the growth rate, and the temperature gradient in the ice may have produced differences in the ice surface.

In the earlier report,³ we approximated the response pattern throughout the peak and sidelobe region with a straight line,

$$TS = A - B \theta, \quad (2)$$

and found that a value for B of 2.6 dB per degree roughly fits the slope for all frequencies. The same analysis for the 40-cm and 84-cm blocks in 1986 gives the values of B shown in Figure 62, which have an average of 2.88 ± 0.4 dB per degree. For modeling purposes, $B = 3$ dB per degree would be a fair representation at all frequencies (20–80 kHz). Values for the constant A can be determined from Figure 59, taking into consideration the discussions in this report.

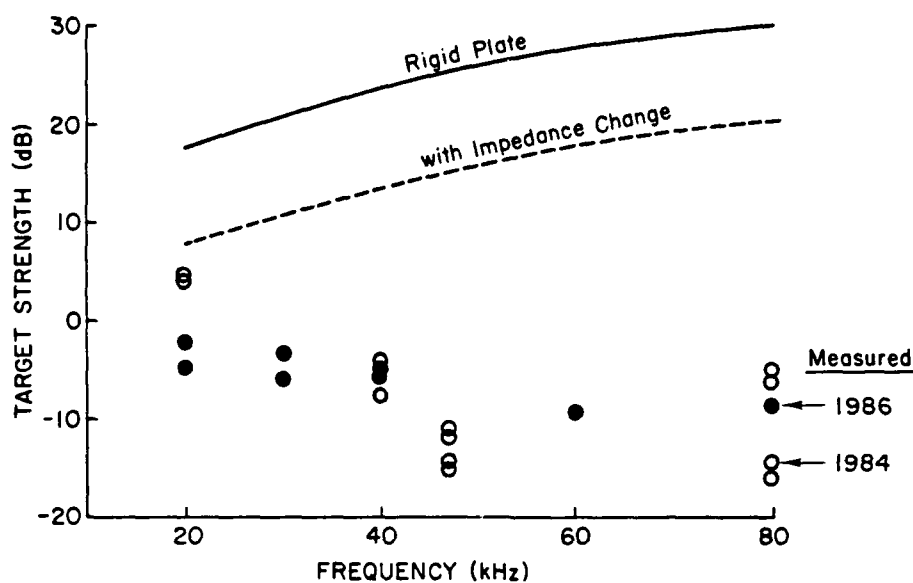


Figure 61. Comparison of 1984 and 1986 results for the 84-cm block at normal incidence.

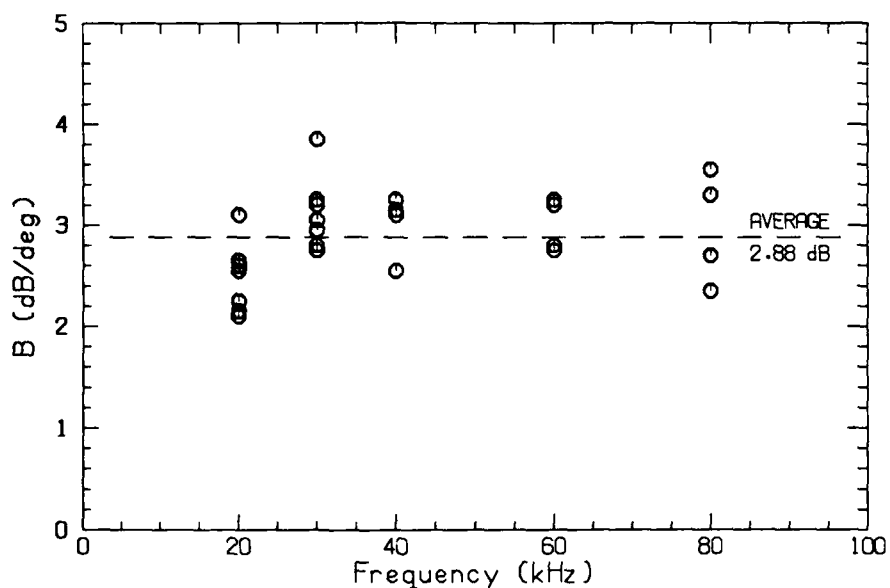


Figure 62. The constant B in Eq. 2 as determined from the 1986 measurements on an 84-cm diameter block.

IX. UPPER FACE REFLECTIONS

In some of the measurements, the return from the back, or upper, face was distinguishable. For the short block, which was cut off at both ends and thus had the same water-ice interface at each end, rough values of the absorption coefficient in the ice can be computed from the two returns. For the other blocks, the absorption coefficient can be determined only if the reflection coefficient for the upper face is known. This face, which was originally the surface of the floe, was covered with a hard crystalline layer of snow. When the blocks were submerged into water at its freezing point (-1.6°C), some water should have frozen onto this face, possibly trapping air in the snow interstices. Regrettably, no examination was made of the upper surface to verify such freezing when the block was removed.

A. Absorption Calculated from Short-Block Measurements

Based on the length of the short block (48.3 cm) and an assumed sound speed of 3300 m s^{-1} , the time delay between the first and second returns would be 0.28 ms. The pulse length used was 1 ms, and therefore considerable overlap would be expected. An example of the returns is shown in Figure 63. The returns were found to change amplitude near 0.28 and 1.28 ms and thus consisted of three levels: the return from the lower face, the sum of the two, and the return from the upper face. It was often difficult to read the third level because it was so low. The three levels were the most readable at 30 kHz.

For this analysis we treat the sound as a plane wave striking an infinite surface. At the lower face, with amplitude reflection coefficient R_A , the transmitted sound has an amplitude $(1 + R_A)$ times the incident amplitude. Upon reflection from the upper face, the amplitude changes by a factor of R_B , which is negative in this instance. Passing through the lower face, it changes by a factor of $(1 - R_A)$. Absorption occurs both ways. The relationship between the measured amplitudes is given by

$$20 \log(A_3/A_1) = 20 \log(1 + R_A) + 20 \log(1 - R_A) + 20 \log(-R_B) - 20 \log R_A - 2\alpha t, (3)$$

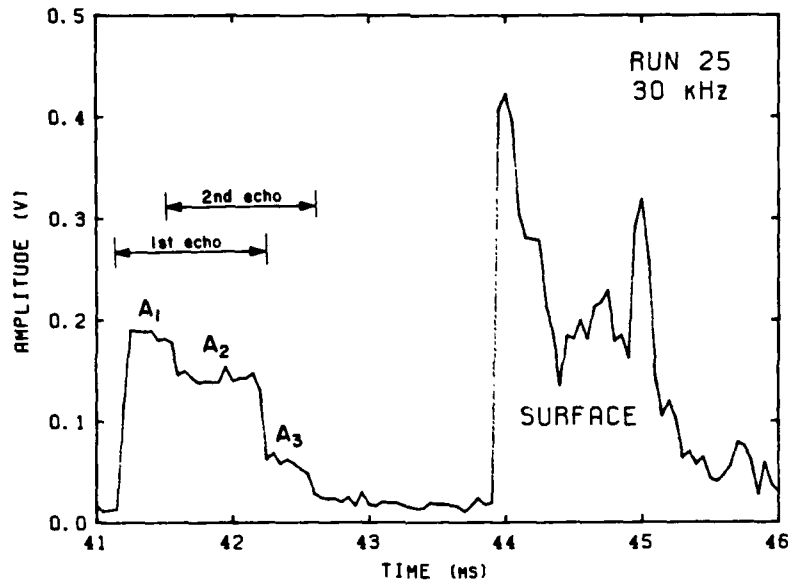


Figure 63. Lower and upper face reflections for the short block. Amplitude A_2 is the combination of the lower face reflection, A_1 , and the upper face reflection, A_3 .

where A represents the first face, B represents the second, and t is the thickness. A_1 , A_2 , and A_3 are the amplitudes, in order, of the three levels in the return. From this we obtain

$$\alpha = \left[\frac{1}{2t} \right] 20 \log \left[\frac{(1-R_A^2) A_1 (-R_B)}{A_3 R_A} \right] \quad (4)$$

for the absorption coefficient in the ice. This assumes that spreading within the ice is negligible and that both returns suffer the same spreading loss between the ice and the receiving transducer. For the short block, we assume that $R_B = -R_A$ and that α is constant throughout the block. R_A can be determined from the lower-face reflection data.

In addition, the phase relation between the two returns can be calculated by computing the phase difference between A_1 and A_3 that would give the resultant A_2 . The calculated phase, using the cosine law, is

$$P = \cos^{-1} \left[\frac{A_2^2 - A_1^2 - A_3^2}{2A_1 A_3} \right]. \quad (5)$$

The returns observed from the upper face of the short block during the experiment can be used, through Eq. 4, to measure α . Some of the short-block returns examined in this regard are shown in Figure 64. The third level was often low and may have been influenced by the tail of the transmitted pulse or some extraneous reflection. Some air-block returns are shown in Figure 65 so that the third level in the short-block returns can be compared with the falloff of the air-block return. At 20 kHz, the third level was about the same amplitude as the falloff; thus the readings are questionable. The best three-level returns were observed at 30 kHz. No returns were readable at 40 kHz (not shown), while at 60 and 80 kHz there were several.

For each return with three levels, we calculated α with the results shown in Figure 66. McCammon and McDaniel⁹ used Langleben's results to predict α at -6°C and the ice internal friction data of Kurowia to develop a temperature dependence for α . The dependence is given by

$$\alpha = 0.06 f \left(\frac{-6}{T} \right)^{2/3} \text{ dB m}^{-1}, \quad (6)$$

where T is the temperature in degrees Celsius and f is the frequency in kilohertz. This relationship is plotted for $T = -2^\circ\text{C}$ in Figure 66. The ice block temperature must have been lower than -2°C because the block had been in the air for 3 days at below -20°C and then in the water for only an hour or two. A lower temperature would lower the absorption curve, thus increasing the discrepancy shown in the figure.

Another consideration is that our measurements were for vertical transmissions whereas Eq. 6 is for horizontal transmissions. If scattering were the dominant process, we would expect the absorption to be less for vertical transmissions than for horizontal ones, because the brine pore inclusions are elliptical in shape and their major axis is vertical. The opposite of this is observed, probably because of other factors.

Two approximations were made in these absorption calculations: (1) use of plane wave reflection coefficients for transmissions through the block, and (2) disregard of spreading within the block.

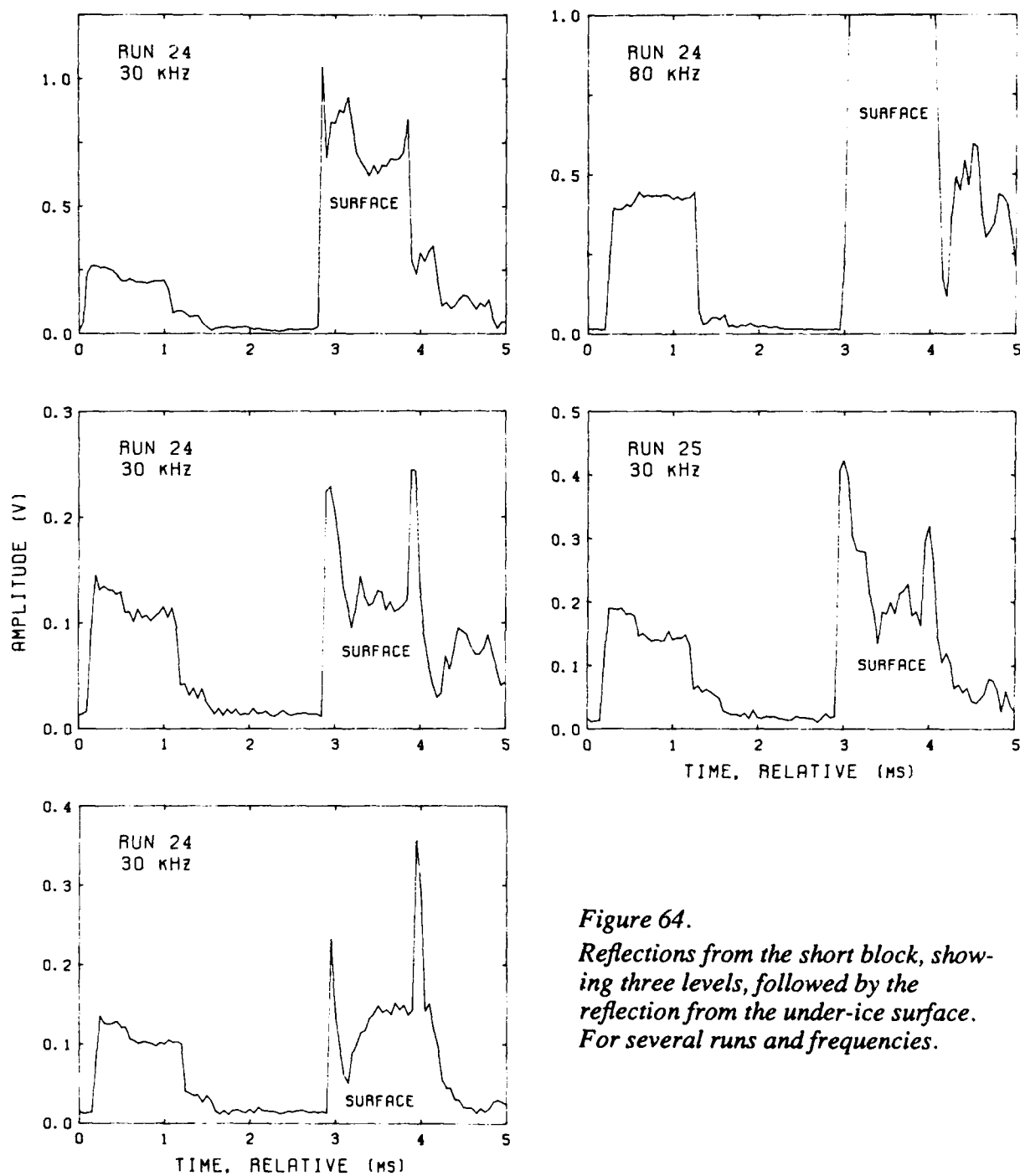
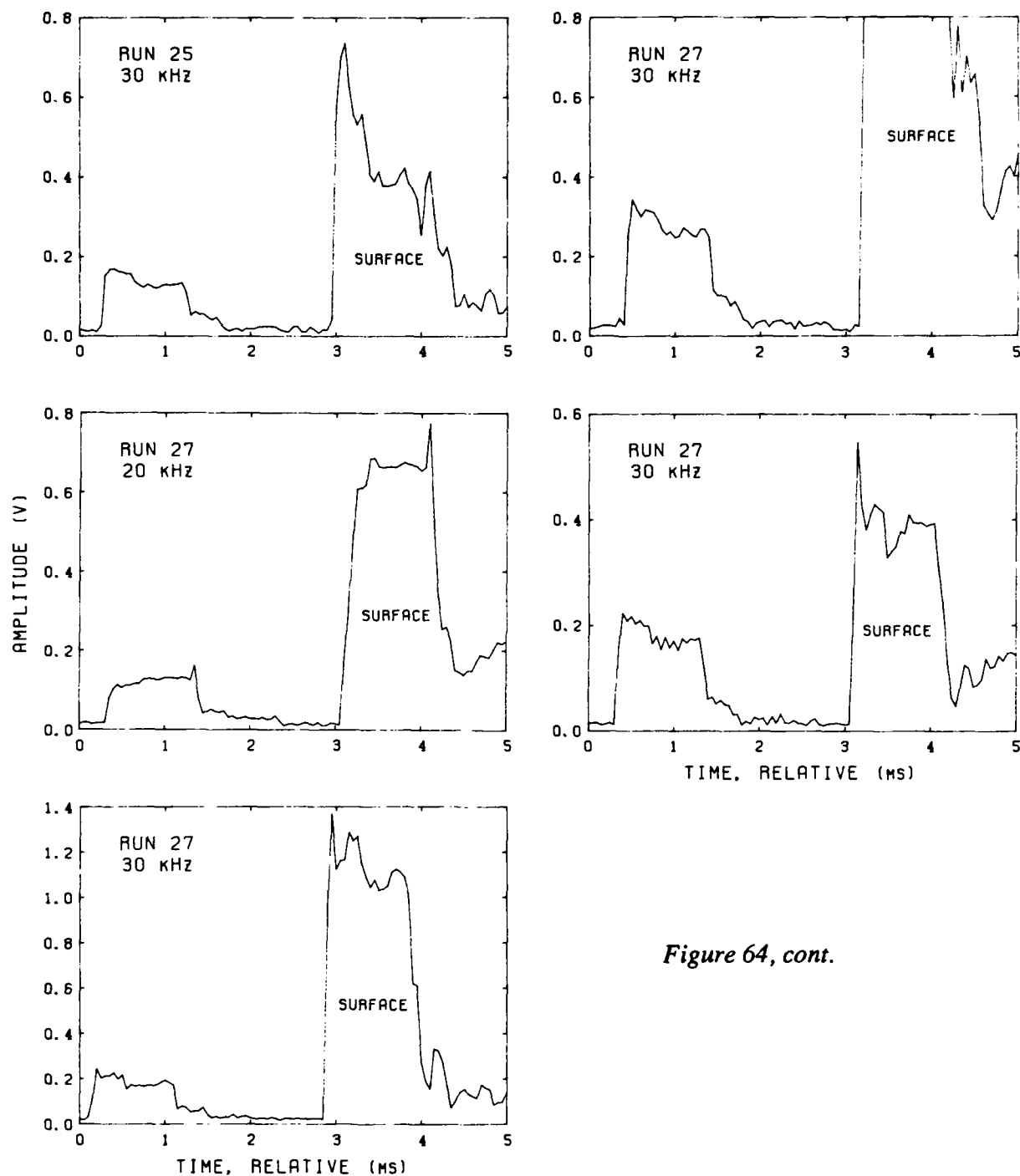
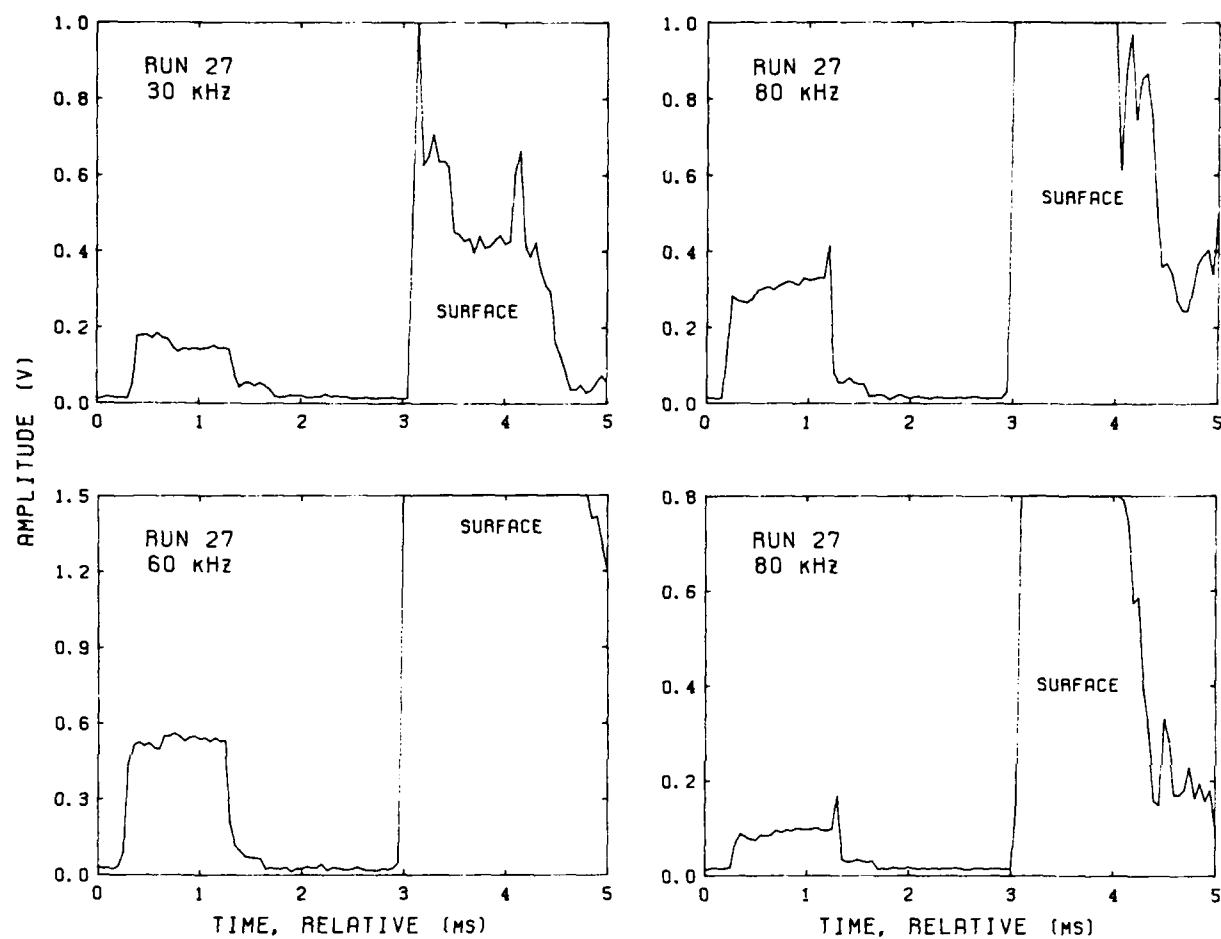
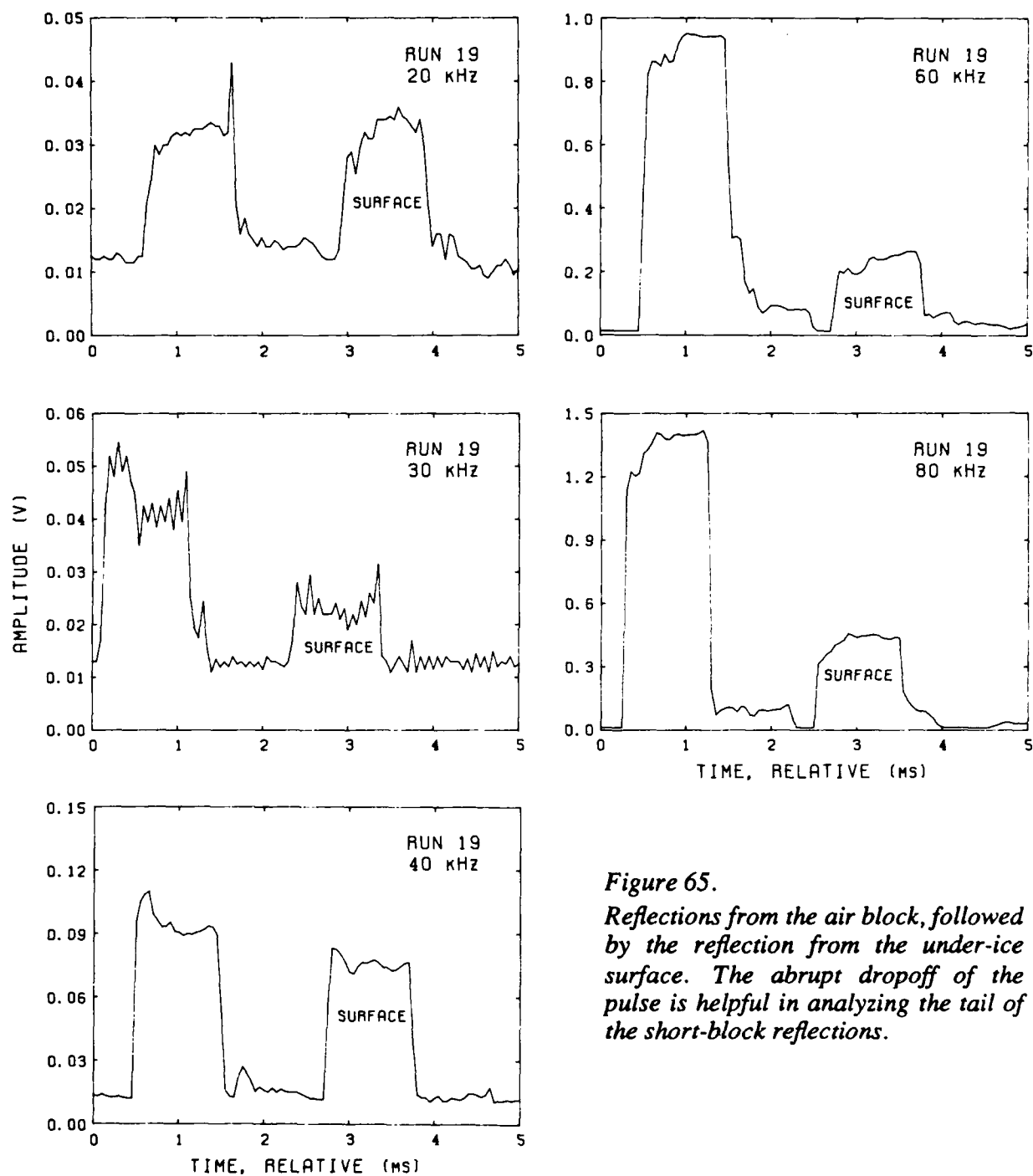


Figure 64.
Reflections from the short block, showing three levels, followed by the reflection from the under-ice surface. For several runs and frequencies.

*Figure 64, cont.*

*Figure 64, cont.*



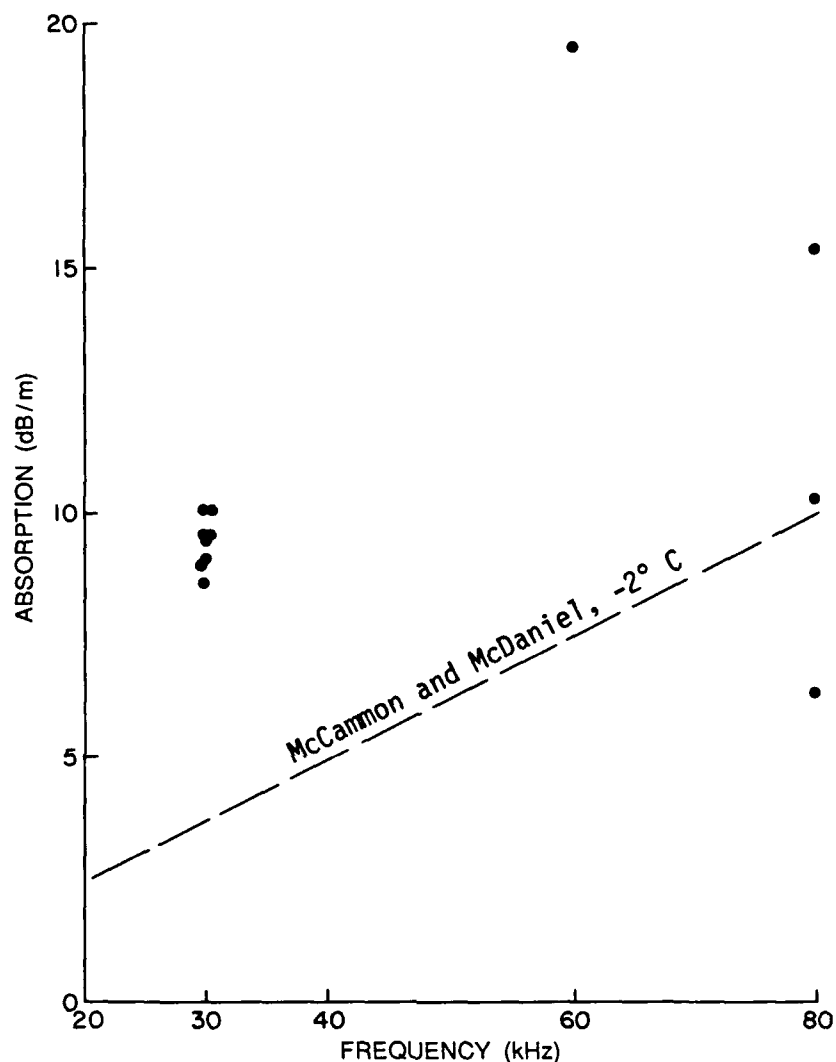


Figure 66. Absorption computed from lower and upper face echoes for the short block.

Phase differences between returns from the lower and upper faces can be computed in two ways: from the three levels using Eq. 5 (solid dots in Figure 67), and by comparing the measured thickness of the block with the acoustic wavelength (open triangles). For the latter calculations, we selected a sound speed to optimize the agreement and computed the number of wavelengths involved and the resulting phase relationship. The predictions shown in Figure 67 are for an ice thickness of 48.3 cm, a sound speed of 3272 m s^{-1} , and an assumed phase shift of 180° upon reflection from the upper face. The

number of cycles involved varied from 5.9 to 23.6 for frequencies of 20 to 80 kHz. The agreement for 30, 60, and 80 kHz is remarkably good.

The result indicates that the two reflections were coherent when they left the block and that the value selected for the sound speed was accurate. This value, 3272 m s^{-1} , agrees with that found by Schwarz and Weeks¹⁰ for -2°C ice but not with the higher values of $3800\text{--}4500 \text{ m s}^{-1}$ found by Vidmar¹¹ for very cold ice. It seems unlikely that the block would have warmed so quickly.

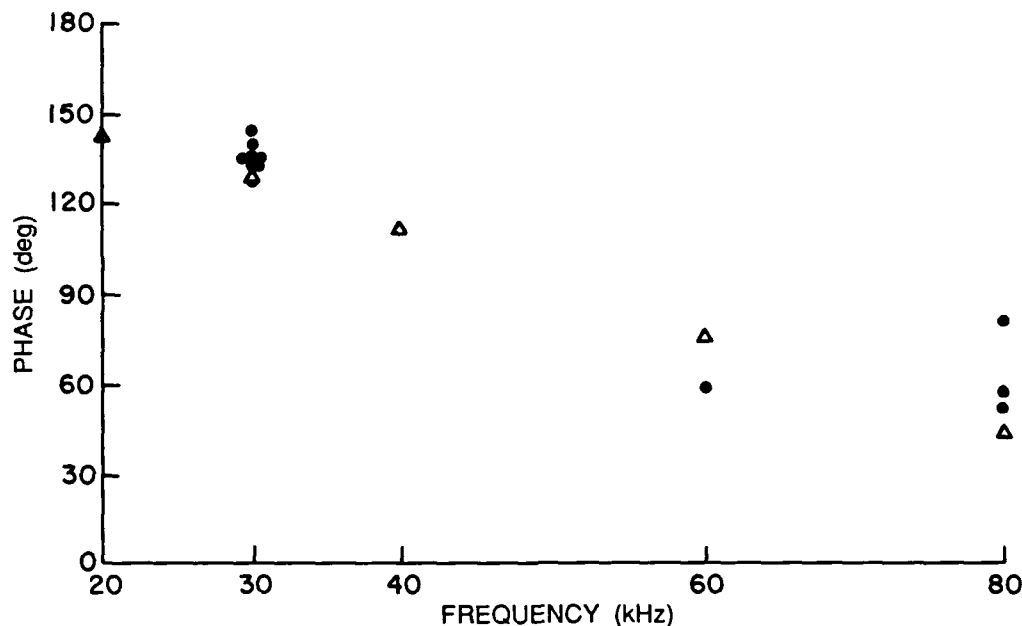


Figure 67. Phase difference between returns from the upper and lower face, as indicated by a comparison of reflection amplitudes (•) and as computed from ice thickness and sound speed (Δ) for the short block at several frequencies with approximately an integer number of wavelengths in the block.

B. Absorption Calculated from Other Blocks

We now consider blocks with a skeletal layer on the lower face. Figure 68 shows the most prominent reflection from the upper face, which occurred at 40 kHz during Run 1 with the 84-cm block. In this case, the upper face was the former snow-covered surface of the floe, which could have contained trapped air. After the 84-cm block was cut out, this face was submerged for several hours before the reflection measurements were made. The 12 other observations of upper face reflections (three from the 84-cm block, three from the 40-cm block, and six from the 109-cm block) are shown in Figures 69 and 70.

The absorption computations are not as direct as those for the short block because little is known about the reflection properties of the upper face. Equation 4 is applicable,

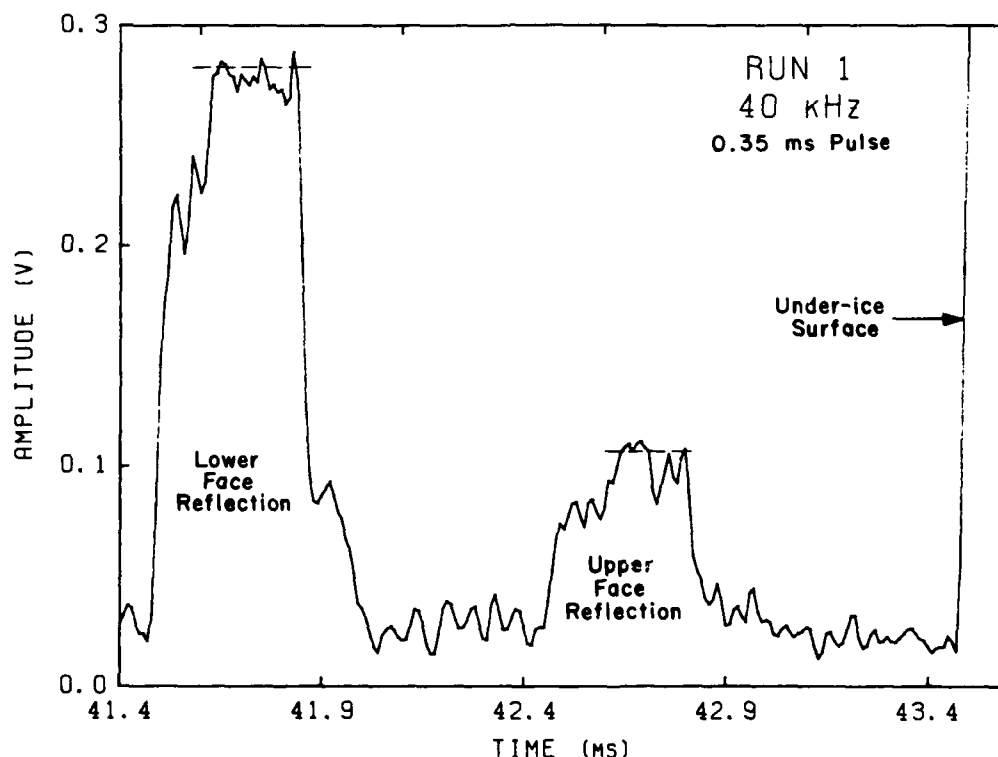


Figure 68. Lower and upper face reflections for the 84 cm block. The dashed lines mark the average amplitudes used in the analysis.

but there are two unknowns, the absorption coefficient, α , and the reflection coefficient of the upper face, R_B . We can, however, set some limits on R_B .

Certainly the ultimate upper limit would be an air-ice interface with $R_B = -1$. A considerable amount of trapped air may have caused some trend toward this condition. If the hard snow layer was cold enough when the block was submerged, it may have become glazed with ice. If this happened, a safe upper limit for $-R_B$ would probably be the R_A measured for the sawed-off short block. A probable lower limit would be the reflection coefficient measured for the lower face with its skeletal layer.

Using the lower- and upper-face returns shown in Figures 69 and 70, we computed α from Eq. 4 based on these three assumptions for R_B . The results are plotted in Figure 71. With no confirmation of trapped air in the submerged snow layer, we believe that α should lie between the "short block" and "lower surface" limits. The dashed line represents a fairly small region that would nearly satisfy this requirement. At 80 kHz, there are conflicting limits that give an uncertainty in α of about 4 dB per meter. The dashed line indicates an α of 5 ± 2 dB per meter at all frequencies; this does not agree with Figure 66, which shows an increase in absorption with frequency.

The hypothesis that the loss is mainly in the skeletal layer has been advanced by Stanton,^{12,13} who reports a measured loss of 30 dB for a 188-kHz transmission through a thin skeletal layer on 18-cm thick ice. Our present measurements on 160-cm thick ice give a loss of about 10 dB per pass at frequencies of 20–80 kHz. Our measurements may be in agreement with Stanton's if the loss is primarily in the skeletal layer (so that thickness is immaterial) and has a large increase with frequency. An increase with frequency is only slightly evident in Figure 66 and not at all in Figure 71, but these measurements were not accurate enough, and did not cover a sufficient frequency range, to determine the frequency dependence.

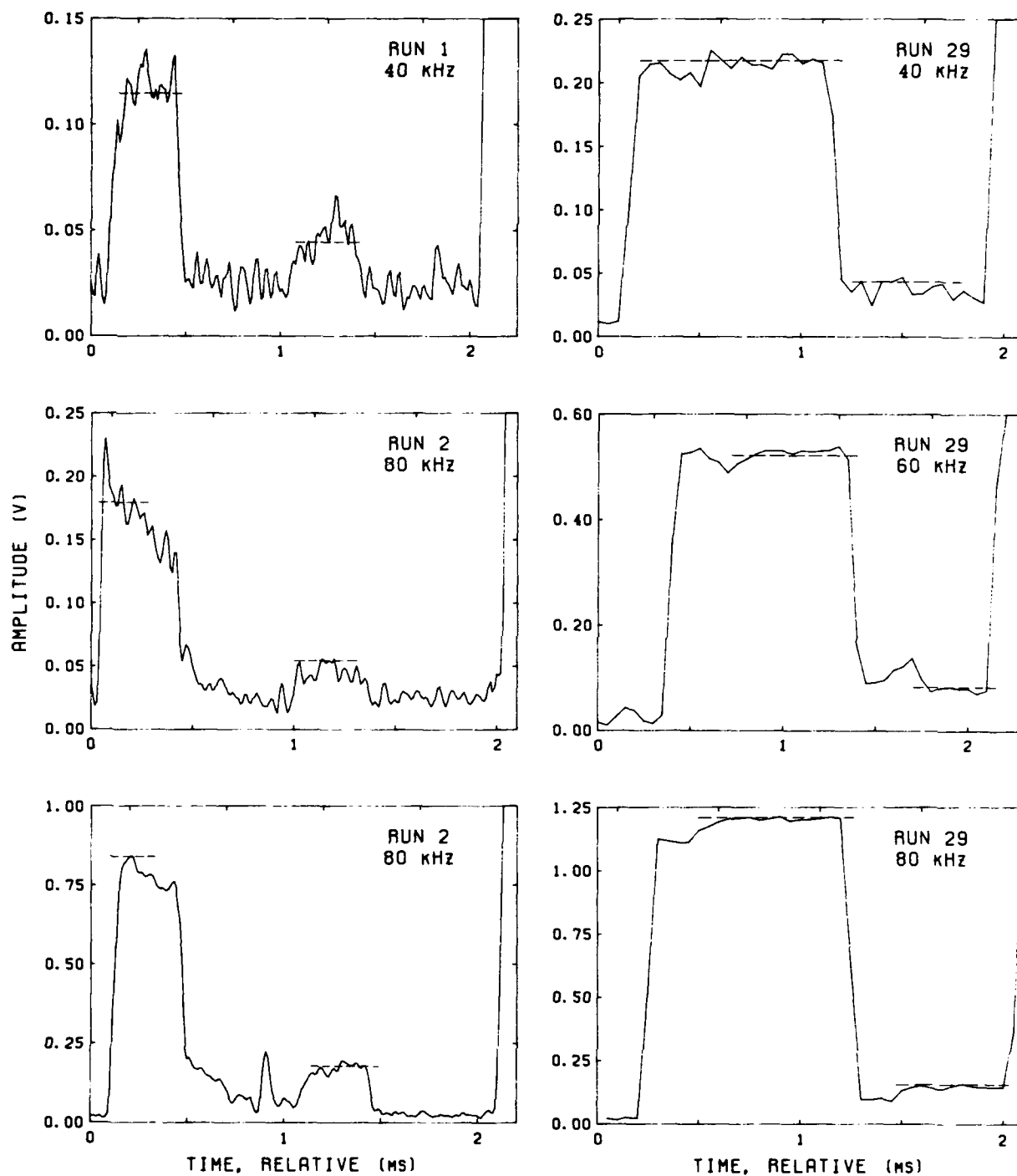


Figure 69. Other observations of upper face reflections. Left column, 84-cm block; right column, 40-cm block.

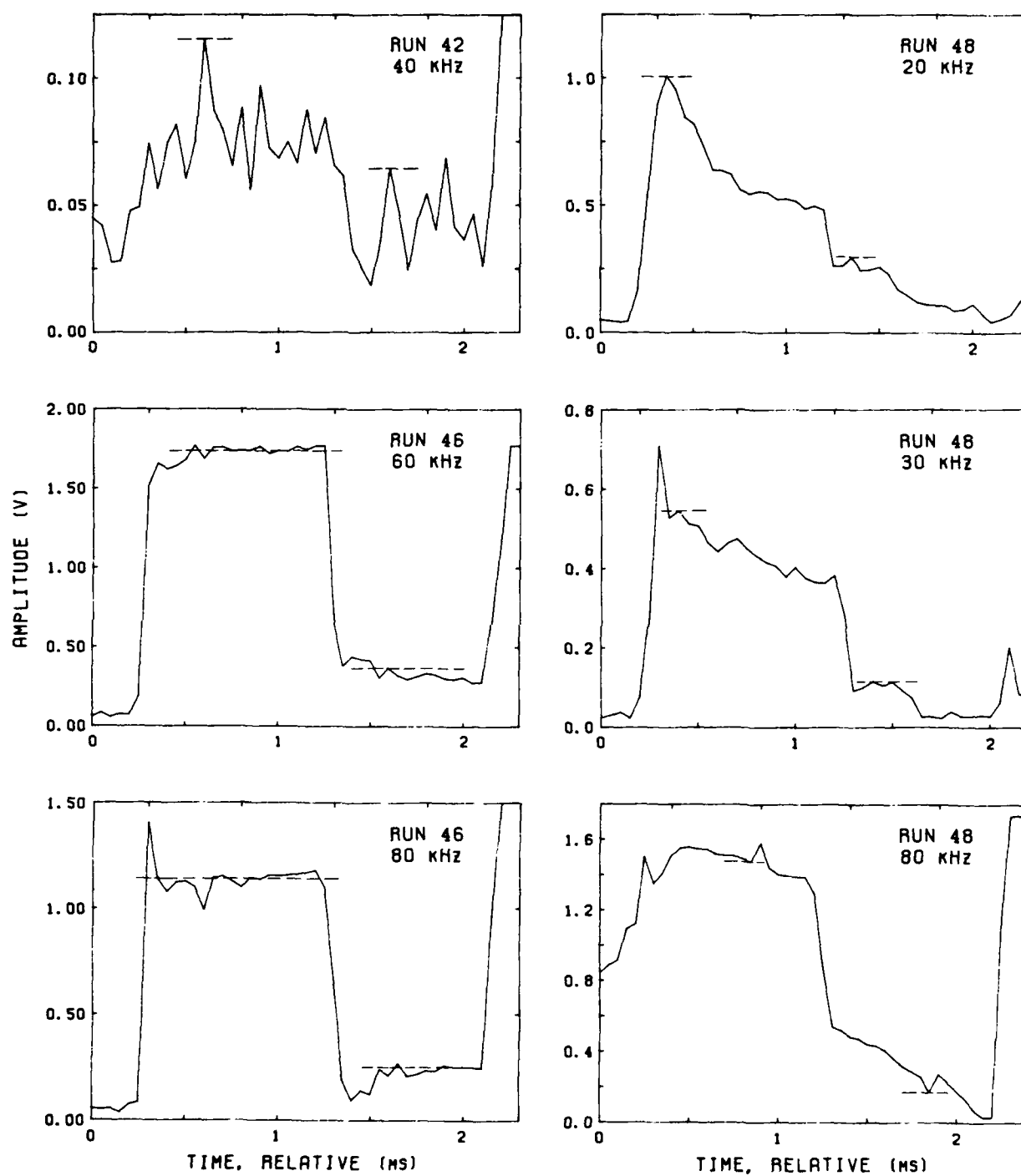


Figure 70. Other observations of upper face reflections, 109-cm block.

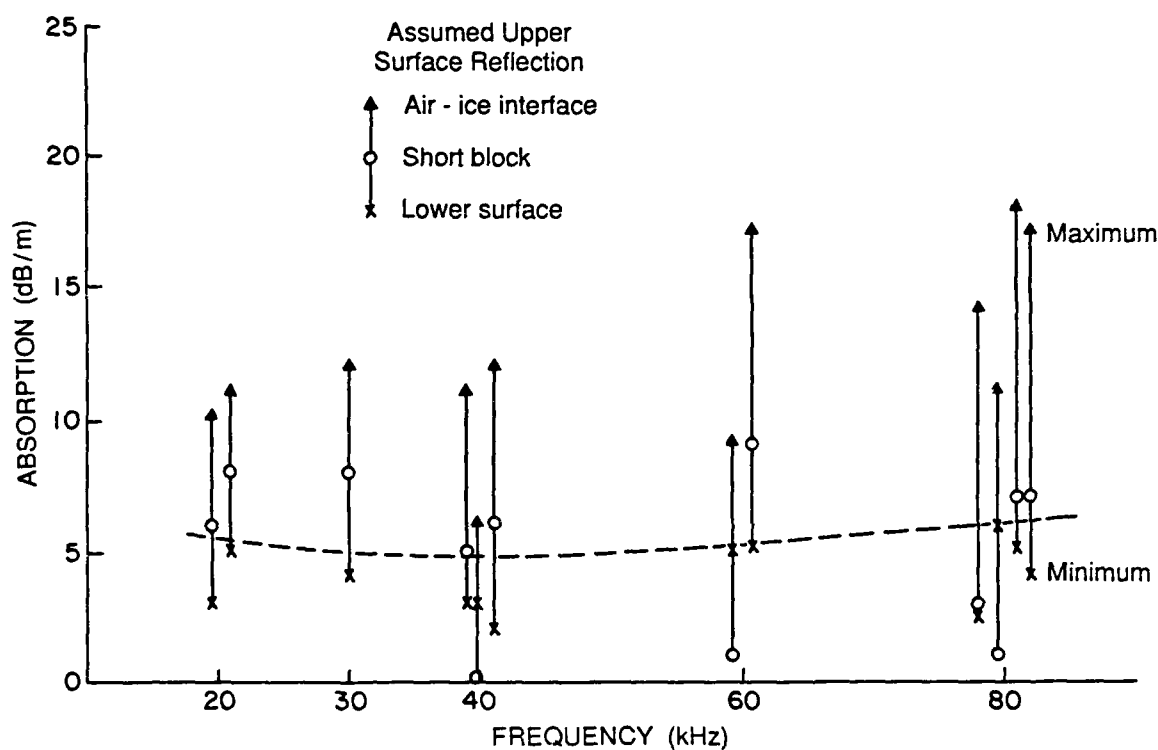


Figure 71. Calculated absorption in the three uncut blocks under three assumptions for upper surface reflection: an air-ice interface, the value of R_A used for the short-block calculations, and the reflection coefficient measured for the lower face. The line is selected as lying between the latter two.

X. RECOMMENDATIONS

Some of the uncertainties in the experimental results could be solved by making similar measurements with the following additions:

- (1) Cut off the lower surface of a block in 5-cm increments and repeat the reflection measurements to determine the effect of the transition layer. Any trapped air will have to be released.
- (2) Measure the properties of each layer of ice removed in (1).
- (3) Monitor the ice-block temperature and observe the changes in reflection and absorption as its temperature increases.
- (4) Measure the flatness of each face after the reflection measurement.
- (5) Provide same-sized air cylinders for each diameter of ice block measured to improve calibration of the system. Place an air-filled cylinder over the cutoff block during measurements to increase the return from the upper face and thus improve the absorption measurements.
- (6) Saturate the skeletal layer with air and measure the change in reflection to evaluate air as a cause of inaccuracy.
- (7) Eliminate the possibility of air contamination in the skeletal layer by rigging without divers and by doing the air-block calibrations after the ice-block measurements.

XI. REFERENCES

1. W.T. Ellison, "Simulation Studies of Under-Ice Acoustic Scattering (U)," Cambridge Acoustical Associates, Inc., 54 Rindge Avenue Extension, Cambridge, Massachusetts, 15 October 1980. (Confidential)
2. G.C. Bishop, W.T. Ellison, and L.E. Mellberg, "A simulation model for high-frequency under-ice reverberation," *J. Acoust. Soc. Am.* **82**, 275-286 (1987).
3. G.R. Garrison, R.E. Francois, T. Wen, and R.P. Stein, "Measurements of Acoustic Reflection From the End of a Cylindrical Block of Arctic Ice," APL-UW 8506, Applied Physics Laboratory, University of Washington, Seattle, September 1986
4. R.J. Urick, *Principles of Underwater Sound* (McGraw-Hill, New York, 1975), p. 275.
5. G.R. Garrison, T. Wen, R.E. Francois, W.J. Felton, and M.L. Welch, "Environmental Measurements in the Beaufort Sea, Spring 1986," APL-UW 4-86, Applied Physics Laboratory, University of Washington, Seattle, January 1987.
6. R.E. Francois and J.G. Harrison, "A thermal drill for making large holes in sea ice," *OCEAN 75 IEEE Conference on Ocean Engineering*, IEEE Pub. 75 CH0 995-1 OEC, 303-310, 1975.
7. G.F. Cox and W.F. Weeks, "Equations for Determining the Gas and Brine Volume in Sea Ice Samples," CRREL Report 82-30, U.S. Army Corps of Engineers, Cold Regions Research and Engineering Laboratory, Hanover, NH, 1982.
8. C.S. Clay and H. Medwin, *Acoustical Oceanography: Principles and Applications* (John Wiley and Sons, 1977) p. 507.
9. D.F. McCammon and S.T. McDaniel, "The influence of the physical properties of ice on reflectivity," *J. Acoust. Am. Soc.* **77**, 499-507 (1985).
10. J. Schwarz and W.F. Weeks, "Engineering properties of sea ice," *J. Glaciol.* **19**:499-531 (1977).
11. P.J. Vidmar, "Synopsis of an Investigation of the Acoustical Properties of Sea Ice," ARL TR-87-6, Applied Research Laboratories, The University of Texas at Austin, 3 February 1987.
12. T.K. Stanton, K.C. Jezek, and A.J. Gow, "Acoustical reflection and scattering from the underside of laboratory grown sea ice: Measurements and predictions," *J. Acoust. Soc. Am.* **80**, 1486-1494 (1986).

13. K. C. Jezek, T. K. Stanton, and A. J. Gow, "Laboratory studies of acoustic scattering from the underside of sea ice," *1985 IEEE Int. Geosci. Remote Sens. Symp. Dig.* 1, 87-91 (1985).
14. M. Laue, "Spiegelung und Brechung des Lichtes an der Grenzen zweier isotroper Körper," *Handb. Exp. Phys.* 18, 149 (1928).
15. L. M. Brekhovskikh, *Waves in Layered Media*, translated by R. T. Beyer (Academic Press, New York, 1980).

APPENDIX A

Effect of Surface Variations

The scattered pressure field at transmitter/receiver position x, y, z is assumed to be

$$p(x, y, z) = \int e^{ir} dx' dy', \quad (A1)$$

where

$$r = \frac{4\pi}{\lambda} \sqrt{(x-x')^2 + (y-y')^2 + (z-z')^2},$$

the primes indicate coordinates of the block face, and the integration is over the block face.

The target strength of the block face will be reduced from that of a flat surface at far field by

$$\Delta TS = 20 \log \left[\frac{\int e^{ir} dx' dy'}{\int dx' dy'} \right]. \quad (A2)$$

This approach is similar to the Kirchhoff approximation with surface slopes neglected.

For complex surfaces, a numerical integration is employed. Application to a flat surface reproduced the patterns given by rigid plate theory and gave us the near-field patterns shown in this report.

In an attempt to explain the results obtained during the measurements, we investigate three models of surface roughness. None explain all the results observed.

A. Gaussian Distribution of Surface Irregularities

We assume the bottom surface is irregular in some manner and that the deviations, h , from a plane follow a Gaussian distribution

$$g = \frac{1}{\sigma \sqrt{2\pi}} e^{-h^2/2\sigma^2}, \quad (A3)$$

where g is the probability density function of elements at depth increments h from the plane and σ is the standard deviation. Using Eq. (A2), we obtain for the far field condition

$$\Delta TS = 20 \log \left[\frac{\sum_{h=-\infty}^{\infty} g \cos\left(\frac{4\pi h}{\lambda}\right)}{\sum_{h=-\infty}^{\infty} g} \right] \quad (A4)$$

for the reduction in target strength. The target strength calculated numerically for the 84-cm block and for several values of σ is plotted in Figure A1 for comparison with the measurements. The dropoff with frequency is in fair agreement with the dropoffs for the 40-cm block (which probably contained entrapped air; see Section VIII.B) and for the short block for values of σ that seem realistic. For the larger blocks, the curves do not match the data.

B. Cylindrical

The patterns predicted for a block with a cylindrical shape on one side of the face were presented in Section VII (Figure 33). This shape could explain the results for the short block, but not for the other blocks.

C. Sinusoidal

As an alternative explanation to air as the cause of the high returns from the 40-cm block, we investigated another possibility: that the bottom surface was sinusoidal with a wavelength of about 120 cm. At this wavelength, the 40-cm block could have been accidentally sampled from the nearly flat portion of the positive half cycle which, having only a small deviation from the plane, would produce returns with little phase difference. The 84- and 109-cm blocks, being nearly a wavelength long, would produce nearly the maximum phase difference, with a resultant decrease in the return. Computations of such effects, however, did not show sufficient differences to match the measurements.

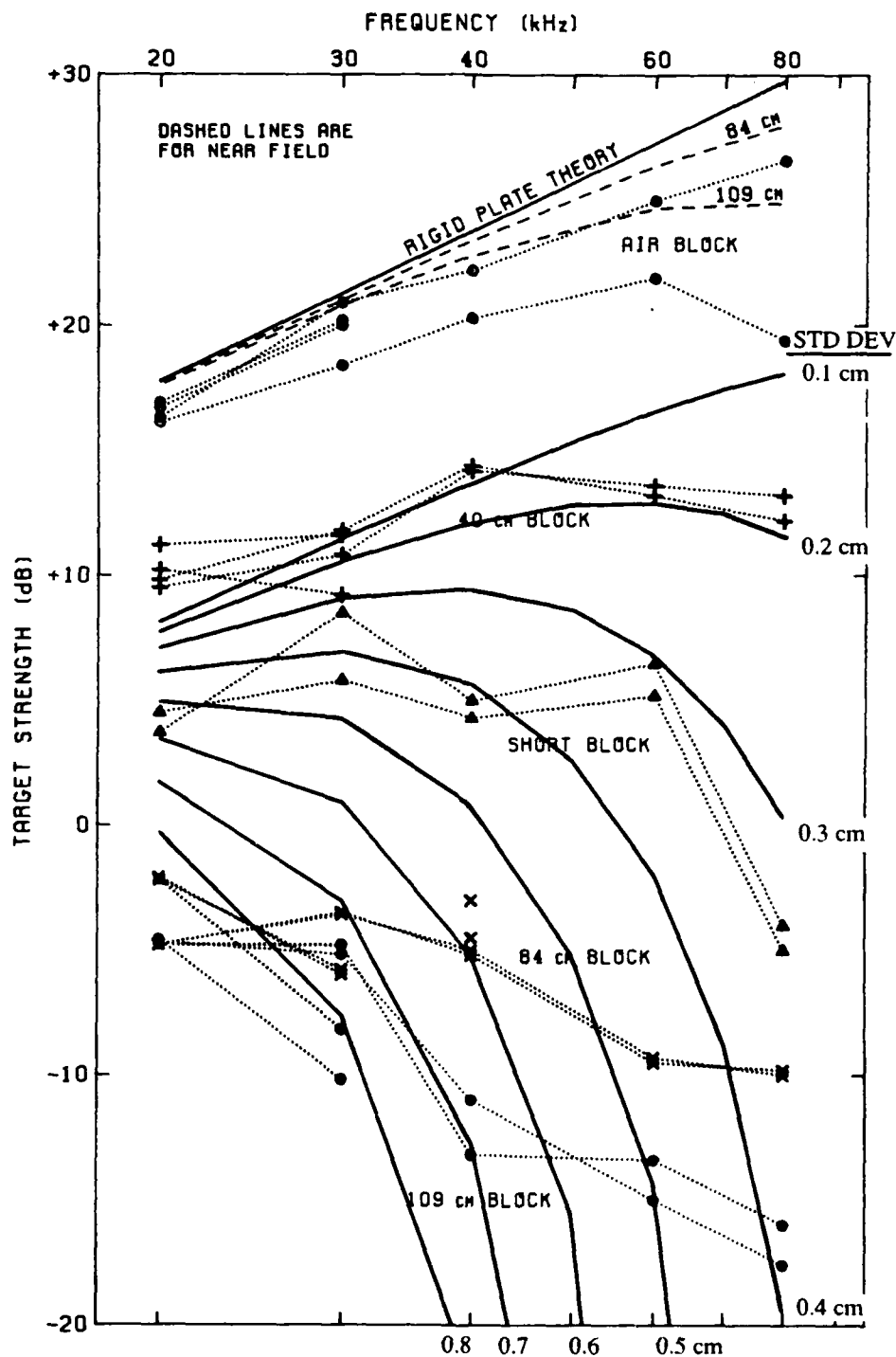


Figure A1. Computed effects of surface variations with a Gaussian distribution. The measured results are for data corrected to 84 cm by $20 \log A$. The computed corrections include a 9.5 dB reduction in target strength due to the impedance mismatch. Near-field corrections are automatically included in the numerical computation.

APPENDIX B

Sound Speed Transition Layer

If the change in sound speed at the ice-water boundary is gradual rather than abrupt, the reflection coefficient will be smaller. To determine whether the measured results could be explained by a gradual transition of sound speed in the skeletal layer, some calculations were made for a linear gradient. The results were suggestive but not satisfactory, and the study is being continued for other, smoother transitions.

The model used for the transition layer is particularly simple. The effects of differences in density and absorption between seawater and sea ice, as well as any effects of variations of these quantities in the transition layer, are ignored since they are small compared with the effects of the change in compressional wave speed; also, we are interested only in returns near vertical incidence, where the conversion of incident acoustic energy to shear modes in the ice is negligible. Thus, a two-fluid model will suffice. In the model tested to date, we assume a linear sound speed profile in the transition layer (i.e., a constant sound speed gradient). The sound speed at the bottom of the layer is that of seawater, and that at the top is that of solid sea ice. The total thickness of the layer is L , and the acoustic wavenumber in the water is $k_0 = 2\pi/\lambda_0$, where λ_0 is the acoustic wavelength in water.

The reflection coefficient for this problem has been derived by Laue¹⁴ and presented and discussed by Brekhovskikh.¹⁵ Define

$$n \equiv c_0/c_1 \quad (\text{B1})$$

and

$$A \equiv \frac{n}{1-n}, \quad (\text{B2})$$

where c_0 and c_1 are the compressional wave speeds in seawater and solid sea ice,

respectively. Then, from Ref. 11, the amplitude reflection coefficient is given by

$$|R| = \frac{\sinh(\mu \ln n)}{[\sinh^2(\mu \ln n) + 4\mu^2]^{1/2}} \quad \text{for } k_0 LA < 1/2, \quad (\text{B3})$$

and

$$|R| = \frac{\sin(m \ln n)}{[\sin^2(m \ln n) + 4m^2]^{1/2}} \quad \text{for } k_0 LA > 1/2, \quad (\text{B4})$$

where $\mu \equiv [1/4 - (k_0 LA)^2]^{1/2}$ and $m \equiv [(k_0 LA)^2 - 1/4]^{1/2}$.

In using these equations for the ice blocks measured, we first evaluate $k_0 LA$ to determine which equation to use. The minimum value will be at the lowest frequency, 20 kHz, and a minimum layer thickness of, say, 1 cm; this calculates to be 0.62. Therefore the second equation is applicable for $L > 1$ cm.

A plot of the reflection coefficient calculated for values of L from 1 to 10 cm is presented in Figure B1 for the five frequencies used in the experiment. The values measured for the 84-cm block, which we are trying to match, are shown at the right.

For an L that gives agreement at 20 kHz (5 cm in Figure B1), the reflection coefficients for the other frequencies generally decrease with frequency, as measured. For other thicknesses, however, the variation of R with frequency is oscillatory. We believe that the general decrease in R with frequency would happen at all thicknesses, not just at 5 cm. Therefore, this model, at least as implemented with the uniform gradient, does not give a satisfactory prediction. A smoother transition without slope discontinuities, such as an S-shape, should not produce the oscillations seen in Figure B1 and would probably be more suitable.

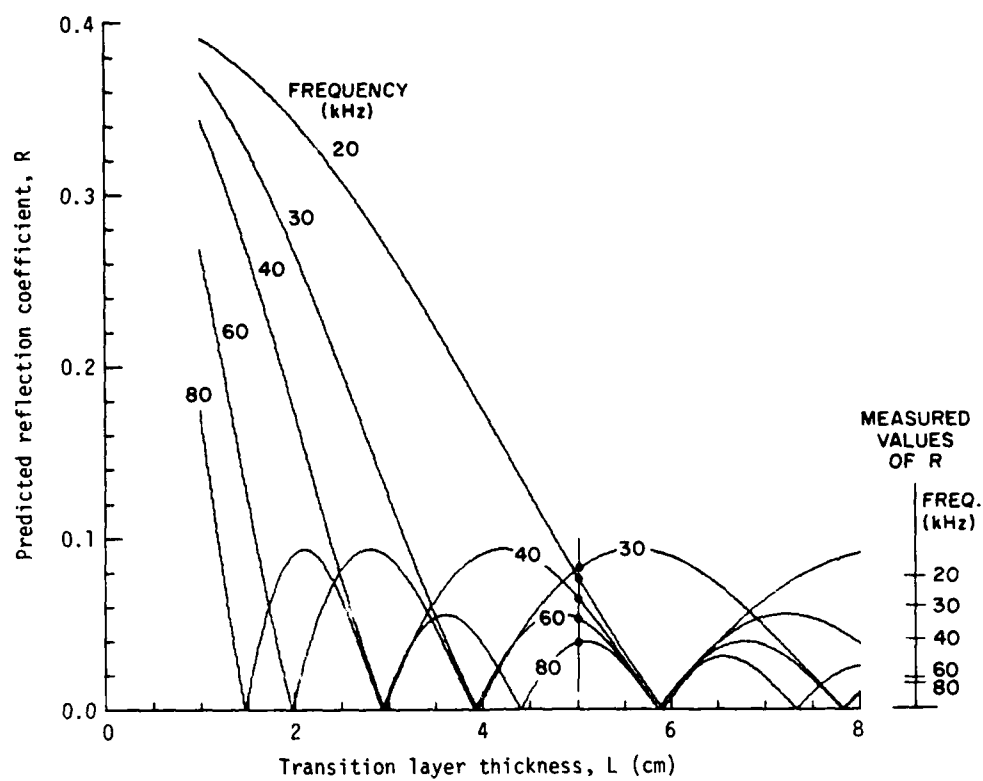


Figure B1. Predicted reflection coefficient for the bottom of the ice with a linear transition of sound speed over thickness L .

UNCLASSIFIED

SECURITY CLASSIFICATION OF THIS PAGE (When Data Entered)

REPORT DOCUMENTATION PAGE		READ INSTRUCTIONS BEFORE COMPLETING FORM
1. REPORT NUMBER APL-UW 8707	2. GOVT ACCESSION NO.	3. RECIPIENT'S CATALOG NUMBER
4. TITLE (and Subtitle) ACOUSTIC REFLECTIONS FROM CYLINDRICAL BLOCKS OF ARCTIC ICE, 1986		5. TYPE OF REPORT & PERIOD COVERED Technical 1986
		6. PERFORMING ORG. REPORT NUMBER
7. AUTHOR(s) G.R. Garrison, R.E. Francois, T. Wen, and R.P. Stein		8. CONTRACT OR GRANT NUMBER(s) SPAWAR N00024-85-C-6264 and N00039-88-C-0054
9. PERFORMING ORGANIZATION NAME AND ADDRESS Applied Physics Laboratory University of Washington 1013 N.E. 40th St., Seattle, WA 98105		10. PROGRAM ELEMENT, PROJECT, TASK AREA & WORK UNIT NUMBERS 62435N
11. CONTROLLING OFFICE NAME AND ADDRESS Office of Naval Technology, Code 234 Ballston Center Tower #1 800 N. Quincy Street, Arlington, VA 22217-5000		12. REPORT DATE August 1988
		13. NUMBER OF PAGES 102
14. MONITORING AGENCY NAME & ADDRESS (if different from Controlling Office) Naval Ocean Research and Development Activity Code 242 NSTL Station, MS 39522-5004		15. SECURITY CLASS. (of this report) Unclassified
		15a. DECLASSIFICATION DOWNGRADING SCHEDULE
16. DISTRIBUTION STATEMENT (of this Report) Approved for public release; distribution is unlimited.		
17. DISTRIBUTION STATEMENT (of the abstract entered in Block 20, if different from Report)		
18. SUPPLEMENTARY NOTES		
19. KEY WORDS (Continue on reverse side if necessary and identify by block number) Acoustic reflection from ice Ice block target strength Target strength of ice		
20. ABSTRACT (Continue on reverse side if necessary and identify by block number) Measurements of acoustic reflections from cylindrical blocks of arctic ice were conducted in spring 1986. Blocks with diameters of 40, 84, and 109 cm were individually cored out and depressed below the surface. Acoustic pulses were transmitted from below, and thus the returns from the depressed block at shorter range were separ- able from the reflections off the underside of the ice canopy. The (cont.)		

UNCLASSIFIED

SECURITY CLASSIFICATION OF THIS PAGE(When Data Entered)

20, cont.

sound source/receiver was moved horizontally beneath the block to measure the angular response pattern. The skeletal layer formed at the bottom of the ice during freezing appeared to reduce the reflection at normal incidence below that expected from the bulk physical properties of the ice; this reduction increased greatly with frequency in the measurement range, 20-80 kHz. The reflective properties are compared with the observed structure of the skeletal layer to understand the nature of the reflection.

UNCLASSIFIED

SECURITY CLASSIFICATION OF THIS PAGE(When Data Entered)

Distribution List for APL-UW 8707

Assistant Secretary of the Navy
(Research, Engineering and Systems)
Department of the Navy
Washington, DC 20350 [2 cp]

Chief of Naval Operations
Department of the Navy
Washington, DC 20350-2000

OP 07
OP 071
OP 095
OP 0962E
OP 0962X
OP 096T
OP 098
OP 22
OP 223

Director of Defense Research
Office of Assistant Director (Ocean Control)
The Pentagon
Washington, DC 20301-5000

Defense Technical Information Center
Cameron Building #5
Alexandria, VA 22304-6145

Office Chief of Naval Research
Department of the Navy
800 N. Quincy Street
Arlington, VA 22217-5000

OCNR 00
OCNR 000A
OCNR 112
OCNR 1125
OCNR 1125AR
OCNR 1125OA
OCNR 1222T
OCNR 125

Office of Naval Research
R. Silverman, Resident Representative
315 University District Bldg., JD-16
1107 N.E. 45th Street
Seattle, WA 98195

Office of Naval Technology
Department of the Navy
Ballston Center Tower #1
800 N. Quincy Street
Arlington, VA 22217-5000

Code 22
Code 23
Code 23D
Code 232
Code 234

Director
Defense Advanced Research Project Agency
1400 Wilson Boulevard
Arlington, VA 22209

Commanding Officer
Naval Intelligence Support Center
4301 Suitland Road
Washington, DC 20390

Commanding Officer
Naval Polar Oceanographic Center
4301 Suitland Road
Washington, DC 20390-5140

Library

Center for Naval Analyses
4401 Ford Avenue
P.O. Box 16268
Alexandria, VA 22302-0268

Attn: Technical Information Center

Commander
Naval Air Systems Command Hq.
Department of the Navy
Washington, DC 20361

AIR 340L

Commander
Space and Naval Warfare Systems Command (NC1)
(SPAWAR)
Department of the Navy
Washington, DC 20363-5100

SPAWAR 005
PMW-180
PMW-181
PMW-182
PMW-182-2

Commander
Naval Sea Systems Command
Department of the Navy
Washington, DC 20362

NSEA 05R
NSEA 06
NSEA 06U2
NSEA 63D [2 cp]
NSEA 63D4
Code PMS-402
Code PMS-406
Code PMS-407

Commanding Officer
Naval Underwater Systems Center
Newport, RI 02840

Library [2 cp]
Code 00
Code 22202
Code 3824
Code 801
Code 81
Code 8211
Code 8212

Officer-in-Charge
New London Laboratory
Naval Underwater Systems Center
New London, CT 06320

Library
Code 01Y [2 cp]
Code 2111

Commander
Naval Weapons Center
China Lake, CA 93555

Library

Commander
Naval Surface Warfare Center
White Oak
Silver Spring, MD 20903-5000

Library [2 cp]
Code R-01
Code R-43 [2 cp]
Code U-04
Code U-06
Code U-42 [2 cp]

Commander
Naval Ocean Systems Center
San Diego, CA 92152-5000

Library
Code 00
Code 19 [2 cp]
Code 541

Commanding Officer
Naval Civil Engineering Laboratory
Port Hueneme, CA 93043-5003

Library
Code L43

Director
Naval Research Laboratory
Washington, DC 20375

Library
Code 5100
Code 5123

Commanding Officer
Naval Coastal Systems Center
Panama City, FL 32407

Library

Commanding Officer
Naval Ocean Research and
Development Activity
Stennis Space Center, MS 39529-5004

Library [2 cp]
Code 113
Code 200
Code 240
Code 242 [3 cp]
Code 252

Commanding Officer
Naval Oceanographic Office
Stennis Space Center, MS 39522-5001

Code OA
Code OAR
Code OARU

Commander
Naval Air Development Center
Warminster, PA 18974

Library
Code 3031 (A. Horbach)

Commander
David Taylor Research Center
Bethesda, MD 20084

Library
Code 1720 [2 cp]
Code 1908

Commanding Officer
Naval Submarine School
Box 70
Naval Submarine Base -- New London
Groton, CT 06340

Superintendent
Naval Postgraduate School
Monterey, CA 93943-5100

Library [2 cp]
Code 68

Commander, SECOND Fleet
Fleet Post Office
New York, NY 09501

Commander, THIRD Fleet
Fleet Post Office
San Francisco, CA 96601

Commander Submarine Force
U.S. Atlantic Fleet
Norfolk, VA 23511

Code 00
Code 019
Code 22
Code N311

Commander Submarine Force
U.S. Pacific Fleet
Pearl Harbor, HI 96860

Code 00
Code N2
Code N21

Commander
Submarine Squadron THREE
Fleet Station Post Office
San Diego, CA 92132

Commander
Submarine Group FIVE
Fleet Station Post Office
San Diego, CA 92132

Commander
Submarine Development Squadron TWELVE
Box 70
Naval Submarine Base - New London
Groton, CT 06340
Code 20

Director
Applied Research Laboratories
The University of Texas at Austin
P.O. Box 8029
Austin, TX 78713-8029

Library

Director
Applied Research Laboratory
The Pennsylvania State University
State College, PA 16801

C. Ackerman
R. Ingram [2 cp]
E. Liszka
S. McDaniel
F. Symons, Jr.

Polar Research Laboratory, Inc.
6309 Carpenteria Avenue
Carpenteria, CA 90813

Sandia National Laboratories
Kirtland Air Force Base
P.O. Box 5800
Albuquerque, NM 87185

Library